

# “ $\gamma + jet$ ” process application for setting the absolute scale of jet energy and determining the gluon distribution at the Tevatron in Run II.

D.V. Bandurin, N.B. Skachkov

*Laboratory of Nuclear Problems  
Joint Institute for Nuclear Research, Dubna, Russia*

## Abstract

The consequences of application of new set of criteria, proposed in our previous works, for the improvement of a jet energy calibration accuracy with the process “ $p\bar{p} \rightarrow \gamma + jet + X$ ” at Tevatron and for a reduction of background events contribution are studied. The efficiencies of the used selection criteria are estimated. The distributions of these events over  $P_t^\gamma$  and  $\eta^{jet}$  are presented. The features of “ $\gamma + jet$ ” events in the central calorimeter region of the D0 detector ( $|\eta| < 0.7$ ) are investigated.

It is also shown that the samples of “ $\gamma + jet$ ” events, selected with the cuts used for the jet energy calibration, may have the statistics sufficient for determining the gluon distribution function of a proton in the region of  $2 \times 10^{-3} < x < 1.0$  and the values of  $Q^2$  by one order higher than that reached in the experiments at HERA.

Monte Carlo events produced by the PYTHIA 5.7 generator are used for this aim.

## 1. INTRODUCTION.

Setting an absolute energy scale for a jet, detected mostly by hadronic and electromagnetic calorimeters (HCAL and ECAL), is an important task for any  $p\bar{p}$  or  $pp$  collider experiment (see e.g. [1–8]).

The main goal of this work is to find out the selection criteria for “ $p\bar{p} \rightarrow \gamma + jet + X$ ” events (we shall use in what follows the abbreviation “ $\gamma + jet$ ” for them) that would lead to the most precise determination of the transverse momentum of a jet (i.e.  $P_t^{jet}$ ) via assigning a photon  $P_t^\gamma$  to a signal produced by a jet. Our study is based on the “ $\gamma + jet$ ” events generated by using PYTHIA 5.7 [9]. Their analysis was done on the “particle level” (in the terminology of [1]), i.e. without inclusion of detector effects. The information provided by this generator is analyzed to track starting from the parton level (where parton-photon balance is supposed to take place in a case of initial state radiation absence) all possible sources that may lead to the  $P_t^\gamma - P_t^{jet}$  disbalance in a final state. We use here the methods applied in [10]–[18] (see also [20]) and [21], [22] for analogous task at LHC energy. The corresponding cuts on physical variables, introduced in [10]–[17], are applied here. Their efficiency is estimated at the particle level of simulation at Tevatron energy with account of D0 detector geometry.

We consider here the case of the Tevatron Run II luminosity  $L = 10^{32} \text{ cm}^{-2}\text{s}^{-1}$ . It will be shown below that its value is quite sufficient for selecting the event samples of large enough volume for application strict cuts as well as of new physical variables introduced in [10]–[17].

Section 2 is a short introduction into the physics connected with the discussed problem. General features of “ $\gamma + jet$ ” processes are presented here. We review the possible sources of the  $P_t^\gamma$  and  $P_t^{jet}$  disbalance and the ways of selecting those events where this disbalance has a minimal value on the particle level.

In Section 3.1 we give the definitions are given for the transverse momenta of different physical objects that we suppose to be important for studying the physics connected with a jet calibration procedure. Values of these transverse momenta enter into the  $P_t$ -balance equation that reflects the total  $P_t$  conservation law for the  $p\bar{p}$ -collision event as a whole.

Section 3.2 describes the criteria we have chosen to select “ $\gamma + jet$ ” events for the jet energy calibration procedure. The “cluster” (or mini-jet) suppression criterion ( $P_{tCUT}^{clust}$ ) which was formulated in an evident form in our previous publications [10]–[18] is used here <sup>1</sup>. (Its important role for selection of events with a good balance of  $P_t^\gamma$  and  $P_t^{jet}$  will be illustrated in Sections 5–8.) <sup>2</sup> These clusters have a physical meaning of a part of another new experimentally measurable quantity, introduced in [10]–[18] for the first time, namely, the sum of  $\mathbf{P}_t$  of those particles that are *out* of the “ $\gamma + jet$ ” system (denoted as  $P_t^{out}$ ) and are *detectable* in the whole pseudorapidity  $\eta$  region covered by the detector <sup>3</sup>. The vector and scalar forms of the total  $P_t$  balance equation, used for the  $p\bar{p}$ -event as a whole, are given in Sections 3.1 and 3.3 respectively.

Another new thing is a use of a new physical object, proposed also in [10]–[18] and named an “isolated jet”. This jet is contained in the cone of radius  $R = 0.7$  in the  $\eta - \phi$  space and does not have any noticeable  $P_t$  activity in some ring around. The width of this ring is taken to be of  $\Delta R = 0.3$  (or approximately of the width of 3 calorimeter towers). In other words, we will select a class of events having a total  $P_t$  activity inside the ring around this “isolated jet” within 3 – 5%

---

<sup>1</sup>We use here, as in [13]–[18], for most application the PYTHIA’s default jetfinder LUCCELL as well as UA1 taken from the CMS program of fast simulation CMSJET [24] for defining jets in an event.

<sup>2</sup>The analogous third jet cut thresholds  $E_T^3$  (varying from 20 to 8 GeV) for improving a single jet energy resolution in di-jet events were used in [29].

<sup>3</sup> $|\eta| < 4.2$  for D0

of jet  $P_t$ . It will be shown in Sections 6, 7 and Appendix 2 that the number of events with such a clean topological structure would not be small at Tevatron energy and  $L = 10^{32} \text{ cm}^{-2} \text{ s}^{-1}$ .

Section 4 is devoted to the estimation of a size of a non-detectable neutrino contribution to a jet. The correlation of the upper cut value, imposed onto  $P_t^{miss}$ <sup>4</sup>, with the mean value of  $P_t$  of neutrinos belonging to the jet  $P_t$  is considered. The detailed results of this section are presented in the tables of Appendix 1. They also include the ratios of the gluonic events  $qg \rightarrow q + \gamma$  containing the information about the gluon distribution inside a proton. In the same tables the expected number of events (at  $L_{int} = 300 \text{ pb}^{-1}$ ) having charm ( $c$ ) and beauty ( $b$ ) quarks in the initial state of the gluonic subprocess are also given.

Since the jet energy calibration is rather a practical than an academic task, in all the following sections we present the rates obtained with the cuts varying from strict to weak because their choice would be a matter of step-by-step statistics collection during the data taking.

Section 5 includes the results of studying the dependence of the initial state radiation (ISR)  $P_t$ -spectrum on the cut imposed on the clusters  $P_t$  ( $P_t^{clust}$ ) and on the angle between the transverse momenta vectors of a jet and a photon. We also present the rates for four different types of “ $\gamma + jet$ ” events, in which jet fits completely in one definite region of the calorimeter: in Central Calorimeter (CC) with  $|\eta| < 0.7$  or in Intercryostat Calorimeter (IC) with  $0.7 < |\eta| < 1.8$  or in End Calorimeter (EC) with  $1.8 < |\eta| < 2.5$  or, finally, in Forward Calorimeter (FC) with  $2.5 < |\eta| < 4.2$ .

In Section 6 our analysis is concentrated on the “ $\gamma + 1 jet$ ” events having a jet entirely contained within the central calorimeter region. The dependence of spectra of different physical variables<sup>5</sup> (and among them those appearing in the  $P_t$  balance equation of event as a whole) on  $P_t^{clust}$  is shown there.

The dependence of the number of events (for  $L_{int} = 300 \text{ pb}^{-1}$ ) on  $P_t^{clust}$  as well as the dependence on it of the fractional  $(P_t^\gamma - P_t^{jet})/P_t^\gamma$  disbalance is studied in Section 7. The details of this study are presented in the tables of Appendix 2 that together with the corresponding Figs. 10–12 can serve to justify the variables and cuts introduced in Section 3.

In Section 8 we present an estimation of the efficiency of background suppression (that was one of the main guidelines to establish the selection rules proposed in Section 3) for different numerical values of cuts.

The importance of the simultaneous use of the above-mentioned new parameters  $P_t^{clust}$  and  $P_t^{out}$  and also of the “isolated jet” criterion for background suppression (as well as for improving the value of the  $P_t^\gamma$  and  $P_t^{jet}$  balance) is demonstrated in Tables 8–11 of Section 8 as well as in the tables of Appendix 3 for various  $P_t^\gamma$  intervals.

The tables of Appendix 3 include a fractional disbalance values  $(P_t^\gamma - P_t^{jet})/P_t^\gamma$  that are found with an additional (as compared with tables of Appendix 2) account of the  $P_t^{out}$  cut. They contain the final and *first main* result (as they include the background contribution) of our study of setting an absolute scale of a jet energy at the particle level defined by generation with PYTHIA.

Section 9 contains the *second main* result of our study of “ $\gamma + jet$ ” events at Tevatron energy. Here we investigate a possibility of using the same sample of the topologically clean “ $\gamma + jet$ ” events, obtained with the described cuts, for determining the gluon distribution in a proton (as it was done earlier for LHC energy in [18], [20]). The kinematic plot presented here shows what a region of  $x$  and  $Q^2$  variables can be covered at Tevatron energies with a sufficient number of events for this aim. The comparison with the kinematic regions covered by other

---

<sup>4</sup>see (7) for definition

<sup>5</sup>mostly those that have a strong influence on the  $P_t^\gamma - P_t^{jet}$  balance in an event.

experiments where parton distributions were studied is also shown in the same plot (see Fig. 17).

About the Summary. We tried to write it in a way allowing a dedicated reader, who is interested in result rather than in method, to pass directly to it after this sentence.

Since the results presented here were obtained with the PYTHIA simulation, we are planning to carry out analogous estimations with another event generator like HERWIG, for example, in subsequent papers.

## 2. GENERALITIES OF THE “ $\gamma + jet$ ” PROCESS.

*Useful variables are introduced here for studying their effects on the initial and final state radiation basing on the simulation in the framework of PYTHIA. Other effects of non-perturbative nature like primordial parton  $k_t$  effect, parton-to-jet hadronization that may lead to  $P_t^\gamma - P_t^{jet}$  disbalance within the physical models used in PYTHIA are also discussed.*

### 2.1 Leading order picture.

The idea of absolute jet energy scale setting calibration) by means of the physical process “ $p\bar{p} \rightarrow \gamma + jet + X$ ” was realized many times in different experiments (see [1–8] and references therein). It is based on the parton picture where two partons ( $q\bar{q}$  or  $qg$ ), supposed to be moving in different colliding nucleons with zero transverse momenta (with respect to the beam line), produce a photon called the “direct photon”. This process is described by the leading order (LO) Feynman diagrams shown in Fig. 1<sup>6</sup> for the “Compton-like” subprocess

$$qg \rightarrow q + \gamma \quad (1a)$$

and for the “annihilation” subprocess

$$q\bar{q} \rightarrow g + \gamma. \quad (1b)$$

As the initial partons were supposed to have zero transverse momenta,  $P_t$  of the “ $\gamma$ +parton” system produced in the final state should be also equal to zero, i.e. one can write the following  $P_t$  balance equation for photon and final parton

$$\mathbf{P}_t^{\gamma+part} = \mathbf{P}_t^\gamma + \mathbf{P}_t^{part} = 0. \quad (2)$$

One could expect that the transverse momentum of the jet produced by the final state parton ( $q$  or  $g$ ) with  $\mathbf{P}_t^{part} = -\mathbf{P}_t^\gamma$  will be close in magnitude with a reasonable precision to the transverse momentum of the final state photon, i.e.  $\mathbf{P}_t^{jet} \approx -\mathbf{P}_t^\gamma$ . Thus, in principle, having a well-calibrated photon energy scale one can determine a jet energy scale. That is the a main idea of the procedure. But a more detailed analysis leads to some features needed to be taken into account and to a photon–jet  $P_t$  balance equation in a more complex form.

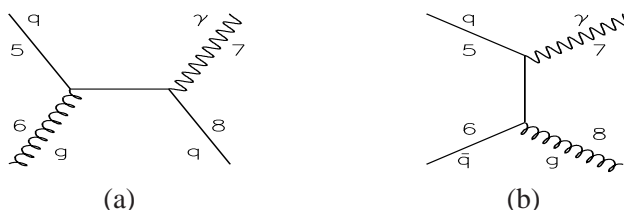


Fig. 1: Some of the leading order Feynman diagrams for direct photon production.

<sup>6</sup>for the explanation of the numeration of lines see Section 2.2

## 2.2 Initial state radiation.

Since we believe in the perturbation theory, the leading order (LO) picture described above is expected to be dominant and determine the main contribution to the cross section. The Next-to-Leading Order (NLO) approximation (see some of the NLO diagrams in Figs. 2 and 4) introduces some deviations from a rather straightforward LO-motivated idea of a jet energy calibration. A gluon radiated in the initial state (ISR), as it is seen from Fig. 2, can have its own non-zero transverse momentum  $P_t^{gluon} \equiv P_t^{ISR} \neq 0$ . Apart of a problem of appearance of extra jets (or mini-jets and clusters), that will be discussed in what follows, it leads to the non-zero transverse momenta of partons that appear in the initial state of fundamental  $2 \rightarrow 2$  QCD subprocesses (1a) and (1b). As a result of the transverse momentum conservation there arises a disbalance between the transverse momenta of a photon  $P_t^\gamma$  and of a parton  $P_t^{part}$  produced in the fundamental  $2 \rightarrow 2$  process  $5 + 6 \rightarrow 7 + 8$  shown in Fig. 2 (and in Fig. 3) and thus, finally, the disbalance between  $P_t^\gamma$  and  $P_t$  of a jet produced by this parton.

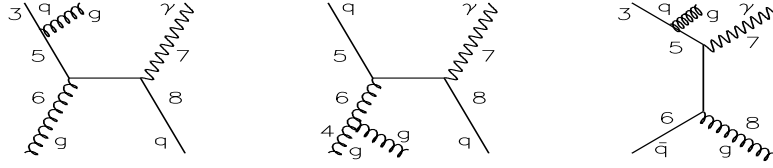


Fig. 2: Some of Feynman diagrams of direct photon production including gluon radiation in the initial state.

Following [13]–[17] and [25] we choose the modulus of the vector sum of the transverse momentum vectors  $\mathbf{P}_t^5$  and  $\mathbf{P}_t^6$  of the incoming into  $2 \rightarrow 2$  fundamental QCD subprocesses  $5 + 6 \rightarrow 7 + 8$  partons (lines 5 and 6 in Fig. 2) and the sum of their modulus as two quantitative measures

$$P_t^{5+6} = |\mathbf{P}_t^5 + \mathbf{P}_t^6|, \quad P_{t56} = |\mathbf{P}_t^5| + |\mathbf{P}_t^6| \quad (3)$$

to estimate the  $P_t$  disbalance caused by ISR<sup>7</sup>. The modulus of the vector sum

$$P_t^{\gamma+jet} = |\mathbf{P}_t^\gamma + \mathbf{P}_t^{jet}| \quad (4)$$

was also used as an estimator of the final state  $P_t$  disbalance in the “ $\gamma + jet$ ” system in [13]–[17].

The numerical notations in the Feynman diagrams (shown in Figs. 1 and 2) and in formula (3) are chosen to be in correspondence with those used in the PYTHIA event listing for description of the parton–parton subprocess displayed schematically in Fig. 3. The “ISR” block describes the initial state radiation process that can take place before the fundamental hard  $2 \rightarrow 2$  process.

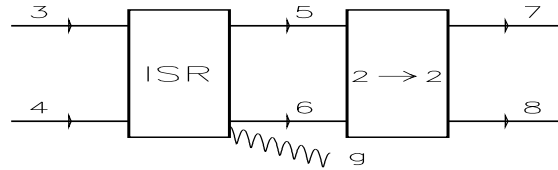


Fig. 3: PYTHIA “diagram” of  $2 \rightarrow 2$  process ( $5+6 \rightarrow 7+8$ ) following the block ( $3+4 \rightarrow 5+6$ ) of initial state radiation (ISR), drawn here to illustrate the PYTHIA event listing information.

<sup>7</sup>The variable  $P_t^{5+6}$  was used in analysis in [10]–[13].

### 2.3 Final state radiation.

Let us consider fundamental subprocesses in which there is no initial state radiation but instead final state radiation (FSR) takes place. These subprocesses are described in the quantum field theory by the NLO diagrams like those shown in Fig. 4. It is clear that appearance of an extra gluon leg in the final state may lead to appearance of additional jets (or clusters) in an event as it happens in the case of ISR described above. So, to suppress FSR (manifesting itself as some extra jets or clusters) the same tools as for reducing ISR should be used. But due to the string model of fragmentation used in PYTHIA it is much more difficult to deduce basing on the PYTHIA event listing information the variables (analogous to (3) and (4)) to describe the disbalance between  $P_t$  of a jet parent parton and  $P_t^\gamma$ . That is why, keeping in mind a close analogy of the physical pictures of ISR and FSR (see Figs. 2 and 4), we shall concentrate in the following sections on the initial state radiation supposing it to serve in some sense as a quantum field theory perturbative model of the final state radiation mechanism.

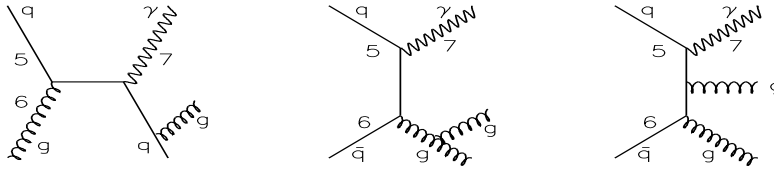


Fig. 4: Some of Feynman diagrams of direct photon production including gluon radiation in the final state.

### 2.4 Primordial parton $k_t$ effect.

Now after considering the disbalance sources connected with the perturbative corrections to the leading order diagrams let us mention the physical effects of a non-perturbative nature. A possible non-zero value of the intrinsic transverse parton velocity inside a colliding proton may be another source of the  $P_t^\gamma$  and  $P_t^{part}$  disbalance in the final state. Nowadays this effect can be described mainly in the phenomenological way. Its reasonable value is supposed to lead to the value  $k_t \leq 1.0 \text{ GeV}/c$ . Sometimes in the literature a total effect of ISR and of the intrinsic parton transverse momentum is denoted by a common symbol “ $k_t$ ”. Here we follow the approach and the phenomenological model used in PYTHIA where these two sources of the  $P_t^\gamma$  and  $P_t^{jet}$  disbalance, having different nature, perturbative and non-perturbative, can be switched on separately by different keys <sup>8</sup>. In what follows we shall keep the value of  $k_t$  mainly to be fixed by the PYTHIA default value  $\langle k_t \rangle = 0.44 \text{ GeV}/c$ . The dependence of the disbalance between  $P_t^\gamma$  and  $P_t^{jet}$  on possible variation of  $k_t$  was discussed in detail in [17, 19]. The general conclusion from there is that any variation of  $k_t$  within reasonable boundaries (as well as slightly beyond them) does not produce a large effect in the case when the initial state radiation is switched on. The latter makes a dominant contribution.

### 2.5 Parton-to-jet hadronization.

Another non-perturbative effect that leads to the  $P_t^\gamma - P_t^{jet}$  disbalance is connected with hadronization (or fragmentation into hadrons) of the parton produced in the fundamental  $2 \rightarrow 2$  subprocess into a jet. The hadronization of a parton into a jet is described in PYTHIA within the Lund string fragmentation model. The mean values of the fractional  $(P_t^{jet} - P_t^{parton})/P_t^{parton}$  disbalance is presented in the tables of Appendix 2 for UA1 jetfinding algorithm. It is seen that a hadronization effect has a sizable contribution into  $P_t^\gamma - P_t^{jet}$  disbalance.

<sup>8</sup>Variables MSTP(61) for ISR and PARP(91), PARP(93), MSTP(91) for intrinsic parton transverse momentum  $k_t$  (see [9])

### 3. CHOICE OF MEASURABLE PHYSICAL VARIABLES FOR THE “ $\gamma + jet$ ” PROCESS AND THE CUTS FOR BACKGROUND REDUCTION.

The classification of different physical objects that participate in “ $\gamma + jet$ ” events and that may give a noticeable contribution into the total  $P_t$ -balance in an event as a whole is done.

Two new physical observables, namely,  $P_t$  of a cluster and  $P_t$  of all detectable particles beyond “ $\gamma + jet$ ” system, as well as the definition of isolated jet, proposed for studying  $P_t^{\gamma} - P_t^{jet}$  disbalance in [10]–[17], are discussed.

The selection cuts for physical observables of “ $\gamma + jet$ ” events are given.

The  $P_t$ -balance equation for the event as a whole is written in scalar form that allow to express the  $P_t^{\gamma} - P_t^{jet}$  disbalance in terms of the considered physical variables.

Apart from (1a) and (1b), other QCD subprocesses with large cross sections, by orders of magnitude larger than the cross sections of (1a) and (1b), can also lead to high  $P_t$  photons and jets in final state. So, we face the problem of selecting signal “ $\gamma + jet$ ” events from a large QCD background. Here we shall discuss a choice of physical variables that would be useful, under some cuts on their values, for separation of the desirable processes with direct photon (“ $\gamma^{dir}$ ”) from the background events. A possible “ $\gamma^{dir}$ –candidate” may originate from the  $\pi^0$ ,  $\eta$ ,  $\omega$  and  $K_s^0$  meson decays or may be caused by a bremsstrahlung photon or by an electron (see Section 8).

We take the D0 ECAL size to be limited by  $|\eta| \leq 2.5$  and the calorimeter to be limited by  $|\eta| \leq 4.2$  and to consist of CC, IC, EC, FC parts, where  $\eta = -\ln(\tan(\theta/2))$  is a pseudorapidity defined in terms of a polar angle  $\theta$  counted from the beam line. In a plane transverse to the beam line the azimuthal angle  $\phi$  defines directions of  $\mathbf{P}_t^{Jet}$  and  $\mathbf{P}_t^{\gamma}$ .

#### 3.1 Measurable physical variables and the $P_t$ vector balance equation.

In  $p\bar{p} \rightarrow \gamma + jet + X$  events we are going to study the main physical object will be a high  $P_t$  jet to be detected in the  $|\eta| < 4.2$  region and a direct photon registered by the ECAL up to  $|\eta| < 2.5$ . In these events there will be a set of particles mainly caused by beam remnants, i.e. by spectator parton fragments, that are flying mostly in the direction of a non-instrumented volume ( $|\eta| > 4.2$ ) in the detector. Let us denote the total transverse momentum of these non-observable particles ( $i$ ) as

$$\sum_{i \in |\eta| > 4.2} \mathbf{P}_t^i \equiv \mathbf{P}_t^{|\eta| > 4.2}. \quad (5)$$

Among the particles with  $|\eta| < 4.2$  there may also be neutrinos. We shall denote their total momentum as

$$\sum_{i \in |\eta| < 4.2} \mathbf{P}_{t(\nu)}^i \equiv \mathbf{P}_{t(\nu)}. \quad (6)$$

A sum of transverse momenta of these two kinds of non-detectable particles will be denoted as  $P_t^{miss}$ <sup>9</sup>:

$$\mathbf{P}_t^{miss} = \mathbf{P}_{t(\nu)} + \mathbf{P}_t^{|\eta| > 4.2}. \quad (7)$$

A high-energy jet may also contain neutrinos that may carry a part of the total jet energy. The average values of this energy can be estimated from a simulation.

---

<sup>9</sup>This value is a part of true missing  $P_t$  in an experiment that includes the detector effects (see [1, 2]).

From the total jet transverse momentum  $\mathbf{P}_t^{\text{Jet}}$  we shall separate the part that, in principle, can be detected in the ECAL+HCAL calorimeter system and in the muon system. Let us denote this detectable part as  $\mathbf{P}_t^{\text{jet}}$  (small “j”!). So, we shall present the total jet transverse momentum  $\mathbf{P}_t^{\text{Jet}}$  as a sum of three parts:

1.  $\mathbf{P}_{t(\nu)}^{\text{Jet}}$ , containing the contribution of neutrinos that belong to the jet, i.e. a non-detectable part of jet  $P_t$  ( $i$  - neutrino):

$$\mathbf{P}_{t(\nu)}^{\text{Jet}} = \sum_{i \in \text{Jet}} \mathbf{P}_{t(\nu)}^i. \quad (8)$$

2.  $\mathbf{P}_{t(\mu)}^{\text{Jet}}$ , containing the contribution of jet muons to  $\mathbf{P}_t^{\text{Jet}}$  ( $i$  - muon):

$$\mathbf{P}_{t(\mu)}^{\text{Jet}} = \sum_{i \in \text{Jet}} \mathbf{P}_{t(\mu)}^i. \quad (9)$$

These muons make a weak signal in the calorimeter but their energy can be measured, in principle, in the muon system (in the region of  $|\eta| < 2.5$  in the case of D0 geometry). Due to the absence of the muon system and the tracker beyond the  $|\eta| < 2.5$  region, there exists a part of  $P_t^{\text{Jet}}$  caused by muons with  $|\eta| > 2.5$ . We denote this part as  $P_{t(\mu, |\eta| > 2.5)}^{\text{Jet}}$ . It is non-detectable part and can be considered as an analogue of  $P_{t(\nu)}^{\text{Jet}}$ .

As for both points 1 and 2, let us say in advance that the estimation of the average values of neutrino and muon contributions to  $P_t^{\text{Jet}}$  (see Section 4 and Tables 1–3 of Appendix 1) have shown that they are quite small: about 0.30% of  $\langle P_t^{\text{Jet}} \rangle_{\text{all}}$  is due to neutrinos and about 0.33% of  $\langle P_t^{\text{Jet}} \rangle_{\text{all}}$  is due to muons where “all” means averaging over all events including those without neutrinos and/or muons in jets. So, they together may cause approximately about 0.63% of the  $P_t^\gamma$  and  $P_t^{\text{jet}}$  disbalance if muon signal is lost.

3. Finally, as we have mentioned before, we use  $\mathbf{P}_t^{\text{jet}}$  to denote the part of  $\mathbf{P}_t^{\text{Jet}}$  which includes all detectable particles of the jet<sup>10</sup>, i.e. the sum of  $P_t$  of jet particles that may produce a signal in the calorimeter (*calo*) and muon system ( $\mu$ ):

$$\mathbf{P}_t^{\text{jet}} = \mathbf{P}_{t(\text{calo})}^{\text{Jet}} + \mathbf{P}_{t(\mu)}^{\text{Jet}}, \quad |\eta^\mu| < 2.5. \quad (10)$$

Thus, in the general case we can write for any  $\eta$  values:

$$\mathbf{P}_t^{\text{Jet}} = \mathbf{P}_t^{\text{jet}} + \mathbf{P}_{t(\nu)}^{\text{Jet}} + \mathbf{P}_{t(\mu, |\eta^\mu| > 2.5)}^{\text{Jet}}. \quad (11)$$

In the case of  $p\bar{p} \rightarrow \gamma + \text{jet} + X$  events the particles detected in the  $|\eta| < 4.2$  region may originate from the fundamental subprocesses (1a) and (1b) corresponding to LO diagrams shown in Fig. 1, as well as from the processes corresponding to NLO diagrams (like those in Figs. 2, 4 that include ISR and FSR), and also from the “underlying” event [1], of course.

So, for any event we separate the particles in the  $|\eta| < 4.2$  region into two subsystems. The first one consists of the particles belonging to the “ $\gamma + \text{Jet}$ ” system (here “*Jet*” denotes the jet with the highest  $P_t$ , greater 30 GeV/c, having the total transverse momentum  $\mathbf{P}_t^{\gamma+\text{Jet}}$  (large “*Jet*”, see (4)). The second subsystem involves all other (*O*) particles beyond the “ $\gamma + \text{Jet}$ ” system in the region, covered by the detector, i.e.  $|\eta| < 4.2$ . The total transverse momentum of this *O*-system are denoted as  $P_t^O$  and it is a sum of  $P_t$  of additional mini-jets (or clusters) and  $P_t$  of single hadrons, photons and leptons in the  $|\eta| < 4.2$  region. Since a part of neutrinos are also present among these leptons, the difference of  $\mathbf{P}_{t(\nu)}$  and  $\mathbf{P}_{t(\nu)}^{\text{Jet}}$  gives us the transverse momentum

<sup>10</sup>We shall consider the issue of charged particles contribution with small  $P_t$  into the total jet  $P_t$  while discussing the results of the full GEANT simulation (with account of the magnetic field effect) in our forthcoming papers.



$$\mathbf{P}_{\mathbf{t}(\nu)}^O = \mathbf{P}_{\mathbf{t}(\nu)} - \mathbf{P}_{\mathbf{t}(\nu)}^{Jet} \quad |\eta^\nu| < 4.2, \quad (12)$$

carried out by the neutrinos that do not belong to the jet but are contained in the  $|\eta| < 4.2$  region.

We denote by  $\mathbf{P}_{\mathbf{t}}^{out}$  a part of  $\mathbf{P}_{\mathbf{t}}^O$  that can be measured, in principle, in the detector. Thus,  $\mathbf{P}_{\mathbf{t}}^{out}$  is a sum of  $P_t$  of other mini-jets or, generally, clusters (with  $P_t^{clust}$  smaller than  $P_t^{Jet}$ ) and  $P_t$  of single hadrons ( $h$ ), photons ( $\gamma$ ) and electrons ( $e$ ) with  $|\eta| < 4.2$  and muons ( $\mu$ ) with  $|\eta^\mu| < 2.5$  that are out of the “ $\gamma + jet$ ” system. For simplicity these mini-jets and clusters will be called “clusters”<sup>11</sup>. So, for our “ $\gamma + jet$ ” events  $\mathbf{P}_{\mathbf{t}}^{out}$  is the following sum (all  $\{h, \gamma, e, \mu\} \notin Jet$ ):

$$\mathbf{P}_{\mathbf{t}}^{out} = \mathbf{P}_{\mathbf{t}}^{clust} + \mathbf{P}_{\mathbf{t}(h)}^{sing} + \mathbf{P}_{\mathbf{t}(\gamma)}^{nondir} + \mathbf{P}_{\mathbf{t}(e)} + \mathbf{P}_{\mathbf{t}(\mu, |\eta^\mu| < 2.5)}^O; \quad |\eta| < 4.2. \quad (13)$$

And thus, finally, we have:

$$\mathbf{P}_{\mathbf{t}}^O = \mathbf{P}_{\mathbf{t}}^{out} + \mathbf{P}_{\mathbf{t}(\nu)}^O + \mathbf{P}_{\mathbf{t}(\mu, |\eta^\mu| > 2.5)}^O. \quad (14)$$

With these notations we come to the following vector form [13] of the  $P_t$ - conservation law for the “ $\gamma + Jet$ ” event (where  $\gamma$  is a direct photon) as a whole (supposing that the jet and the photon are contained in the corresponding detectable regions):

$$\mathbf{P}_{\mathbf{t}}^\gamma + \mathbf{P}_{\mathbf{t}}^{Jet} + \mathbf{P}_{\mathbf{t}}^O + \mathbf{P}_{\mathbf{t}}^{|\eta| > 4.2} = 0 \quad (15)$$

with last three terms defined correspondingly by (11), (15) and (5) respectively.

### 3.2 Definition of selection cuts for physical variables.

1. We shall select the events with one jet and one “ $\gamma^{dir}$ -candidate” (in what follows we shall designate it as  $\gamma$  and call the “photon” for brevity)<sup>12</sup> with

$$P_t^\gamma \geq 40 \text{ GeV}/c \quad \text{and} \quad P_t^{Jet} \geq 30 \text{ GeV}/c. \quad (16)$$

In the simulation the ECAL signal is considered as a candidate for a direct photon if it fits inside one D0 calorimeter tower having size  $0.1 \times 0.1$  in the  $\eta - \phi$  space.

For most of our applications in Sections 4, 5 and 6 mainly the PYTHIA jetfinding algorithm LUCCELL will be used<sup>13</sup>. The jet cone radius  $R$  in the  $\eta - \phi$  space counted from the jet initiator cell (ic) is taken to be  $R_{ic} = ((\Delta\eta)^2 + (\Delta\phi)^2)^{1/2} = 0.7$ .

2. To suppress the contribution of background processes, i.e. to select mostly the events with “isolated” direct photons and to discard the events with fake “photons” (that may originate as  $\gamma^{dir}$ -candidates from meson decays, for instance), we restrict

a) the value of the scalar sum of  $P_t$  of hadrons and other particles surrounding a “photon” within a cone of  $R_{isol}^\gamma = ((\Delta\eta)^2 + (\Delta\phi)^2)^{1/2} = 0.7$  (“absolute isolation cut”)<sup>14</sup>

$$\sum_{i \in R} P_t^i \equiv P_t^{isol} \leq P_{tCUT}^{isol}; \quad (17)$$

<sup>11</sup>As was already mentioned in Introduction, these clusters are found by the LUCCELL jetfinder with the same value of the cone radius as for jets:  $R^{clust} = R^{jet} = 0.7$ .

<sup>12</sup>only in Section 8, devoted to the backgrounds, we shall denote  $\gamma^{dir}$ -candidate by  $\tilde{\gamma}$

<sup>13</sup>Comparison with the UA1 and UA2 jetfinding algorithms was presented in [19, 15, 16]

<sup>14</sup>We have found that  $S/B$  ratio with  $R_{isol}^\gamma = 0.7$  is in about 1.5 times better than with  $R_{isol}^\gamma = 0.4$  what is accompanied by only 10% of additional loss of the number of signal events.

b) the value of a fraction (“fractional isolation cut”)

$$\sum_{i \in R} P_t^i / P_t^\gamma \equiv \epsilon^\gamma \leq \epsilon_{CUT}^\gamma. \quad (18)$$

3. We accept only the events having no charged tracks (particles) with  $P_t > 5 \text{ GeV}/c$  within the  $R = 0.4$  cone around the  $\gamma^{dir}$ -candidate.

4. To suppress the background events with photons resulting from  $\pi^0, \eta, \omega$  and  $K_S^0$  meson decays, we require the absence of a high  $P_t$  hadron in the tower containing the  $\gamma^{dir}$ -candidate:

$$P_t^{hadr} \leq 7 \text{ GeV}/c. \quad (19)$$

At the PYTHIA level of simulation this cut may effectively take into account the imposing of an upper cut on the HCAL energy in the cells behind the ECAL signal cells fired by the direct photon. In real experimental conditions one can require that a fraction of the photon energy, deposited in ECAL to be greater than some value ( $\approx 0.95 - 0.96$  as it is now at D0).

5. We select the events with the vector  $\mathbf{P}_t^{Jet}$  being “back-to-back” to the vector  $\mathbf{P}_t^\gamma$  (in the plane transverse to the beam line) within  $\Delta\phi$  defined by the equation:

$$\phi_{(\gamma, jet)} = 180^\circ \pm \Delta\phi, \quad (20)$$

where  $\phi_{(\gamma, jet)}$  is the angle between the  $P_t^\gamma$  and  $P_t^{jet}$  vectors:  $\mathbf{P}_t^\gamma \mathbf{P}_t^{Jet} = P_t^\gamma P_t^{Jet} \cdot \cos(\phi_{(\gamma, jet)})$ ,  $P_t^\gamma = |\mathbf{P}_t^\gamma|$ ,  $P_t^{Jet} = |\mathbf{P}_t^{Jet}|$ . The cases  $\Delta\phi \leq 17^\circ, 11^\circ, 6^\circ$  are considered in this paper ( $6^\circ$  is approximately one D0 calorimeter tower size in  $\phi$ ).

6. As we have already mentioned in Section 3.1, one can expect reasonable results of the jet energy calibration procedure modeling and subsequent practical realization only if one uses a set of selected events with small  $P_t^{miss}$  (see (7) and (25)). So, we also use the following cut:

$$P_t^{miss} \leq P_{tCUT}^{miss}. \quad (21)$$

The aim of the event selection with small  $P_t^{miss}$  is quite obvious: we need a set of events with a reduced  $P_t^{Jet}$  uncertainty due to a possible presence of a non-detectable particle contribution to a jet and due to the term  $P_t^{|\eta|>4.2}$  (see (7) and (25)).

The influence of  $P_{tCUT}^{miss}$  on the selection of events with a reduced value of the total sum of neutrino contribution into  $P_t^{Jet}$  is studied in Section 4.

7. The initial and final state radiations (ISR and FSR) manifest themselves most clearly as some final state mini-jets or clusters activity. To suppress it, we impose a new cut condition that was not formulated in an evident form in previous experiments: we choose the “ $\gamma + jet$ ” events that do not have any other jet-like or cluster high  $P_t$  activity by selecting the events with the values of  $P_t^{clust}$  (the cluster cone  $R_{clust}(\eta, \phi) = 0.7$ ), being lower than some threshold  $P_{tCUT}^{clust}$  value, i.e. we select the events with

$$P_t^{clust} \leq P_{tCUT}^{clust} \quad (22)$$

( $P_{tCUT}^{clust} = 15, 10, 5 \text{ GeV}/c$  are most effective as will be shown in Sections 6–8). Here, in contrast to [13]–[17], the clusters are found by one and the same jetfinder LUCCELL while three different jetfinders UA1, UA2 and LUCCELL are used to find the jet ( $P_t^{Jet} \geq 30 \text{ GeV}/c$ ) in the event.

8. Now we pass to another new quantity (proposed also for the first time in [13]–[17]) that can be measured at the experiment. We limit the value of the modulus of the vector sum of  $\mathbf{P}_t$  of all particles, except those of the “ $\gamma + jet$ ” system, that fit into the region  $|\eta| < 4.2$  covered by the ECAL and HCAL, i.e., we limit the signal in the cells “beyond the jet and photon” region by the

following cut:

$$\left| \sum_{i \notin Jet, \gamma-dir} \mathbf{P}_t^i \right| \equiv P_t^{out} \leq P_{tCUT}^{out}, \quad |\eta^i| < 4.2. \quad (23)$$

The importance of  $P_{tCUT}^{out}$  and  $P_{tCUT}^{clust}$  for selection of events with a good balance of  $P_t^\gamma$  and  $P_t^{jet}$  and for the background reduction will be demonstrated in Sections 7 and 8.

Below the set of selection cuts 1 – 8 will be referred to as “Selection 1”. The last two of them, 7 and 8, are new criteria [13] not used in previous experiments.

9. In addition to them one more new object, introduced in [13] – [17] and named an “isolated jet”, will be used in our analysis. i.e. we shall require the presence of a “clean enough” (in the sense of limited  $P_t$  activity) region inside the ring of  $\Delta R = 0.3$  width (or approximately of a size of three calorimeter towers) around the jet. Following this picture, we restrict the ratio of the scalar sum of transverse momenta of particles belonging to this ring, i.e.

$$P_t^{ring} / P_t^{jet} \equiv \epsilon^{jet} \leq \epsilon_0^{jet}, \quad \text{where} \quad P_t^{ring} = \sum_{i \in 0.7 < R < 1.0} |\mathbf{P}_t^i|. \quad (24)$$

( $\epsilon_0^{jet}$  is chosen to be 3 – 5%, see Sections 7 and 8).

The set of cuts 1 – 9 will be called in what follows “Selection 2”.

The exact values of the cut parameters  $P_{tCUT}^{isol}$ ,  $\epsilon_{CUT}^\gamma$ ,  $\epsilon^{jet}$ ,  $P_{tCUT}^{clust}$ ,  $P_{tCUT}^{out}$  will be specified below, since they may be different, for instance, for various  $P_t^\gamma$  intervals (being looser for higher  $P_t^\gamma$ ).

### 3.3 The scalar form of the $P_t$ balance equation and the jet energy calibration procedure.

Let us rewrite the basic  $P_t$ -balance equation (15) of Section 3.1 with the notations introduced here in the scalar form more suitable for the following applications:

$$\frac{P_t^\gamma - P_t^{Jet}}{P_t^\gamma} = (1 - \cos\Delta\phi) + P_t(O+\eta > 4.2) / P_t^\gamma, \quad (25)$$

where  $P_t(O+\eta > 4.2) \equiv (\mathbf{P}_t^O + \mathbf{P}_t^{|\eta|>4.2}) \cdot \mathbf{n}^{Jet}$  with  $\mathbf{n}^{Jet} = \mathbf{P}_t^{Jet} / P_t^{Jet}$ .

As will be shown in Section 7, the first term on the right-hand side of equation (25), i.e.  $(1 - \cos\Delta\phi)$  is negligibly small as compared with the second term<sup>15</sup> and tends to decrease fast with growing  $P_t^{Jet}$ . So, in this case the main contribution to the  $P_t$  disbalance in the “ $\gamma + jet$ ” system is caused by the term  $P_t(O+\eta > 4.2) / P_t^\gamma$ .

$P_t^{Jet}$  can be easily expressed from equation (25) through:

$$P_t^{Jet} = \alpha \cdot P_t^\gamma \quad (26)$$

with  $\alpha$  defined as  $\alpha = \cos\Delta\phi - P_t(O+\eta > 4.2) / P_t^\gamma$ .

Having defined in every selected event  $P_t^{Jet}$  from equation (26) one can determine calibration coefficients  $\{C_i\}$  via minimizing of a standard deviation of the function:

$$F = \sum_{j=1}^{N_{event}} \left( \frac{P_t^{Jet} - \sum_{i=1}^{N_l} C_i P_t^{i,c}}{\Delta P_t^{Jet}} \right)^2 \quad (27)$$

---

<sup>15</sup>in a case of Selection 1

In this expression  $N_l$  is a number of calorimeter layers <sup>16</sup>,  $P_t^{i,c}$  is energy deposition in the  $i$ -th calorimeter layer and  $\Delta P_t^{Jet}$  is the error on  $P_t^{Jet}$  caused by uncertainty in  $\alpha$  ( $\Delta\alpha$ ) and uncertainty due to limited accuracy of  $P_t^\gamma$  determination ( $\Delta P_t^\gamma$ ) <sup>17</sup>. So, one can write (see (26)):

$$\Delta P_t^{Jet} = \Delta\alpha \oplus \Delta P_t^\gamma \quad (28)$$

Obtained in this way the calibration coefficients  $\{C_i\}$  in the selected “ $\gamma + jet$ ” events for every bin of  $\eta^{jet}$  and calorimeter  $P_t^{jet}$  then should be applied to energy depositions in each layer  $P_t^{i,c}$  of a found jet in any event to reconstruct a jet transverse momentum at the particle level. The accuracy of such a reconstruction will directly depend on the accuracy of the coefficients  $\{C_i\}$ . The latter, in their turn, are caused by the error of  $\Delta P_t^{Jet}$  (see (27)) <sup>18</sup>.

Having determined relatively perfectly a photon energy scale the  $\Delta P_t^\gamma$ , the  $\Delta P_t^{Jet}$  uncertainty will be mainly defined by  $\Delta\alpha$  (namely by term  $P_t(O+\eta > 4.2)/P_t^\gamma$  of equation (25)).

#### 4. ESTIMATION OF A NON-DETECTABLE PART OF $P_t^{Jet}$ AND $P_t^{miss}$ SPECTRA.

*It is shown that by imposing an upper cut on the missing transverse momentum  $P_t^{miss} < 10 \text{ GeV}/c$  one can reduce the correction to the measurable part of  $P_t^{jet}$  due to neutrino contribution down to the value of  $\Delta_\nu = \langle P_{t(\nu)}^{Jet} \rangle_{all \text{ events}} = 0.1 \text{ GeV}/c$  in all intervals of  $P_t^\gamma$ .*

In Section 3.1 we have divided the transverse momentum of a jet, i.e.  $P_t^{Jet}$ , into two parts, a detectable  $P_t^{jet}$  and non-detectable ( $P_t^{Jet} - P_t^{jet}$ ), consisting of  $P_{t(\nu)}^{Jet}$  and  $P_{t(\mu,|\eta|>2.5)}^{Jet}$  (see (11)). In the same way, according to equation (15), we divided the transverse momentum  $P_t^O$  of “other particles”, that are out of  $\gamma^{dir} + jet$  system, into a detectable part  $P_t^{out}$  and a non-detectable part consisting of the sum of  $P_{t(\nu)}^O$  and  $P_{t(\mu,|\eta|>2.5)}^O$  (see (15)).

We shall estimate here what part of  $P_t^{Jet}$  may be carried out by non-detectable particles (mainly neutrinos originating from weak decays) <sup>19</sup>.

We shall consider the case of switched-on decays of  $\pi^\pm$  and  $K^\pm$  mesons <sup>20</sup>. Here  $\pi^\pm$  and  $K^\pm$  meson decays are allowed inside the solenoid volume with the barrel radius  $R_B = 80 \text{ cm}$  and the distance from the interaction vertex to Endcap along the  $z$ -axis  $L = 130 \text{ cm}$  (D0 geometry).

For this aim we shall use the bank of the signal “ $\gamma + jet$ ” events, i.e. caused by subprocesses (1a) and (1b), generated for three  $P_t^\gamma$  intervals:  $40 < P_t^\gamma < 50$ ,  $70 < P_t^\gamma < 90$  and  $90 < P_t^\gamma < 140 \text{ GeV}/c$  and selected with conditions (16)–(23) (Selection 1) and the following cut values:

$$P_{tCUT}^{isol} = 4 \text{ GeV}/c, \quad \epsilon_{CUT}^\gamma = 7\%, \quad \Delta\phi < 17^\circ, \quad P_{tCUT}^{clust} = 30 \text{ GeV}/c. \quad (29)$$

Here the cut  $P_{tCUT}^{clust} = 30 \text{ GeV}/c$  has the meaning of a very weak restriction on mini-jets or clusters activity. No restriction was imposed on the  $P_t^{out}$  value. The results of analysis of these events, based on the application of LUCCELL jetfinder, are presented in Fig. 5.

<sup>16</sup> $N_l = 8$  at D0 (4 for ECAL and 4 for HCAL).

<sup>17</sup>For instance, in the central region of D0 calorimeter ( $|\eta| < 0.9$ ) electron/photon energy resolution can be written through  $\sigma/E = 23\%/\sqrt{(E)} \oplus 20\%/E \oplus 0.4\%$ .

<sup>18</sup>Other possibility, based on the usage of artificial neural networks (ANN), was also considered (see [27] and [28]). In this approach one can obtain a better energy resolution of the reconstructed jet but it requires a bigger statistics for ANN training. The calibration coefficients  $\{C_i\}$  in this case will be replaced by set of ANN weights  $\{w_{ij}\}$  and function (27) — by a more complicated expression.

<sup>19</sup>In [17] and [26] it was shown that main source of high  $P_t$  neutrinos in background processes are  $W^\pm$  decays, which also contain  $e^\pm$  that in its turn may fake direct photons.

<sup>20</sup>According to the PYTHIA default agreement,  $\pi^\pm$  and  $K^\pm$  mesons are stable.

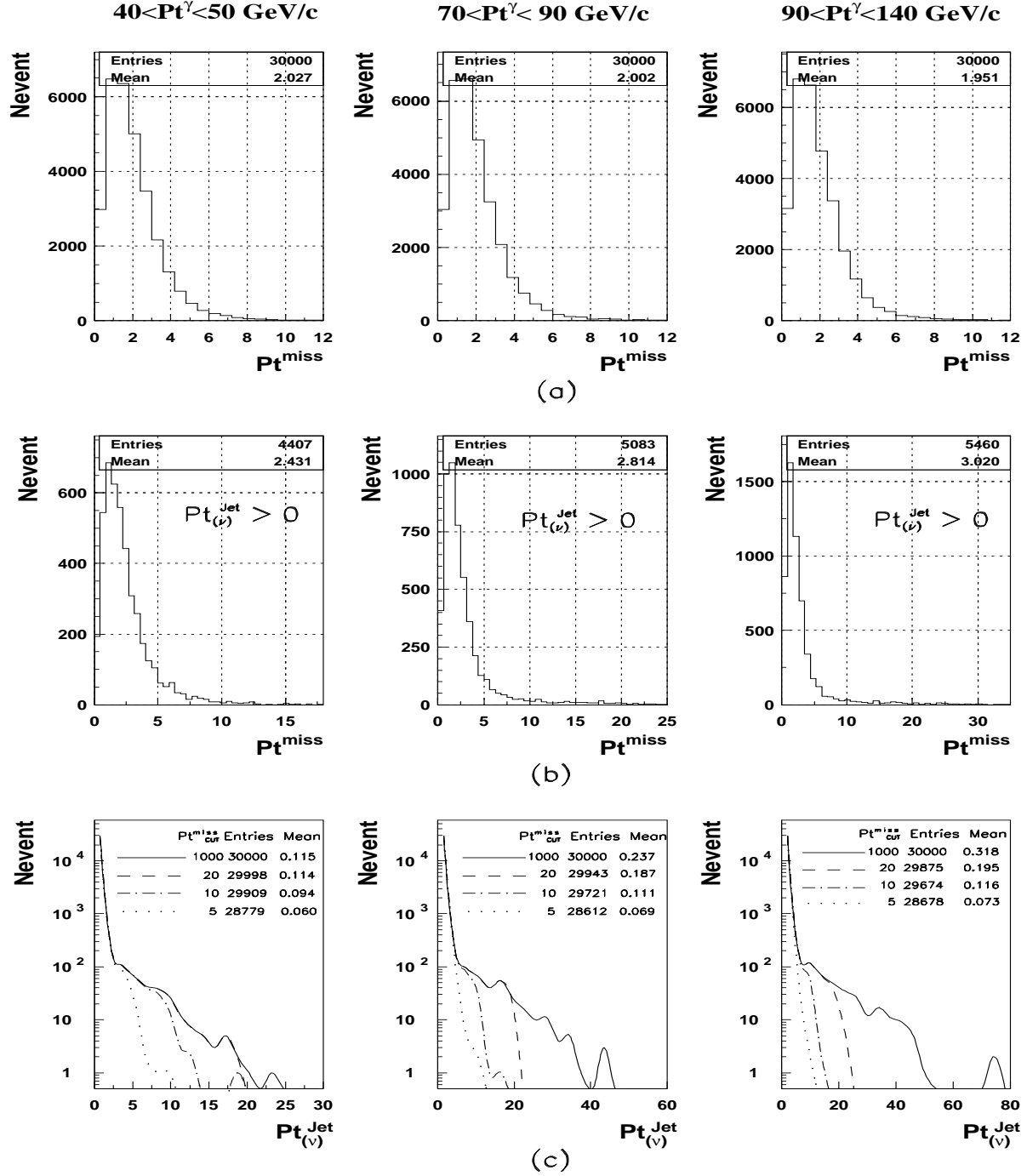


Fig. 5: a)  $P_t^{miss}$  spectra in all events; b)  $P_t^{miss}$  spectra in events having jets with non-zero  $P_t$  neutrinos, i.e.  $P_t^{Jet} > 0$ ; c)  $P_t^{Jet}$  spectra and their mean values dependence on the values of  $P_t^{miss}$  in various  $P_t^\gamma$  ( $\approx P_t^{Jet}$ ) intervals.  $\pi^\pm$  and  $K^\pm$  meson decays are allowed inside the solenoid of  $R = 80$  cm and  $L = 130$  cm ( $P_t^{clust} = 30$  GeV/c).

The first row of Fig. 5 contains  $P_t^{miss}$  spectra in the “ $\gamma + jet$ ” events for different  $P_t^\gamma$  intervals and demonstrates (to a good accuracy) their practical independence on  $P_t^\gamma$ .

In the second row of Fig. 5 we present the spectra of  $P_t^{miss}$  for those events (denoted as  $P_{t(\nu)}^{Jet} > 0$ ) which contain jets having neutrinos, i.e. having a non-zero  $P_{t(\nu)}^{Jet}$  component of  $P_t^{Jet}$ . These figures show a very weak dependence of the  $P_t^{miss}$  spectrum on the direct photon  $P_t^\gamma$ . Comparison of the number of entries in the second row plots of Fig. 5 with those in the first row allows to conclude that the part of events with the jet having the non-zero neutrinos contribution is about 15 – 18%.

The effect of imposing general  $P_{tCUT}^{miss}$  in each event of our sample is shown in the third row of Fig. 5. The upper cut  $P_{tCUT}^{miss} = 1000 \text{ GeV}/c$  means the absence of any upper limit for  $P_t^{Jet}$ . The most important illustrative fact that in the absence of any restriction on  $P_t^{miss}$  the total neutrino  $P_t$  inside the jet averaged over all events can be as large as  $P_{t(\nu)}^{Jet} \approx 0.32 \text{ GeV}/c$  at  $90 < P_t^\gamma < 140 \text{ GeV}/c$  (see the right-hand plot of the third row in Fig. 5). In the  $40 < P_t^{Jet} < 50 \text{ GeV}/c$  interval, we have already a very small mean value of  $P_{t(\nu)}^{Jet}$  equal to  $0.12 \text{ GeV}/c$  even without imposing any  $P_{tCUT}^{miss}$ . From the same plots of the third row of Fig. 5 we see that with general  $P_{tCUT}^{miss} = 10 \text{ GeV}/c$  the average correction due to neutrino contribution is  $0.1 \text{ GeV}/c$  in all three intervals of  $P_t^\gamma$ .

At the same time, as it was demonstrated in [17] and [26], this cut essentially reduces the admixture of the  $e^\pm$ -events, in which  $e^\pm$ , mainly originating from the  $W^\pm \rightarrow e^\pm \nu$  weak decays, may fake the direct photon signal. These events are characterized by big values of  $P_t^{miss}$  (it is higher, on the average, by about one order of magnitude than in the signal “ $\gamma^{dir} + jet$ ” events) that may worsen the jet calibration accuracy.

The situation, analogous to neutrino, holds for the  $P_{t(\mu)}^{Jet}$  contribution.

The detailed information about the values of non-detectable  $P_{t(\nu)}^{Jet}$  averaged over all events (no cut on  $P_t^{miss}$  was used) as well as about mean  $P_t$  values of muons belonging to jets  $\langle P_{t(\mu)}^{Jet} \rangle$  is presented in Tables 1–3 of Appendix 1 for the sample of events with jets which are entirely contained in the central region of the calorimeter ( $|\eta^{jet}| < 0.7$ ) and found by UA1 jetfinder. In these tables the ratio of the number of events with non-zero  $P_{t(\nu)}^{Jet}$  to the total number of events is denoted by  $R_{event}^{\nu \in Jet}$  and the ratio of the number of events with non-zero  $P_{t(\mu)}^{Jet}$  to the total number of events is denoted by  $R_{event}^{\mu \in Jet}$ .

The quantity  $P_t^{miss}$  in events with  $P_{t(\nu)}^{Jet} > 0$  is denoted in these tables as  $P_{t\nu \in Jet}^{miss}$  and is given there for three  $P_t^\gamma$  intervals ( $40 < P_t^\gamma < 50$ ,  $70 < P_t^\gamma < 90$  and  $90 < P_t^\gamma < 140$ ) and  $P_{tCUT}^{clust} = 30, 20, 15, 10, 5 \text{ GeV}/c$ )<sup>21</sup>

## 5. EVENT RATES FOR DIFFERENT $P_t^\gamma$ AND $\eta^{jet}$ INTERVALS.

The number of “ $\gamma + jet$ ” events distribution over  $P_t^\gamma$  and  $\eta^\gamma$  is shown here. It is found that in each interval of the  $\Delta P_t^\gamma = 10 \text{ GeV}/c$  width the rates decrease by a factor more than 2. The number of events with jets which transverse momentum are completely (or with 5% accuracy) contained in CC, IC, EC and FC regions are presented in Tables 5, 6 for integrated luminosity  $L_{int} = 300 \text{ pb}^{-1}$ .

<sup>21</sup>Note that the values of  $P_t^{miss}$  and  $P_{t\nu \in Jet}^{miss}$  in the plots of Fig. 5 are slightly different from those of Appendix 1 as the numbers in from Fig. 5 were found for events in the whole  $|\eta| < 4.2$  region.

## 5.1 Dependence of distribution of the number of events on the “back-to-back” angle $\phi_{(\gamma, jet)}$ and on $P_t^{ISR}$ .

The definitions of the physical variables introduced in Sections 2 and 3 allow to study a possible way to select the events with a good  $P_t^\gamma$  and  $P_t^{Jet}$  balance. Here we shall be interested to get (by help of PYTHIA generator and the theoretical models therein) the form of the spectrum of the variable  $P_t^{56}$  (see (3)) (which is approximately proportional to  $P_t^{ISR}$  up to the value of intrinsic parton transverse momentum  $k_t$  inside a proton) at different values of  $P_t^\gamma$ . For this aim four samples of “ $\gamma + jet$ ” events were generated by using PYTHIA with 2 QCD subprocesses (1a) and (1b) being included simultaneously. In what follows we shall call these events as “signal events”. The generations were done with the values of the PYTHIA parameter CKIN(3)( $\equiv \hat{p}_\perp^{min}$ ) equal to 20, 25, 35 and 45  $GeV/c$  in order to cover four  $P_t^\gamma$  intervals: 40–50, 50–70, 70–90 and 90–140  $GeV/c$ , respectively<sup>22</sup>. Each sample in these  $P_t^\gamma$  intervals had a size of  $5 \cdot 10^6$  events. The cross sections for the two subprocesses were found to be as given in Table 1.

Table 1: The cross sections (in *microbarns*) of the  $qg \rightarrow q + \gamma$  and  $q\bar{q} \rightarrow g + \gamma$  subprocesses for four  $P_t^\gamma$  intervals.

Subprocess type	$\hat{p}_\perp^{min} (GeV/c)$			
	20	25	35	45
$qg \rightarrow q + \gamma$	$0.97 \cdot 10^{-2}$	$4.78 \cdot 10^{-3}$	$1.36 \cdot 10^{-3}$	$4.95 \cdot 10^{-4}$
$q\bar{q} \rightarrow g + \gamma$	$0.20 \cdot 10^{-2}$	$0.96 \cdot 10^{-3}$	$0.35 \cdot 10^{-3}$	$1.56 \cdot 10^{-4}$
Total	$1.17 \cdot 10^{-2}$	$5.75 \cdot 10^{-3}$	$1.71 \cdot 10^{-3}$	$6.51 \cdot 10^{-4}$

For our analysis we used Selection 1 (see (16)–(23)) and the values of cut parameters (32).

In Fig. 6 we present the  $P_t^{56}$  spectra for two most illustrative cases of  $P_t^\gamma$  intervals  $40 < P_t^\gamma < 50 GeV/c$  (two upper plots) and  $70 < P_t^\gamma < 90 GeV/c$  (two bottom plots). The distributions of the number of events for the integrated luminosity  $L_{int} = 300 pb^{-1}$  in different  $P_t^{56}$  intervals and for different “back-to-back” angle intervals  $\phi_{(\gamma, jet)} = 180^\circ \pm \Delta\phi$  ( $\Delta\phi \leq 17^\circ$  and  $6^\circ$  as well as without any restriction on  $\Delta\phi$ , i.e. for the whole  $\phi$  interval  $\Delta\phi \leq 180^\circ$ )<sup>23</sup> are given there. The LUCCELL jetfinder was used for determination of jets and clusters<sup>24</sup>. Left column of Fig. 6 correspond to  $P_t^{clust} < 30 GeV/c$  and serve as an illustration since it is rather a weak cut condition, while right column of Fig. 6 correspond to a more restrictive selection cut  $P_{tCUT}^{clust} = 5 GeV/c$ .

Tables 2 and 3 show the number of events (at  $L_{int} = 300 pb^{-1}$ ) left after application different cuts on the angle  $\Delta\phi$  for two values of  $P_{tCUT}^{clust}$ . In the case of weak restriction  $P_t^{clust} < 30 GeV/c$  we can see that for the  $40 \leq P_t^\gamma \leq 50 GeV/c$  interval about 75% of events are concentrated in the  $\Delta\phi < 17^\circ$  range, while 41% of events are in the  $\Delta\phi < 6^\circ$  range. As for  $70 \leq P_t^\gamma \leq 90 GeV/c$ : about 86% of events have  $\Delta\phi < 17^\circ$  and 50% of them have  $\Delta\phi < 6^\circ$ .

A tendency of distributions of the number of signal “ $\gamma + jet$ ” events to be very rapidly concentrated in a rather narrow back-to-back angle interval  $\Delta\phi < 17^\circ$  as  $P_t^\gamma$  grows becomes more distinct with a more restrictive cut on the cluster  $P_t$ . From Table 3 we see that in the first interval  $40 \leq P_t^\gamma \leq 50 GeV/c$  more than 99% of the events, selected with  $P_{tCUT}^{clust} = 5 GeV/c$ , have  $\Delta\phi < 17^\circ$ , while 76% of them are in the  $\Delta\phi < 6^\circ$  range. It should be mentioned that after application of cut  $P_{tCUT}^{clust} = 5 GeV/c$  only about 40% of events remain as compared with a case of  $P_{tCUT}^{clust} = 30 GeV/c$ . For  $70 \leq P_t^\gamma \leq 90 GeV/c$  more than 90% of the events, subject to the cut  $P_{tCUT}^{clust} = 5 GeV/c$ , have  $\Delta\phi < 6^\circ$ . It means that while suppressing cluster or mini-jet activity

<sup>22</sup> $\langle k_t \rangle$  was taken to be fixed at the PYTHIA default value, i.e.  $\langle k_t \rangle = 0.44 GeV/c$

<sup>23</sup>The value  $\Delta\phi = 6^\circ$  approximately coincides with one D0 HCAL tower size in the  $\phi$ -plane.

<sup>24</sup>More details connected with UA1 jetfinder application can be found in Section 7 and Appendix 2 for a jet contained in CC region.

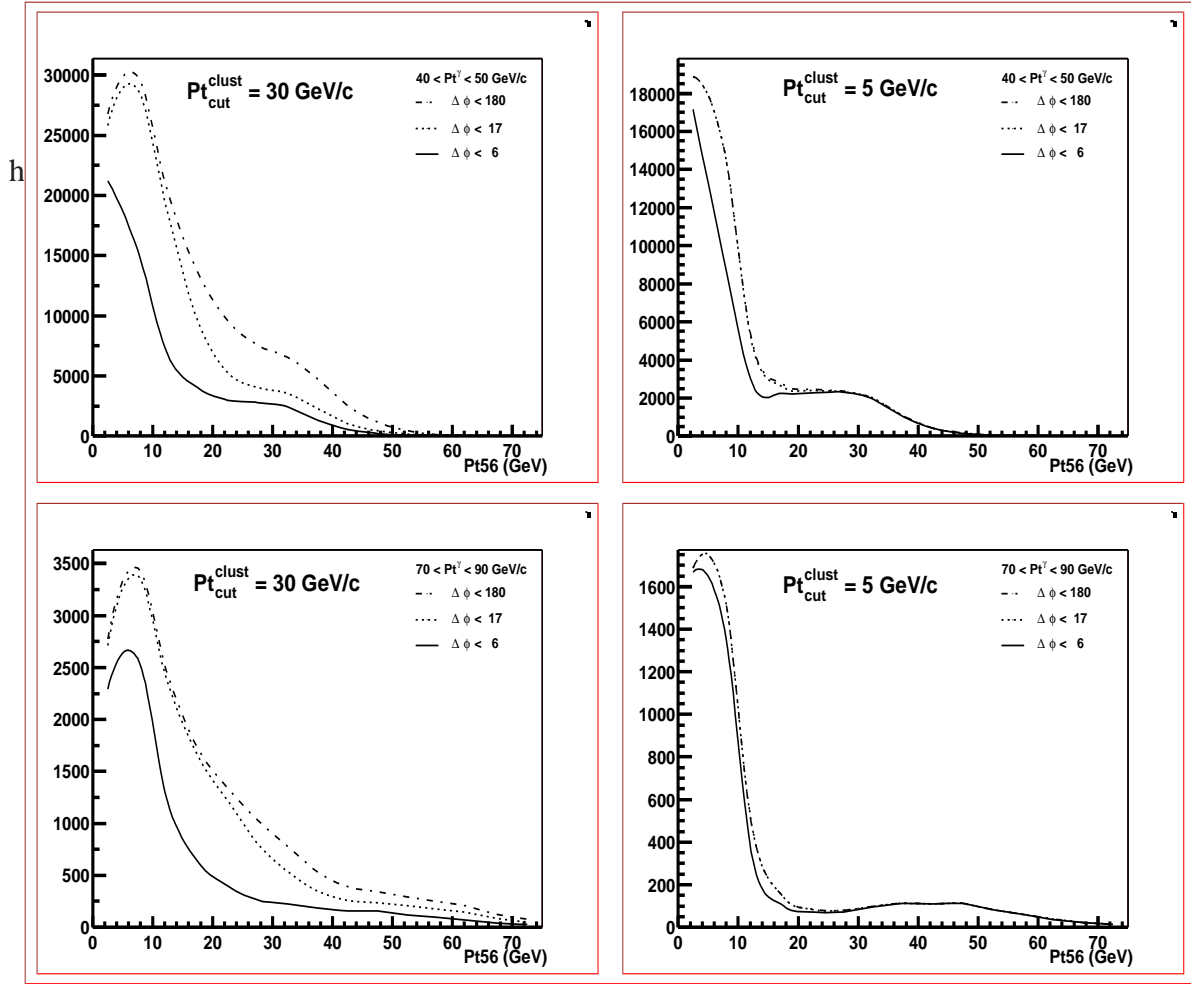


Fig. 6: A dependence of the number of events (at  $L_{int} = 300 \text{ pb}^{-1}$ ) on  $\Delta\phi_{max}$  and  $P_t^{clust}$  for two  $P_t^\gamma$  intervals:  $40 \leq P_t^\gamma \leq 50 \text{ GeV}/c$  for two upper plots and  $70 \leq P_t^\gamma \leq 90 \text{ GeV}/c$  for two bottom plots.

Table 2: A dependence of the number of events on  $\Delta\phi_{max}$  and on  $P_t^\gamma$  for  $L_{int} = 300 \text{ pb}^{-1}$ ,  $P_{tCUT}^{clust} = 30 \text{ GeV}/c$ .

$P_t^{56}$ (GeV/c)	$\Delta\phi_{max}$			
	180°	17°	11°	6°
40 – 50	110691	82913	68921	44830
50 – 70	71075	55132	45716	29692
70 – 90	14853	12727	10919	7418
90 – 140	5887	5534	4974	3655

Table 3: A dependence of the number of events on  $\Delta\phi_{max}$  and on  $P_t^\gamma$  for  $L_{int} = 300 \text{ pb}^{-1}$ ,  $P_{tCUT}^{clust} = 5 \text{ GeV}/c$ .

$P_t^{56}$ (GeV/c)	$\Delta\phi_{max}$			
	180°	17°	11°	6°
40 – 50	37576	37235	35473	27025
50 – 70	19056	19017	18651	15149
70 – 90	3773	3773	3755	3387
90 – 140	1525	1525	1524	1468



by imposing  $P_{tCUT}^{clust} = 5 \text{ GeV}/c$  we can select the sample of events with a clean “back-to-back” (within  $17^\circ$  in  $\phi$ ) topology of  $\gamma$  and jet orientation <sup>25</sup>.

Thus one can conclude that PYTHIA simulation predicts that at Tevatron energies most of the “ $\gamma + jet$ ” events (more than 75%) may have the vectors  $\mathbf{P}_t^\gamma$  and  $\mathbf{P}_t^{jet}$  being back-to-back within  $\Delta\phi < 17^\circ$  after imposing  $P_{tCUT}^{clust} = 30 \text{ GeV}/c$ . The cut  $P_{tCUT}^{clust} = 5 \text{ GeV}/c$  significantly improves this tendency <sup>26</sup>.

It is worth mentioning that this picture reflects the predictions of one of the generators based on the approximate LO values for the cross section. It may change if the next-to-leading order or soft physics <sup>27</sup> effects are included.

From Fig. 6 one can see that in the case when there are no restrictions on  $P_t^{clust}$  the  $P_{t56}$  spectrum becomes a bit wider for larger values of  $P_t^\gamma$ .

At the same time, one can conclude from the comparison of left and right upper plots that the width of the most populated part of the  $P_{t56}$  (or  $P_t^{ISR}$ ) spectrum reduces by about 40% with restricting  $P_{tCUT}^{clust}$ . So, for  $\Delta\phi_{max} = 17^\circ$  we see that it drops from  $0 < P_{t56} < 20 \text{ GeV}/c$  for  $P_{tCUT}^{clust} = 30 \text{ GeV}/c$  to a narrower interval of  $0 < P_{t56} < 10 - 12 \text{ GeV}/c$  for the  $P_{tCUT}^{clust} = 5 \text{ GeV}/c$ . At higher  $P_t^\gamma$  intervals (two bottom plots) for the same value  $\Delta\phi_{max} = 17^\circ$  the reduction factor of the  $P_{t56}$  spectrum width is more than two (from  $0 < P_{t56} < 30 \text{ GeV}/c$  for  $P_{tCUT}^{clust} = 30 \text{ GeV}/c$  to  $0 < P_{t56} < 12 - 15 \text{ GeV}/c$  for  $P_{tCUT}^{clust} = 5 \text{ GeV}/c$ ).

Thus, we can summarize that the PYTHIA generator predicts an increase in the  $P_t^{ISR}$  spectrum with growing  $P_t^\gamma$  and this increase can be substantially reduced by imposing a restrictive cut on  $P_t^{clust}$  <sup>28</sup>. Unfortunately,  $P_t^{ISR}$  cannot be completely suppressed by  $\Delta\phi$  and  $P_t^{clust}$  cuts alone <sup>29</sup>. That is why we prefer to use the  $P_t$  balance equation for the event as a whole (see equations (15) and (25) of Sections 3.1 and 3.3), i.e. an equation that takes into account the ISR and FSR effects, rather than balance equation (2) for fundamental processes (1a) and (1b) as discussed in Section 2.1 <sup>30</sup>.

## 5.2 $P_t^\gamma$ and $\eta^\gamma$ dependence of event rates.

Here we shall present the number of events for different  $P_t^\gamma$  and  $\eta^\gamma$  intervals as predicted by PYTHIA simulation with weak cuts defined mostly by (32) with only change of  $P_{tCUT}^{clust}$  value from 30 to 10  $\text{GeV}/c$ . The lines of Table 4 correspond to  $P_t^\gamma$  intervals and the columns to  $\eta^\gamma$  intervals. The last column of this table contains the total number of events (at  $L_{int} = 300 \text{ pb}^{-1}$ ) in the whole ECAL  $\eta^\gamma$ -region  $|\eta^\gamma| < 2.5$  for a given  $P_t^\gamma$  interval. We see that the number of events decreases fast with growing  $P_t^\gamma$  (by more than 50% for each subsequent interval).

## 5.3 Estimation of “ $\gamma + jet$ ” event rates for different calorimeter regions.

Since a jet is a wide-spread object, the  $\eta^{jet}$  dependence of rates for different  $P_t^\gamma$  intervals will be presented in a different way than in Section 5.2. Namely, Tables 5–6 include the rates of

<sup>25</sup>Unfortunately, as it will be discussed below and is seen in Fig. 6, it does not mean that  $P_{tCUT}^{clust}$  allows to suppress completely the ISR. (see also the event spectra over  $P_t^{clust}$  in Fig. 7 of the following Section 6.)

<sup>26</sup>A growth of  $P_t^\gamma$  produces the same effect, as is seen from Tables 2 and 3 and will be demonstrated in more detail in Section 6 and Appendix 2.

<sup>27</sup>We thank E. Pilon and J. Ph. Joliet for the information about new Tevatron data on this subject and for clarifying the importance of NLO corrections and soft physics effects.

<sup>28</sup>for more details see Sections 6 and 7

<sup>29</sup>In Sections 7, 8 the effect of the additional  $P_{tCUT}^{out}$  will be discussed.

<sup>30</sup>In Section 6 we shall study a behavior of each term that enter equation (25) in order to find the criteria that would allow to select events with a good balance of  $P_t^\gamma$  and  $P_t^{jet}$ .

Table 4: Rates for  $L_{int} = 300 \text{ pb}^{-1}$  for different  $P_t^\gamma$  intervals and  $\eta^\gamma$  ( $P_{tCUT}^{clust} = 10 \text{ GeV}/c$  and  $\Delta\phi \leq 17^\circ$ ).

$P_t^\gamma$ (GeV/c)	$ \eta^\gamma $ intervals							all $\eta^\gamma$
	0.0-0.4	0.4-0.7	0.7-1.1	1.1-1.4	1.4-1.8	1.8-2.1	2.1-2.5	0.0-2.5
40 – 50	10978	11232	10604	10337	9662	8051	5806	66679
50 – 60	4483	4210	4489	3938	3624	2814	1562	25121
60 – 70	2028	1732	1890	1587	1442	984	607	10270
70 – 80	949	931	937	753	637	392	170	4770
80 – 90	508	513	469	363	309	180	62	2405
90 – 100	302	287	252	201	149	80	25	1295
100 – 120	285	280	257	189	125	61	11	1207
120 – 140	134	121	98	63	38	9	1	465
40 – 140	19662	19302	18992	17427	15986	12571	8245	112216

Table 5: Selection 1.  $\Delta P_t^{jet}/P_t^{jet} = 0.00$  ( $P_{tCUT}^{clust} = 10 \text{ GeV}/c$ ,  $\Delta\phi \leq 17^\circ$  and  $L_{int} = 300 \text{ pb}^{-1}$ ).

$P_t^\gamma$	CC	CC → IC	IC	IC → CC, EC	EC	EC → IC, FC	FC	FC → EC
40 – 50	9965	13719	8152	22225	617	8854	554	1912
50 – 60	4009	5597	3104	8791	207	2766	109	413
60 – 70	1754	2515	1339	3615	71	979	14	93
70 – 80	930	1195	651	1593	21	348	1	23
80 – 90	503	596	328	811	9	136	0	6
90 – 100	283	352	165	421	3	59	0	1
100 – 120	263	351	137	389	2	37	0	0
120 – 140	118	143	50	142	1	7	0	0
40 – 140	17822	24462	13927	37988	930	13184	678	2448

Table 6: Selection 1.  $\Delta P_t^{jet}/P_t^{jet} \leq 0.05$  ( $P_{tCUT}^{clust} = 10 \text{ GeV}/c$ ,  $\Delta\phi \leq 17^\circ$  and  $L_{int} = 300 \text{ pb}^{-1}$ ).

$P_t^\gamma$	CC	CC → IC	IC	IC → CC, EC	EC	EC → IC, FC	FC	FC → EC
40 – 50	17951	5733	20631	9746	4174	5296	1280	1186
50 – 60	7466	2141	8313	3583	1403	1570	253	269
60 – 70	3405	863	3553	1401	492	558	39	68
70 – 80	1699	426	1667	577	179	190	6	17
80 – 90	902	197	838	301	75	71	3	4
90 – 100	528	107	440	146	31	31	0	0
100 – 120	537	98	384	142	19	20	0	0
120 – 140	223	37	143	48	5	3	0	0
40 – 140	32701	9603	35971	15943	6377	7738	1582	1545

events ( $L_{int} = 300 \text{ pb}^{-1}$ ) for different  $\eta^{jet}$  intervals, covered by the central, intercryostat, end and forward (CC, IC, EC and FC) parts of the calorimeter and for different  $P_t^\gamma (\approx P_t^{jet})$  intervals.

No restrictions on other parameters are used. The first column of Table 5 *CC* gives the number of events with the jets (found by the LUCCELL jetfinding algorithm of PYTHIA), all particles of which are comprised entirely (100%)<sup>31</sup> in the CC part and there is a 0% sharing of  $P_t^{jet}$  ( $\Delta P_t^{jet} = 0$ ) between the CC and the neighboring IC part of the calorimeter. The second columns of the tables *CC*  $\rightarrow$  *IC* contain the number of events in which  $P_t$  of a jet is shared between the CC and IC regions. The same sequence of restriction conditions takes place in the next columns. Thus, the *IC*, *EC* and *FC* columns include the number of events with jets entirely contained in these regions, while the *EC*  $\rightarrow$  *IC*, *FC* column gives the number of events where the jet covers both the EC and IC or EC and FC regions. From these tables we can see what number of events can be, in principle, most suitable for the precise jet energy absolute scale setting, carried out separately for the CC, EC and FC parts of the calorimeter in different  $P_t^\gamma$  intervals.

The selection cuts are as in (32) but  $P_{tCUT}^{clust} = 10 \text{ GeV}/c$

Less restrictive conditions, when up to 5% of the jet  $P_t$  are allowed to be shared between the CC, EC and FC parts of the calorimeter, is given in Table 6. Tables 5 and 6 correspond to the case of Selection 1<sup>32</sup>.

From last summarizing line of Table 5 we see that for the entire interval  $40 < P_t^\gamma < 140 \text{ GeV}/c$  PYTHIA predicts around 18000 events for CC and around 1000 events for EC at integrated luminosity  $L_{int} = 300 \text{ pb}^{-1}$ .

## 6. INFLUENCE OF THE $P_{tCUT}^{clust}$ PARAMETER ON THE PHOTON AND JET $P_t$ BALANCE AND ON THE INITIAL STATE RADIATION SUPPRESSION.

*The influence of  $P_{tCUT}^{clust}$  parameter (defining the upper limit on  $P_t$  of clusters or mini-jets in the event) on the variables characterizing the  $P_t^\gamma - P_t^{jet}$  balance is studied.*

In this section we shall study the specific sample of events considered in the previous section that may be most suitable for the jet energy calibration in the CC region, with jets entirely (100%) contained in this region, i.e. having 0% sharing of  $P_t^{jet}$ <sup>33</sup> with IC. Below we shall call them "CC-events". The  $P_t^\gamma$  spectrum for this particular set of events for  $P_{tCUT}^{clust} = 10 \text{ GeV}/c$  was presented in the first column (CC) of Table 5. Here we shall use three different jetfinders, LUCCELL from PYTHIA and UA1, UA2 from CMSJET [24]. The  $P_t^{clust}$  distributions for generated events found by the all three jetfinders in two  $P_t^\gamma$  intervals,  $40 < P_t^\gamma < 50 \text{ GeV}/c$  and  $70 < P_t^\gamma < 90 \text{ GeV}/c$ , are shown in Fig. 7 for  $P_{tCUT}^{clust} = 30 \text{ GeV}/c$  and  $\Delta\phi \leq 17^\circ$ .

It is interesting to note an evident similarity of the  $P_t^{clust}$  spectra with  $P_{t56}$  spectra shown in Fig. 6 (see also Figs. 8, 9), what support our intuitive picture of ISR and cluster connection described in Section 2.2.

Here we shall study in more detail correlation of  $P_t^{clust}$  with  $P_t^{ISR}$  mentioned above. The averaged value of intrinsic parton transverse momentum will be fixed at  $\langle k_t \rangle = 0.44 \text{ GeV}/c$ .

The banks of 1-jet " $\gamma + jet$ " events gained from the results of PYTHIA generation of  $5 \cdot 10^6$  signal " $\gamma + jet$ " events in each of four  $P_t^\gamma$  intervals (40–50, 50–70, 70–90, 90–140  $\text{GeV}/c$ )<sup>34</sup>

<sup>31</sup>at the particle level of simulation!

<sup>32</sup>The cost of passing to Selection 2 (defined in Section 3.2 with  $\epsilon^{jet} < 3\%$ ) is a reduction of the number of events by factor equal to 2.

<sup>33</sup>at the PYTHIA particle level of simulation

<sup>34</sup>they were discussed in Section 5

will be used here. The observables defined in Sections 3.1 and 3.2 will be restricted here by cuts of Selection 1 (16)–(23) and the cut parameters defined by (32).

We have chosen two of these intervals to illustrate the influence of the  $P_{tCUT}^{clust}$  parameter on the distributions of physical variables, that enter the balance equation (25). These distributions are shown in Fig. 8 ( $40 < P_t^\gamma < 50 \text{ GeV}/c$ ) and Fig. 9 ( $70 < P_t^\gamma < 90 \text{ GeV}/c$ ). In these figures, in addition to three variables  $P_{t56}$ ,  $P_t^{|\eta|>4.2}$ ,  $P_t^{out}$ , already explained in Sections 2.2, 3.1 and 3.2, we present distributions of two other variables,  $P_t(O+\eta > 4.2)$  and  $(1 - \cos\Delta\phi)$ , which define the right-hand side of the  $P_t^\gamma - P_t^{jet}$  balance equation (25). The distribution of the  $\gamma$ -jet back-to-back angle  $\Delta\phi$  (see (22)) is also presented in Figs. 8, 9.

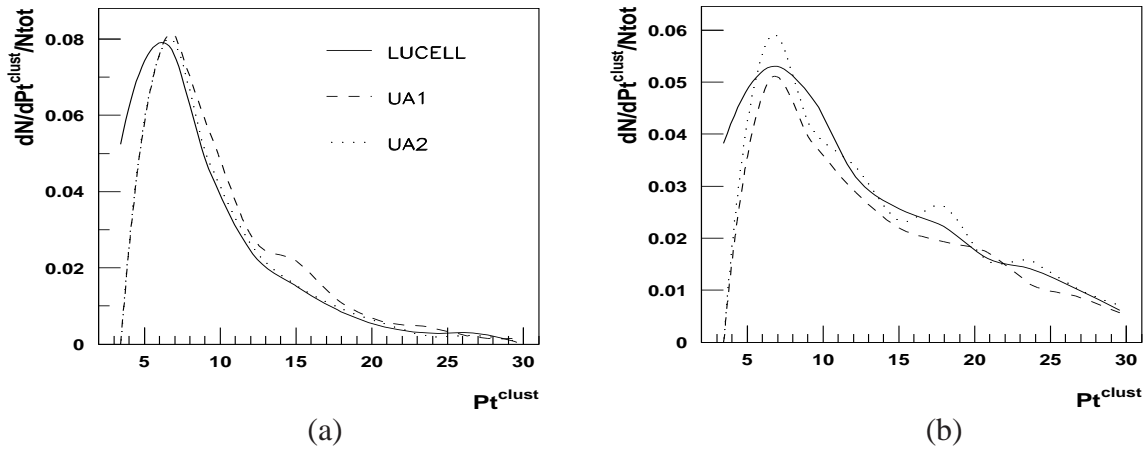


Fig. 7:  $P_t^{clust}$  distribution in “ $\gamma + jet$ ” events from two  $P_t^\gamma$  intervals: (a)  $40 < P_t^\gamma < 50 \text{ GeV}/c$  and (b)  $70 < P_t^\gamma < 90 \text{ GeV}/c$  with the same cut  $P_{tCUT}^{clust} = 30 \text{ GeV}/c$  ( $\Delta\phi \leq 17^\circ$ ).

The ISR describing variable  $P_{t56}$  (defined by (3)) and both components of (see (25)),  $(1 - \cos\Delta\phi)$  and  $P_t(O+\eta > 4.2)/P_t^\gamma$ , as well as  $P_t^{out}$  and  $\Delta\phi$ , show a tendency to become smaller (the mean values and the widths) with the restriction of the upper limit on the  $P_t^{clust}$  value (see Figs. 8, 9). It means that a jet energy calibration accuracy may increase with decreasing  $P_{tCUT}^{clust}$ , which justifies the intuitive choice of this new variable in Section 3. The origin of this improvement becomes clear from the  $P_{t56}$  density plot, which demonstrates a decrease of  $P_{t56}$  (or  $P_t^{ISR}$ ) values with decrease of  $P_t^{clust}$ . In Section 2.3 we gave arguments why it may also influence FSR.

Comparison of Fig. 8 (for  $40 < P_t^\gamma < 50 \text{ GeV}/c$ ) and Fig. 9 (for  $70 < P_t^\gamma < 90 \text{ GeV}/c$ ) also shows that the values of  $\Delta\phi$  as a degree of back-to-backness of the photon and jet  $P_t$  vectors in the  $\phi$ -plane decreases with increasing  $P_t^\gamma$ . At the same time  $P_t^{out}$  and  $P_t^{ISR}$  distributions become slightly wider. It is also seen that the  $P_t^{|\eta|>4.2}$  distribution practically does not depend on  $P_t^\gamma$  and  $P_t^{clust}$ <sup>35</sup>.

It should be mentioned that the results presented in Figs. 8 and 9 were obtained with the LUCCELL jetfinder of PYTHIA<sup>36</sup>.

<sup>35</sup>see also Appendix 2 and Fig. 2

<sup>36</sup>The results obtained with all jetfinders and  $P_t^\gamma - P_t^{jet}$  balance will be discussed in Section 7 in more detail.

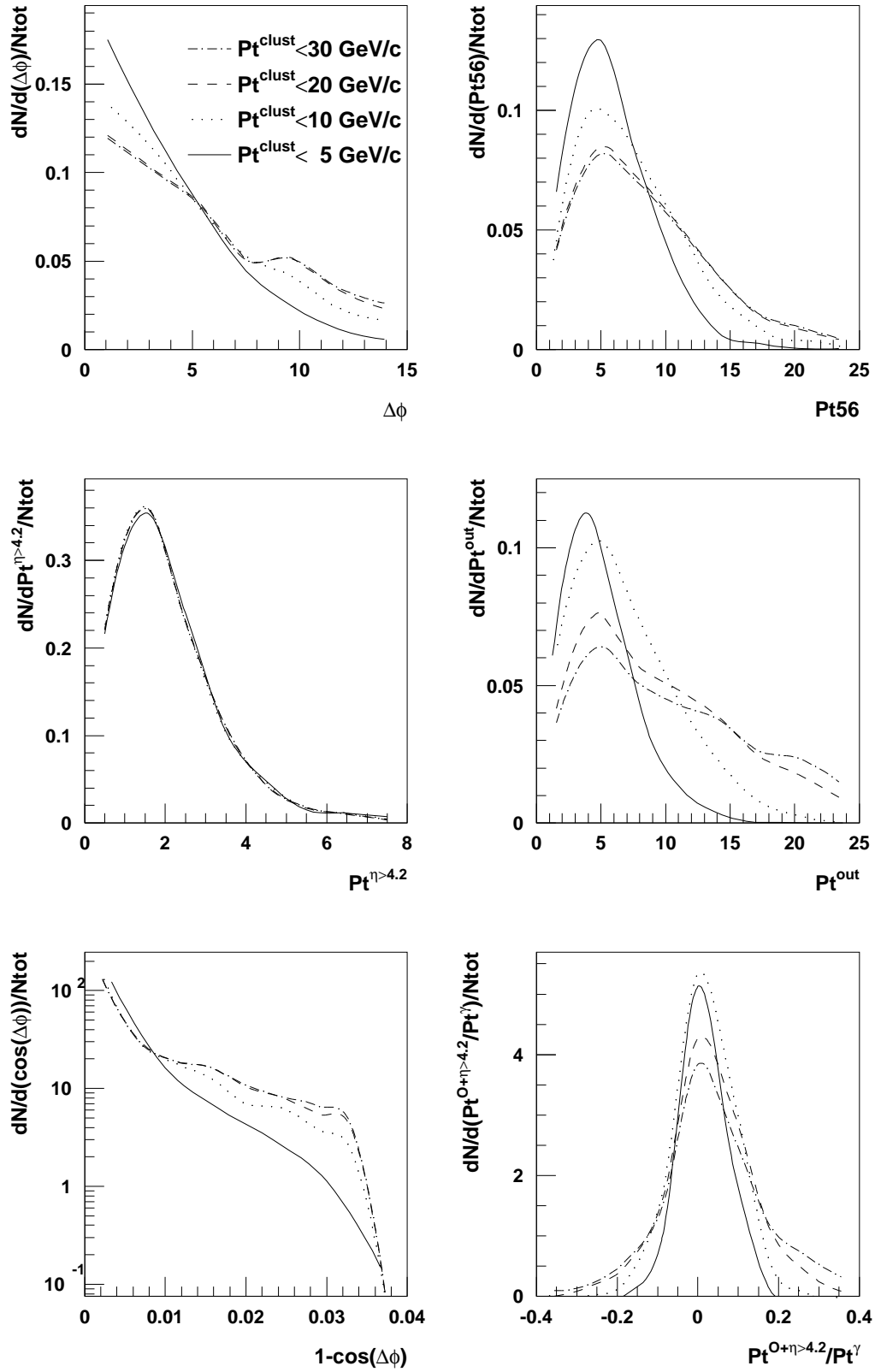


Fig. 8: LUCCELL algorithm,  $\Delta\phi < 17^\circ$ ;  $40 < P_t^\gamma < 50 \text{ GeV}/c$ . Selection 1.

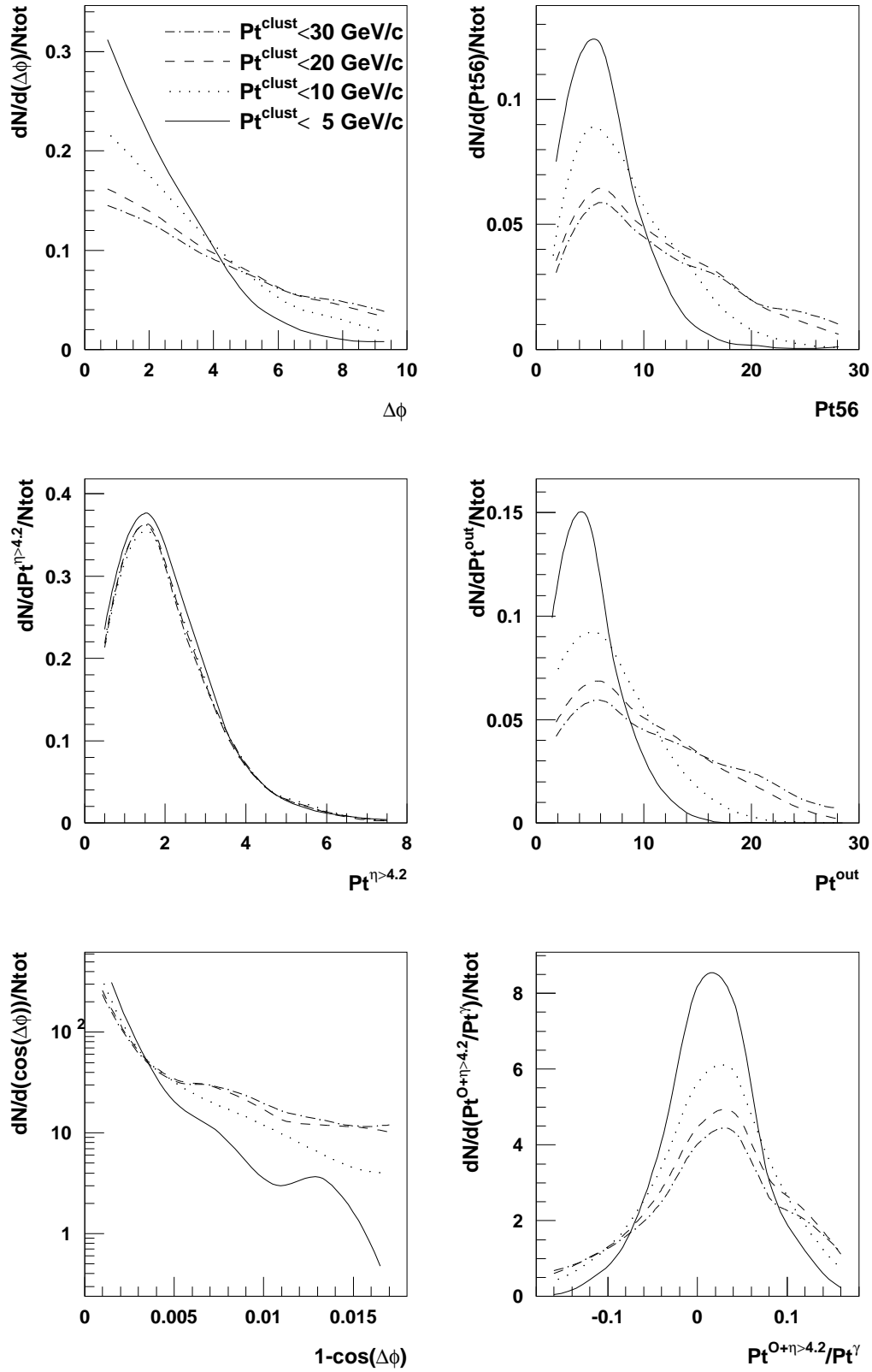


Fig. 9: LUCCELL algorithm,  $\Delta\phi < 17^\circ$ ;  $70 < P_t^\gamma < 90 \text{ GeV}/c$ . Selection 1.

## 7. DEPENDENCE OF THE $P_t$ -DISBALANCE IN THE “ $\gamma + jet$ ” SYSTEM ON $P_{tCUT}^{clust}$ and $P_{tCUT}^{out}$ PARAMETERS.

It is shown that with Selection 2 (that leads to about twice reduction of the number of events  $N_{event}$  for  $P_t^\gamma < 70 \text{ GeV}/c$  and to about 30 – 40% loss of them at  $P_t^\gamma > 70 \text{ GeV}/c$ ) one can select at the particle level the events with a value of the fractional  $(P_t^\gamma - P_t^{Jet})/P_t^\gamma$  disbalance better than 1%. The number of events (at  $L_{int} = 300 \text{ pb}^{-1}$ ) and other characteristics of “ $\gamma + jet$ ” events are presented in tables of Appendix 2 for interval  $40 < P_t^\gamma < 140 \text{ GeV}/c$ .

Earlier we have introduced physical variables for studying “ $\gamma + jet$ ” events (Section 3) and discussed what cuts for them may lead to a decrease in the disbalance of  $P_t^\gamma$  and  $P_t^{Jet}$ . One can make these cuts to be tighter if more events would be collected during data taking.

Here we shall study in detail the dependence of the  $P_t$  disbalance in the “ $\gamma + jet$ ” system on  $P_{tCUT}^{clust}$  and  $P_{tCUT}^{out}$  values. For this aim we shall use the same samples of events as in Section 5 that were generated by using PYTHIA with 2 QCD subprocesses (1a) and (1b) and collected to cover three  $P_t^\gamma$  intervals: 40–50, 70–90, 90–140  $\text{GeV}/c$ .

The normalized event distributions over  $(P_t^\gamma - P_t^{Jet})/P_t^\gamma$  for two most illustrative  $P_t^\gamma$  intervals  $40 < P_t^\gamma < 50$  and  $70 < P_t^\gamma < 90 \text{ GeV}/c$  are shown for a case of  $\Delta\phi \leq 17^\circ$  in Fig. 10 in different plots for three jetfinders LUCCELL, UA1 and UA2. These plots demonstrate the dependence of the mean and mean square deviations on  $P_{tCUT}^{clust}$  value.

More details on  $P_{tCUT}^{clust}$  dependence of different important features of “ $\gamma + jet$ ” events are presented in tables of Appendix 2. They include the information about a topology of events and mean values of most important variables that characterize  $P_t^\gamma - P_t^{Jet}$  disbalance.

This information can be useful as a model guideline while performing jet energy calibration procedure and also may serve for fine tuning of PYTHIA parameters while comparing its predictions with the collected real data.

Appendix 2 contains the tables for events with  $P_t^\gamma$  varying within three intervals:  $40 < P_t^\gamma < 50$ ,  $70 < P_t^\gamma < 90$  and  $90 < P_t^\gamma < 140 \text{ GeV}/c$ .  $\Delta\phi$  is limited there by  $\Delta\phi < 17^\circ$ . Tables 1–3 correspond to the events passed Selection 1 with a jet found by UA1 algorithm. Tables 4–6 correspond to the events passed Selection 2. The latter allows to select events with the “isolated jet”, i.e. events with the total  $P_t$  activity in the  $\Delta R = 0.3$  ring around the jet not exceeding 3% of jet  $P_t$  (see Section 3.2)<sup>37</sup>.

The columns in all tables correspond to five different values of cut parameter  $P_{tCUT}^{clust} = 30, 20, 15, 10$  and  $5 \text{ GeV}/c$ . The upper lines contain the expected numbers  $N_{event}$  of “CC events” (i.e. the number of signal “ $\gamma + jet$ ” events in which the jet is entirely fitted into the CC region of the calorimeter; see Section 5) for the integrated luminosity  $L_{int} = 300 \text{ pb}^{-1}$ .

In the next four lines of the tables we put the values of  $P_t56$ ,  $\Delta\phi$ ,  $P_t^{out}$  and  $P_t^{|\eta|>4.2}$  defined by formulae (3), (22), (24) and (5) respectively and averaged over the events selected with a chosen  $P_{tCUT}^{clust}$  value.

From the tables we see that the values of  $P_t56$ ,  $\Delta\phi$ ,  $P_t^{out}$  decrease fast with decreasing  $P_{tCUT}^{clust}$ , while the averaged values of  $P_t^{|\eta|>4.2}$  show very weak dependence on it (practically constant).

The following three lines present the average values of the variables  $(P_t^\gamma - P_t^{part})/P_t^\gamma$ ,  $(P_t^J - P_t^{part})/P_t^J$ ,  $(P_t^\gamma - P_t^J)/P_t^\gamma$  (here  $J \equiv \text{Jet}$ ) that serve as measures of the  $P_t$  disbalance in

<sup>37</sup>In contrast to the case of LHC energies, where we required in Selection 2  $\epsilon^{jet} \leq 6 - 8\%$  for  $40 < P_t^\gamma < 50$  (see [25]), at Tevatron energies, due to less  $P_t$  activity in the space beyond the jet, one can impose the tighter cut  $\epsilon^{jet} \leq 3\%$ .

the “ $\gamma + parton$ ” and “ $\gamma + jet$ ” systems as well as a measure of the parton-to-hadrons (Jet) fragmentation effect.

The lines 9, 10 include the averaged values of  $P_t(O+\eta > 4.2)/P_t^\gamma$  and  $(1 - \cos(\Delta\phi))$  quantities that appear on the right-hand side of  $P_t^\gamma - P_t^{jet}$  balance equation (25).

After application of cut  $\Delta\phi < 17^\circ$  the value of  $\langle 1 - \cos(\Delta\phi) \rangle$  becomes smaller than the value of  $\langle P_t(O+\eta > 4.2)/P_t^\gamma \rangle$  in the case of Selection 1 and tends to decrease faster with growing energy. So, we can again conclude that the main contribution into the  $P_t$  disbalance in the “ $\gamma + jet$ ” system, as defined by equation (25), comes from the term  $P_t(O+\eta > 4.2)/P_t^\gamma$ . With Selection 2 the contribution of  $\langle P_t(O+\eta > 4.2)/P_t^\gamma \rangle$  reduces with growing  $P_t^{clust}$  to the level of  $\langle 1 - \cos(\Delta\phi) \rangle$  and even to smaller values.

We have estimated separately the contributions of two terms  $\mathbf{P}_t^O \cdot \mathbf{n}^{Jet}$  and  $\mathbf{P}_t^{|\eta|>4.2} \cdot \mathbf{n}^{Jet}$  that enter  $P_t(O+\eta > 4.2)$  (see (25)).

Firstly from tables it is easily seen that  $P_t^{|\eta|>4.2}$  has practically the same value in all  $P_t^\gamma$  intervals and it does not depend neither on  $\Delta\phi$  nor on  $P_t^{clust}$  values being equal to  $2 \text{ GeV}/c$  up to a good precision <sup>38</sup>.

A mean value of  $|\mathbf{P}_t^{|\eta|>4.2} \cdot \mathbf{n}^{Jet}|$  contribution does not exceed  $\approx 0.15 \text{ GeV}/c$  and a width (RMS) of the corresponding distribution contributes only 11 – 12% to the total width of the  $P_t(O+\eta > 4.2)$  distribution. So, a mean and a width of  $P_t(O+\eta > 4.2)$  are caused mainly by measurable term  $\mathbf{P}_t^O \cdot \mathbf{n}^{Jet}$  <sup>39</sup>. Below in this section the cuts on the value of  $P_t^{out}$  is applied to select events with better  $P_t^\gamma$  and  $P_t^{jet}$  balance.

The following two lines contain the averaged values of the standard deviations  $\sigma(Db[\gamma, J])$  and  $\sigma(Db[\gamma, part])$  of  $(P_t^\gamma - P_t^J)/P_t^\gamma (\equiv Db[\gamma, J])$  and  $(P_t^\gamma - P_t^{part})/P_t^\gamma (\equiv Db[\gamma, part])$  respectively. These two variables drop approximately by about 50% (and even more for  $P_t^\gamma > 70 \text{ GeV}/c$ ) with restricting from  $P_{tCUT}^{clust} = 30 \text{ GeV}/c$  to  $5 \text{ GeV}/c$  for all  $P_t^\gamma$  intervals.

The last lines of the tables present the number of generated events left after cuts.

Two features are clearly seen from these tables <sup>40</sup>:

- (1) in events with  $\Delta\phi < 17^\circ$  the fractional disbalance on the *parton-photon* level  $(P_t^\gamma - P_t^{part})/P_t^\gamma$  reduces to about 1% (or even less) after imposing  $P_t^{clust} < 10 \text{ GeV}/c$ . It means that  $P_{tCUT}^{clust} = 10 \text{ GeV}/c$  is really effective for ISR suppression as it was supposed in Section 3.1.
- (2) *parton-to-jet* hadronization/fragmentation effect, that includes also FSR, can be estimated by the value of the following ratio  $(P_t^J - P_t^{part})/P_t^J$ . It always has a negative value. It means that a jet loses some part of the parent parton transverse momentum  $P_t^{part}$ . It is seen that in the case of Selection 1 this effect gives a big contribution into  $P_t^\gamma$  and  $P_t^{jet}$  disbalance even after application of  $P_{tCUT}^{clust} = 10 \text{ GeV}/c$ . The value of the fractional  $(P_t^J - P_t^{part})/P_t^J$  disbalance does not vary strongly with  $P_{tCUT}^{clust}$  in the cases of Selections 2 and 3.

We also see from the tables that more restrictive cuts on the observable  $P_t^{clust}$  lead to a decrease in the values of  $P_{t56}$  variable (non-observable one) that serves, according to (3), as a measure of the initial state radiation transverse momentum  $P_t^{ISR}$ , i.e. of the main source of the  $P_t$  disbalance in the fundamental  $2 \rightarrow 2$  subprocesses (1a) and (1b). Thus, variation of  $P_{tCUT}^{clust}$  from  $30 \text{ GeV}/c$  to  $5 \text{ GeV}/c$  (for  $\Delta\phi < 17^\circ$ ) leads to suppression of the  $P_{t56}$  value (or  $P_t^{ISR}$ ) approximately by 40% for  $40 < P_t^\gamma < 50 \text{ GeV}/c$  and by  $\approx 60\%$  for  $P_t^\gamma \geq 90 \text{ GeV}/c$ .

<sup>38</sup>Let us emphasize that it is a prediction of PYTHIA.

<sup>39</sup>A contribution of  $\mathbf{P}_t^O(\nu)$  and  $\mathbf{P}_t^O(\mu, |\eta^\mu| > 2.5)$  (see (14)) in the selected event samples is a negligibly small.

<sup>40</sup>As was shown in [19, 15] a transition from  $\Delta\phi \leq 180^\circ$  to  $\Delta\phi \leq 17^\circ$  supposed to be most effective in low  $P_t^\gamma$  intervals, does not affect the  $(P_t^\gamma - P_t^{jet})/P_t^\gamma$  disbalance strongly as compared with “jet isolation” criterion or cut on  $P_t^{clust}$  and  $P_t^{out}$



In the first two intervals with  $P_t^\gamma < 90 \text{ GeV}/c$  the decrease in  $P_{tCUT}^{clust}$  leads to some decrease in the  $(P_t^\gamma - P_t^J)/P_t^\gamma$  ratio (see Tables 1,2 of Appendix 2 and Fig. 10). In the case of  $90 < P_t^\gamma < 140 \text{ GeV}/c$  the mean value of  $(P_t^\gamma - P_t^J)/P_t^\gamma$  drops from 4.2% to 1.1% (see Table 3 of Appendix 2). After we pass to Selection 2 (Table 4–6 of Appendix 2) this disbalance becomes of the 1% level and smaller but at the cost of statistics loss (by about 40 – 60%). Tables 4–6 clearly show the prediction of PYTHIA about the best level of jet calibration precision that can be achieved after application of Selection 2.

*Thus, to summarize the results presented in tables of Appendix 2, we want to underline that only after imposing the jet isolation requirement (see Tables 4–6 of Appendix 2) the mean values of  $P_t^\gamma$  and  $P_t^{Jet}$  disbalance, i.e.  $(P_t^\gamma - P_t^J)/P_t^\gamma$ , for all  $P_t^\gamma$  intervals are contained inside the 1% window for any  $P_t^{clust} \leq 20 \text{ GeV}/c$ . The reduction of  $P_t^{clust}$  leads to lower values of mean square deviations of the photon-parton  $Db[\gamma, part]$  and of photon-jet  $Db[\gamma, J]$  balances.*

The Selection 2 (with  $P_{tCUT}^{clust} = 10 \text{ GeV}/c$ , for instance) leaves after its application the following number of events with jets *entirely contained* (see Section 5) in the CC region at  $L_{int} = 300 \text{ pb}^{-1}$ :

- (1) about 4000 for  $40 < P_t^\gamma < 50 \text{ GeV}/c$ ,
- (2) about 3000 for  $50 < P_t^\gamma < 70 \text{ GeV}/c$ ,
- (3) about 850 for  $70 < P_t^\gamma < 90 \text{ GeV}/c$  and (4) about 500 for the  $90 < P_t^\gamma < 140 \text{ GeV}/c$ .

So, we can say that Selections 2, besides improving the  $P_t^\gamma - P_t^{Jet}$  balance value, is also important for selecting events with a clean jet topology and for rising the confidence level of a jet determination.

Up to now we have been studying the influence of the  $P_{tCUT}^{clust}$  parameter on the balance. Let us see, in analogy with Fig. 10, what effect is produced by  $P_{tCUT}^{out}$  variation <sup>41</sup>.

If we  $P_{tCUT}^{out} = 5 \text{ GeV}/c$ , keeping  $P_t^{clust}$  practically unbound by  $P_{tCUT}^{clust} = 30 \text{ GeV}/c$ , then, as can be seen from Fig. 11, the mean and RMS values of the  $(P_t^\gamma - P_t^J)/P_t^\gamma$  in the case of the LUCCELL algorithm for  $40 < P_t^\gamma < 50 \text{ GeV}/c$  decrease from 3.6% to 1.3% and from 14.5% to 7.1%, respectively. For  $70 < P_t^\gamma < 90 \text{ GeV}/c$  the mean and RMS values drop from 4.5% to 0.7% and from 11.5% to 3.7% respectively. From these plots we also may conclude that variation of  $P_{tCUT}^{out}$  improves the  $P_t$ -disbalance, in fact, almost in the same way as the variation of  $P_{tCUT}^{clust}$ . It is not surprising as the cluster  $P_t$  activity is a part of the  $P_t^{out}$  activity.

The influence of the  $P_{tCUT}^{out}$  variation on the distribution of  $(P_t^\gamma - P_t^J)/P_t^\gamma$  is shown in Fig. 12 for Selection 1 with the fixed value  $P_{tCUT}^{clust} = 10 \text{ GeV}/c$ . In this case the mean value of  $(P_t^\gamma - P_t^J)/P_t^\gamma$  drops from 3.2% to 1.3% for LUCCELL and from 2.7% to 1.3% for UA2 algorithms for the  $40 < P_t^\gamma < 50 \text{ GeV}/c$  interval. At the same time RMS value changes from 12% to 7% for all algorithms. For interval  $70 < P_t^\gamma < 90 \text{ GeV}/c$  the mean value of fractional disbalance  $(P_t^\gamma - P_t^J)/P_t^\gamma$  decrease to to 1.2 – 1.4% at  $P_{tCUT}^{out} = 10 \text{ GeV}/c$  and to less then 1% at  $P_{tCUT}^{out} = 5 \text{ GeV}/c$ . Simultaneously, RMS decreases to about 3.7% for all three jetfinders.

More detailed study of  $P_{tCUT}^{out}$  influence on the  $(P_t^\gamma - P_t^{Jet})/P_t^\gamma$  disbalance will be continued in the following Section 8 (see also Appendix 3).

*So, we conclude basing on the analysis of PYTHIA simulation (as a model) that the new cuts  $P_{tCUT}^{clust}$  and  $P_{tCUT}^{out}$  introduced in Section 3 as well as introduction of a new object, the “isolated jet”, are found as those that may be very efficient tools to improve the jet calibration accuracy. Their combined usage for this aim and for the background suppression will be a subject of a further more detailed study in Section 8.*

<sup>41</sup>This variable enters into the expression  $P_t(O + \eta > 4.2)/P_t^\gamma$ , which makes a dominant contribution to the right-hand side of  $P_t$  balance equation (??), as we mentioned above.

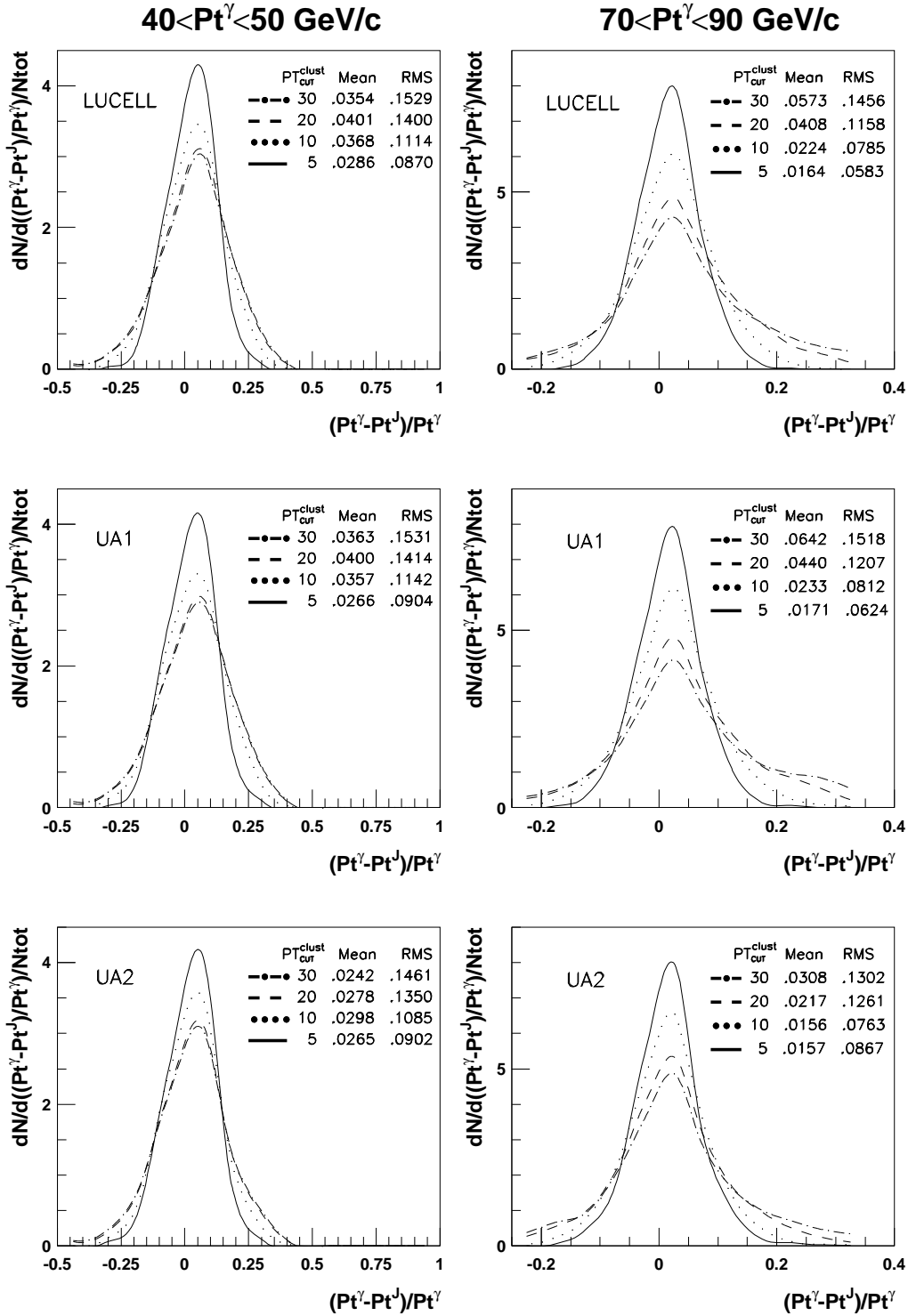


Fig. 10: A dependence of  $(P_t^\gamma - P_t^J)/P_t^\gamma$  on  $P_t^{clust}$  for LUCCELL, UA1 and UA2 jetfinding algorithms and two intervals of  $P_t^\gamma$ . The mean and RMS of the distributions are displayed on the plots.  $\Delta\phi < 17^\circ$ .  $P_t^{out}$  is not limited. Selection 1.

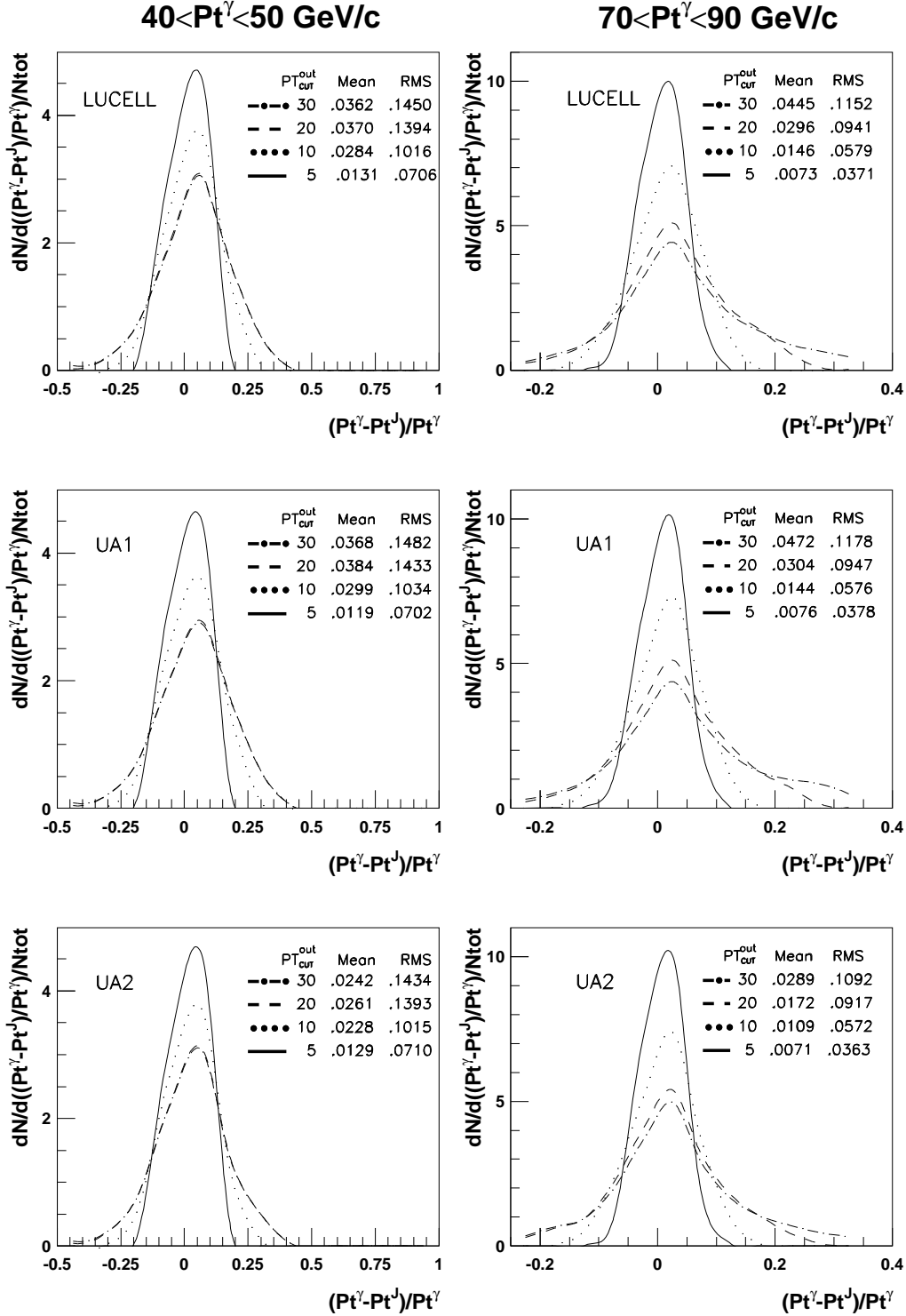


Fig. 11: A dependence of  $(P_t^\gamma - P_t^J)/P_t^\gamma$  on  $P_{tCUT}^{out}$  for LUCCELL, UA1 and UA2 jetfinding algorithms and two intervals of  $P_t^\gamma$ . The mean and RMS of the distributions are displayed on the plots.  $\Delta\phi \leq 17^\circ$ ,  $P_{tCUT}^{clust} = 30 \text{ GeV}/c$ . Selection 1.

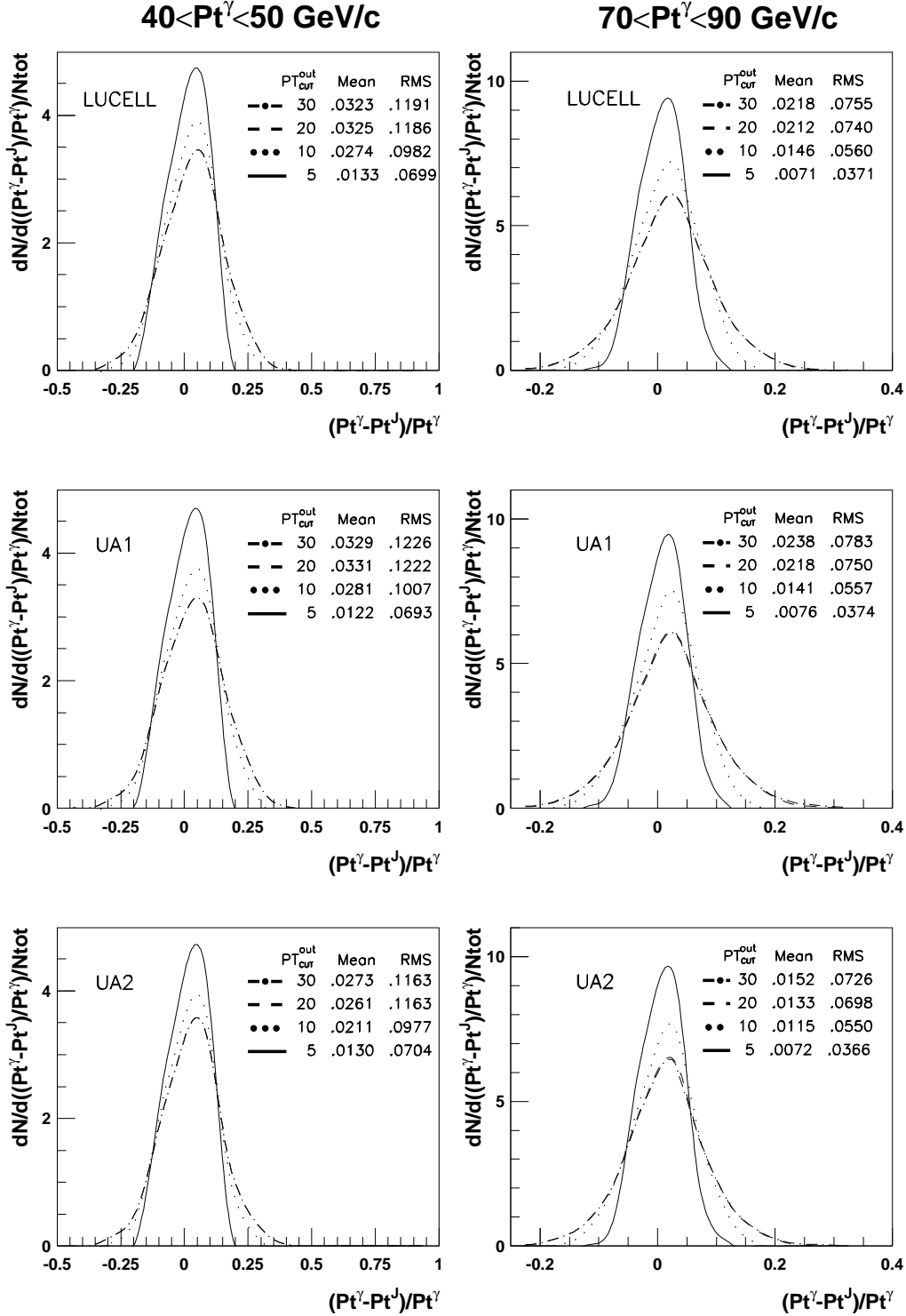


Fig. 12: A dependence of  $(P_t^\gamma - P_t^J)/P_t^\gamma$  on  $P_t^{out}_{CUT}$  for LUCCELL, UA1 and UA2 jetfinding algorithms and two intervals of  $P_t^\gamma$ . The mean and RMS of the distributions are displayed on the plots.  $\Delta\phi \leq 17^\circ$ ,  $P_t^{clust}_{CUT} = 10 \text{ GeV}/c$ . Selection 1.

## 8. ESTIMATION OF BACKGROUND SUPPRESSION CUTS EFFICIENCY.

The relative efficiency of “hadronic” cuts that are added to “photonic” ones, used to suppress the background in the case of inclusive photon measurement, is estimated at the particle level. It is shown that an imposing of new cuts on  $P_t$  of “clusters” ( $P_{tCUT}^{clust}$ ) and on  $P_t$  activity in the region out of “ $\gamma + jet$ ” system ( $P_{tCUT}^{out}$ ) and also an application of “jet isolation” criterion would allow to achieve further (after “photonic” cuts) fourteen-fold background suppression at the cost of four-fold loss of the signal “ $\gamma^{dir} + jet$ ” events.

It is also shown that the imposing of  $P_{tCUT}^{out}$ ,  $P_{tCUT}^{clust}$  together with a usage of jet isolation criterion would lead to a substantial improvement of  $P_t^\gamma - P_t^{jet}$  balance.

The potentially dangerous role of a new source of background to the signal “ $\gamma^{dir} + jet$ ” events caused by hard bremsstrahlung photons (“ $\gamma - brem$ ”) is demonstrated. It is shown that at Tevatron energy this new irreducible background may be compatible at low  $P_t^\gamma$  intervals with the  $\pi^0$  contribution and it may grow faster with  $P_t^\gamma$  increasing than the latter one.

To estimate an efficiency of the selection criteria proposed in Section 3.2 we carried out the simulation<sup>42</sup> with a mixture of all QCD and SM subprocesses with large cross sections existing in PYTHIA<sup>43</sup>. The events caused by this set of the subprocesses may give a large background to the “ $\gamma^{dir} + jet$ ” signal events defined by the subprocesses (1a) and (1b)<sup>44</sup> that were also included in this simulation.

Three generations with the above-mentioned set of subprocesses were performed. Each of them was done with a different value of  $\hat{p}_\perp^{min}$  parameter<sup>45</sup> that defines a minimal value of  $P_t$  appearing in the final state of a hard  $2 \rightarrow 2$  parton level fundamental subprocess in the case of ISR absence. These values were  $\hat{p}_\perp^{min} = 40, 70$  and  $100 \text{ GeV}/c$ . By 40 million events were generated for each of  $\hat{p}_\perp^{min}$  value. The cross sections of the above-mentioned subprocesses define the rates of corresponding physical events and thus appear in simulation as weight factors.

We selected “ $\gamma^{dir}$ -candidate +1 jet” events containing one  $\gamma^{dir}$ -candidate (denoted in what follows as  $\tilde{\gamma}$ ) and one jet, found by LUCCELL, with  $P_t^{jet} > 30 \text{ GeV}/c$ . Here and below, as we work at the PYTHIA particle level of simulation, speaking about the  $\gamma^{dir}$ -candidate we actually mean, apart from  $\gamma^{dir}$ , a set of particles like electrons, bremsstrahlung photons and also photons from neutral meson decays that may be registered in one D0 calorimeter tower of the  $\Delta\eta \times \Delta\phi = 0.1 \times 0.1$  size.

Here we consider a set of 17 cuts that are separated into 2 subsets: 6 “photonic” cuts and 11 “hadronic” ones. The first subset consists of the cuts used to select an isolated photon candidate in some  $P_t^{\tilde{\gamma}}$  interval. The second one includes the cuts connected mostly with jets and clusters and are used to select events having one “isolated jet” and limited  $P_t$  activity out of “ $\tilde{\gamma} + jet$ ” system.

The used cuts are listed in Table 7. To give an idea about their physical meaning and importance we have done an estimation of their possible influence on the signal-to-background ratios  $S/B$ . The letter were calculated after application of each cut. Their values are presented in Table 8 for a case of the most illustrative intermediate interval of event generation with  $\hat{p}_\perp^{min} = 70 \text{ GeV}/c$ . In this table the number in each line corresponds to the number of the cut in Table 7. Three important lines of Table 8 are darkened because they will be often referenced to while

<sup>42</sup>PYTHIA 5.7 version with default CTEQ2L parameterization of structure functions is used here.

<sup>43</sup>ISUB=1, 2, 11–20, 28–31, 53, 68 (in notations of PYTHIA)

<sup>44</sup>ISUB=29 and 14 in PYTHIA. A contribution of another possible NLO channel  $gg \rightarrow g\gamma$  (ISUB=115) was found to be still negligible even at Tevatron energies.

<sup>45</sup>CKIN(3) in PYTHIA

discussing the following Tables 9–11.

The efficiencies  $E f f_{S(B)}$  (with their errors) in Table 8 are defined as a ratio of the number of signal (background) events that passed under a cut (1–17) to the number of the preselected events (1st cut of this table).

Table 7: List of the applied cuts (will be used also in Tables 8–11).

1. a) $P_t^{\tilde{\gamma}} \geq 40 \text{ GeV}/c$ , b) $P_t^{jet} \geq 30 \text{ GeV}/c$ ,	9. $\Delta\phi < 17^\circ$ ;
c) $ \eta^{\tilde{\gamma}}  \leq 2.5$ , d) $P_t^{hadr} < 7 \text{ GeV}/c^*$ ;	10. $P_t^{miss}/P_t^{\tilde{\gamma}} \leq 0.10$ ;
2. $P_t^{isol} \leq 5 \text{ GeV}/c$ , $\epsilon^{\tilde{\gamma}} < 15\%$ ;	11. $P_t^{clust} < 20 \text{ GeV}/c$ ;
3. $P_t^{\tilde{\gamma}} \geq \hat{p}_\perp^{min}$ ;	12. $P_t^{clust} < 15 \text{ GeV}/c$ ;
4. $P_{t_{ring}}^{isol} \leq 1 \text{ GeV}/c^{**}$ ;	13. $P_t^{clust} < 10 \text{ GeV}/c$ ;
5. $P_t^{isol} \leq 2 \text{ GeV}/c$ , $\epsilon^{\tilde{\gamma}} < 5\%$ ;	14. $P_t^{out} < 20 \text{ GeV}/c$ ;
6. $N_{jet} \leq 3$ ;	15. $P_t^{out} < 15 \text{ GeV}/c$ ;
7. $N_{jet} \leq 2$ ;	16. $P_t^{out} < 10 \text{ GeV}/c$ ;
8. $N_{jet} = 1$ ;	17. $\epsilon^{jet} \leq 3\%$ .

\* maximal  $P_t$  of a hadron in the ECAL cell containing a  $\gamma^{dir}$ -candidate;

\*\* A scalar sum of  $P_t$  in the ring:  $P_t^{sum}(R = 0.4) - P_t^{sum}(R = 0.2)$ .

Line number 1 of Table 7 makes primary preselection. It includes and specifies our first general cut (16) of Section 3.2 as well as the cut connected with ECAL geometry and the cut (19) that excludes  $\gamma^{dir}$ -candidates accompanied by hadrons.

Line number 2 of Table 7 fixes the values of  $P_{t_{CUT}}^{isol}$  and  $\epsilon_{CUT}^{\tilde{\gamma}}$  that, according to (17) and (18), define the isolation parameters of  $\tilde{\gamma}$ .

The third cut selects the events containing  $\gamma^{dir}$ -candidates with  $P_t$  higher than  $\hat{p}_\perp^{min}$  ( $\equiv CKIN(3)$ ) threshold<sup>46</sup>. We impose the third cut to select the samples of events with  $P_t^{\tilde{\gamma}} \geq 40, 70$  and  $100 \text{ GeV}/c$  as ISR may smear the sharp kinematical cutoff defined by  $CKIN(3)$  [9]. This cut reflects an experimental viewpoint when one is interested in how many events with  $\gamma^{dir}$ -candidates are contained in some definite interval of  $P_t^{\tilde{\gamma}}$ .

The fourth cut restricts a value of  $P_{t_{ring}}^{isol} = P_{t_{R=0.4}}^{isol} - P_{t_{R=0.2}}^{isol}$ , where  $P_{t_R}^{isol}$  is a sum of  $P_t$  of all ECAL cells contained in the cone of the radius  $R$  around the cell fired by  $\gamma^{dir}$ -candidate [34], [35].

The fifth cut makes tighter the isolation criteria within  $R = 0.7$  than those imposed onto  $\gamma^{dir}$ -candidate in the second line of Table 7.

The cuts considered up to now, apart from general preselection cut  $P_t^{jet} \geq 30 \text{ GeV}/c$  used in the first line of Table 7, were connected with photon selection (“photonic” cuts). Before we go further, some words of caution must be said here. Firstly, we want to emphasize that the starting numbers of the signal ( $S$ ) and background ( $B$ ) events (first line of Table 8) may be specific only for PYTHIA generator and for the way of preparing primary samples of the signal and background events described above. So, we want to underline here that the starting values of  $S$  and  $B$  in the first columns of Table 8 are model dependent.

But nevertheless, for our aim of investigation of efficiency of new cuts 11–17 (see [10]–[17]) the important thing here is that we can use these starting model numbers of  $S$ - and  $B$ -events for studying a further relative influence of these cuts on  $S/B$  ratio.

The cuts 6–9 are connected with the selection of events having only one jet and the definition of jet-photon spatial orientation in  $\phi$ -plane. The 9-th cut selects the events with jet and photon

<sup>46</sup>see PYTHIA manual [9]

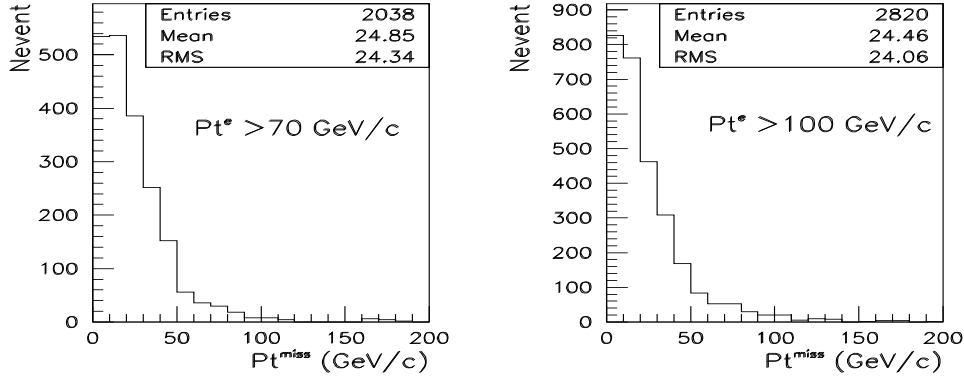


Fig. 13: Distribution of events over  $P_t^{miss}$  in events with energetic  $e^\pm$ 's appearing as direct photon candidates for the cases  $P_t^e \geq 70 \text{ GeV}/c$  and  $P_t^e \geq 100 \text{ GeV}/c$  (here are used events satisfying cuts 1–5 of Table 7).

transverse momenta being “back-to-back” to each other in  $\phi$ -plane within the angle interval of the  $\Delta\phi = 17^\circ$  size<sup>47</sup>.

In line 10 we used the cut on  $P_t^{miss}$  to reduce a background contribution from the electroweak subprocesses  $qg \rightarrow q' + W^\pm$  and  $q\bar{q}' \rightarrow g + W^\pm$  with the subsequent decay  $W^\pm \rightarrow e^\pm\nu$  that leads to a substantial  $P_t^{miss}$  value. It is clear from the distributions over  $P_t^{miss}$  for two  $P_t^e$  intervals presented in Fig. 13 (compare with Fig. 5). One can see from the last column of Table 8 “ $e^\pm$ ” that the cut on  $P_t^{miss}$  reduces strongly (in about 4 times) the number of events containing  $e^\pm$  as direct photon candidate.

Table 8: Values of significance and efficiencies for  $\hat{p}_\perp^{min} = 70 \text{ GeV}/c$ .

Cut	$S$	$B$	$Eff_S(\%)$	$Eff_B(\%)$	$S/B$	$e^\pm$
1	39340	1247005	100.00± 0.00	100.000± 0.000	0.03	17562
2	36611	51473	93.06± 0.68	4.128± 0.019	0.71	4402
3	29903	18170	76.01± 0.58	1.457± 0.011	1.65	2038
4	26426	11458	67.17± 0.53	0.919± 0.009	2.31	1736
5	23830	7504	60.57± 0.50	0.602± 0.007	3.18	1568
6	23788	7406	60.47± 0.50	0.594± 0.007	3.21	1554
7	23334	6780	59.31± 0.49	0.544± 0.007	3.44	1460
8	19386	4136	49.28± 0.43	0.332± 0.005	4.69	1142
9	18290	3506	46.49± 0.42	0.281± 0.005	5.22	796
10	18022	3418	45.81± 0.41	0.274± 0.005	5.27	210
11	15812	2600	40.19± 0.38	0.208± 0.004	6.08	176
12	13702	1998	34.83± 0.35	0.160± 0.004	6.86	130
13	10724	1328	27.26± 0.30	0.106± 0.003	8.08	88
14	10636	1302	27.04± 0.30	0.104± 0.003	8.17	86
15	10240	1230	26.03± 0.29	0.099± 0.003	8.33	84
16	8608	984	21.88± 0.26	0.079± 0.003	8.75	64
17	6266	622	15.93± 0.22	0.050± 0.002	10.07	52

(\*) The background ( $B$ ) does not include the contribution from the “ $e^\pm$  events” (i.e. in which  $e^\pm$  fake  $\gamma$ -candidate) that is shown separately in the right-hand column “ $e^\pm$ ”.

Moving further we see from Table 8 that the cuts 11–16 of Table 7 reduce the values of  $P_t^{clust}$  and  $P_t^{out}$  down to the values less than  $10 \text{ GeV}/c$ . The 17-th cut of Table 7 imposes

<sup>47</sup>i.e. within the size of three calorimeter cells

the jet isolation requirement. It leaves only the events with jets having the sum of  $P_t$  in a ring surrounding a jet to be less than 3% of  $P_t^{Jet}$ . From comparison of the numbers in 10-th and 17-th lines we make the important conclusion that all these new cuts (11–17), despite of model dependent nature of starting  $S/B$  value in line 10, may, in principle, lead to the following about two-fold improvement of  $S/B$  ratio. This improvement is reached by reducing the  $P_t$  activity out of “ $\tilde{\gamma} + 1 jet$ ” system.

It is also rather interesting to mention that *the total effect of “hadronic cuts” 6–17 for the case of  $\hat{p}_\perp^{min} = 70 GeV/c$  consists of about twelve-fold decrease of background contribution at the cost of less than four-fold loss of signal events (what results in about 3.2 times growth of  $S/B$  ratio)*. So, in this sense, we may conclude that from the viewpoint of  $S/B$  ratio a study of “ $\gamma + jet$ ” events may be more preferable as compared with a case of inclusive photon production.

Table 9 includes the numbers of signal and background events left in three generated event samples after application of cuts 1–16 and 1–17. They are given for all three intervals of  $P_t^{\tilde{\gamma}}$ . Tables 9 and 8 are complementary to each other. The summary of Table 8 is presented in the middle section ( $\hat{p}_\perp^{min} = 70 GeV/c$ ) of Table 9 where the line “Preselected” corresponds to the cut 1 of Table 7 and, respectively, to the line number 1 of Table 8 presented above. The line “After cuts” corresponds to the line 16 of Table 8 and line “+jet isolation” corresponds to the line 17 of Table 8.

Table 9: Number of signal and background events remained after cuts.

$\hat{p}_\perp^{min}$ (GeV/c)	Cuts	$\gamma$ direct	$\gamma$ brem	photons from the mesons				$e^\pm$
				$\pi^0$	$\eta$	$\omega$	$K_S^0$	
40	Preselected	18056	14466	152927	56379	17292	14318	2890
	After cuts	6238	686	824	396	112	104	24
	+ jet isol.	3094	264	338	150	40	44	14
70	Preselected	39340	63982	761926	269666	87932	63499	17562
	After cuts	8608	424	320	146	58	36	64
	+ jet isol.	6266	262	206	90	40	24	52
100	Preselected	56764	111512	970710	346349	117816	91416	38872
	After cuts	11452	280	124	92	24	24	136
	+ jet isol.	9672	204	92	64	24	20	120

Table 10: Efficiency,  $S/B$  ratio and significance values in the selected events without jet isolation cut.

$\hat{p}_\perp^{min}$ (GeV/c)	$S$	$B$	$Eff_S(\%)$	$Eff_B(\%)$	$S/B$	$S/\sqrt{B}$
40	6238	2122	$34.55 \pm 0.51$	$0.831 \pm 0.018$	2.9	135.4
70	8608	984	$21.88 \pm 0.26$	$0.079 \pm 0.003$	8.8	274.4
100	11452	544	$20.17 \pm 0.21$	$0.033 \pm 0.001$	21.1	491.0

Table 11: Efficiency,  $S/B$  ratio and significance values in the selected events with jet isolation cut.

$\hat{p}_\perp^{min}$ (GeV/c)	$S$	$B$	$Eff_S(\%)$	$Eff_B(\%)$	$S/B$	$S/\sqrt{B}$
40	3094	836	$17.14 \pm 0.33$	$0.327 \pm 0.011$	3.7	107.0
70	6266	622	$15.93 \pm 0.22$	$0.050 \pm 0.002$	10.1	251.2
100	9672	404	$17.04 \pm 0.19$	$0.025 \pm 0.001$	23.9	481.2

Table 9 is done to show in more detail the origin of  $\gamma^{dir}$ -candidates. The numbers in the “ $\gamma$ -direct” column correspond to the respective numbers of signal events left in each of  $P_t^{\tilde{\gamma}}$  intervals



after application of the cuts defined in lines 1, 16 and 17 of Table 7 (and column “S” of Table 8). Analogously the numbers in the “ $\gamma - brem$ ” column of Table 9 correspond to the numbers of events with the photons radiated from quarks participating in the hard interactions. Columns 5–8 of Table 9 illustrate the numbers of the “ $\gamma - mes$ ” events with photons originating from  $\pi^0$ ,  $\eta$ ,  $\omega$  and  $K_S^0$  meson decays. In a case of  $P_t^{\tilde{\gamma}} > 70 \text{ GeV}/c$  the total numbers of background events, i.e. a sum over the numbers presented in columns 4–8 of Table 9, are shown in the lines 1, 16 and 17 of column “B” of Table 8. The other lines of Table 9 for  $\hat{p}_\perp^{min} = 40$  and  $100 \text{ GeV}/c$  have the meaning analogous to that described above for  $\hat{p}_\perp^{min} = 70 \text{ GeV}/c$ .

The last column of Table 9 shows the number of preselected events with  $e^\pm$ .

The numbers in Tables 10 (without jet isolation cut) and 11 (with jet isolation cut) accumulate in a compact form the final information of Tables 7 – 9. Thus, for example, the columns  $S$  and  $B$  of the line that corresponds to  $\hat{p}_\perp^{min} = 70 \text{ GeV}/c$  contain the total numbers of the selected signal and background events taken at the level of 16-th (for Table 10) and 17-th (for Table 11) cuts from Table 8.

It is seen from Table 10 that in the case of Selection 1 the ratio  $S/B$  grows from 2.9 to 21.1 while  $P_t^{\tilde{\gamma}}$  increases from  $P_t^{\tilde{\gamma}} \geq 40 \text{ GeV}/c$  to  $P_t^{\tilde{\gamma}} \geq 100 \text{ GeV}/c$  interval.

The jet isolation requirement (cut 17 from Table 7) noticeably improves the situation at low  $P_t^{\tilde{\gamma}}$  (see Table 11). After application of this criterion the value of  $S/B$  increases from 2.9 to 3.7 at  $P_t^{\tilde{\gamma}} \geq 40 \text{ GeV}/c$  and only from 21.1 to 23.9 at  $P_t^{\tilde{\gamma}} \geq 100 \text{ GeV}/c$ . Remember on this occasion the conclusion that the sample of events selected with our criteria has a tendency to contain more events with an isolated jet as  $P_t^{\tilde{\gamma}}$  increases <sup>48</sup>.

Let us underline here that, in contrast to other types of background, “ $\gamma - brem$ ” background has an irreducible nature. Thus, the number of “ $\gamma - brem$ ” events should be carefully estimated for each  $P_t^{\tilde{\gamma}}$  interval using the particle level of simulation in the framework of event generator like PYTHIA. They are also have to be taken into account in experimental analysis of the prompt photon production data at high energies.

Tables 12 and 13 shows the relative contributions of fundamental QCD subprocesses (having the largest cross sections)  $qg \rightarrow qg$ ,  $qq \rightarrow qq$ ,  $gg \rightarrow q\bar{q}$  and  $gg \rightarrow gg$  <sup>49</sup> that define the main production of “ $\gamma - brem$ ” and “ $\gamma - mes$ ” background in event samples selected with criteria 1–13 of Table 7 in three  $P_t^{\tilde{\gamma}}$  intervals.

Accepting the results of simulation with PYTHIA, we found from the event listing analysis that in the main part of selected “ $\gamma - brem$ ” events these photons are produced in the final state of the fundamental  $2 \rightarrow 2$  subprocess <sup>50</sup>. Namely, they are mostly radiated from the outgoing quarks in the case of the first three sets of subprocesses ( $qg \rightarrow qg$ ,  $qq \rightarrow qq$  and  $gg \rightarrow q\bar{q}$ ). They may also appear as a result of string breaking in a final state of  $gg \rightarrow gg$  scattering. But this subprocess, naturally, gives a small contribution into “ $\tilde{\gamma} + jet$ ” events production.

It may be noted also from the first two columns of Tables 12 and 13 that the most of “ $\gamma - brem$ ” and “ $\gamma - mes$ ” background events (93% at least) originate from  $qg \rightarrow qg$  and  $q_i q_j \rightarrow q_i q_j$ ,  $q_i \bar{q}_i \rightarrow q_j \bar{q}_j$  subprocesses. Tables 12 and 13 show also a tendency of increasing the contribution from the subprocess  $q_i q_j \rightarrow q_i q_j$  and  $q_i \bar{q}_i \rightarrow q_j \bar{q}_j$  (given in the second columns of tables) with growing  $P_t^{\tilde{\gamma}}$ .

The values of signal-to-background ratios in Tables 10, 11 are obtained without any detector effects. But these numbers can be noticeably increased if we take into account information

<sup>48</sup>see Sections 5–7 and Appendix 2

<sup>49</sup>ISUB=11, 12, 28, 53 and 68 (see [9])

<sup>50</sup>i.e. from lines 7, 8 in Fig. 3

Table 12: Relative contribution (in per cents) of different QCD subprocesses into the “ $\gamma$ -brem” events production.

$P_t^\gamma$ (GeV/c)	fundamental QCD subprocess			
	$qg \rightarrow qg$	$qq \rightarrow qq$	$gg \rightarrow q\bar{q}$	$gg \rightarrow gg$
40–70	62.1±6.6	31.8±4.0	3.3±1.0	2.8±0.9
70–100	52.3±7.7	42.4±6.4	3.8±1.4	1.5±0.9
> 100	41.8±6.0	56.9±7.2	1.3±0.7	—

Table 13: Relative contribution (in per cents) of different QCD subprocesses into the “ $\gamma$ -mes” events production.

$P_t^\gamma$ (GeV/c)	fundamental QCD subprocess			
	$qg \rightarrow qg$	$qq \rightarrow qq$	$gg \rightarrow q\bar{q}$	$gg \rightarrow gg$
40–70	59.3±5.2	34.8±3.5	2.9±0.7	2.4±0.7
70–100	48.6±8.0	47.3±7.8	0.5±0.5	0.5±0.5
> 100	41.8±6.4	53.9±7.6	1.8±0.9	0.7±0.5

from the preshower detector<sup>51</sup>. First of all, photons in the signal “ $\gamma + jet$ ” events have the distribution over number of preshower 3-dimensional<sup>52</sup> clusters  $N_{clust}^{PS}$  different from one for photon candidates in the QCD background events. Selection efficiencies for the signal and background events after application of the cut  $N_{clust}^{PS} \leq 1$  is shown in Fig. 14 for  $|\eta^{\tilde{\gamma}}| < 0.9$ . Relatively big numbers of  $N_{clust}^{PS}$  in the QCD background may be explained by the facts that besides  $\pi^0$ 's we have a contribution from events with multiphoton decays of  $\eta$ ,  $K_s^0$  and  $\omega$  mesons and that despite the strong isolation criteria photon candidates from the background events still have a hadron accompaniment.

Additional rejection can be obtained after analysis of energy distributions among the strips of each of three single layer clusters (SLC). They are again different for the signal and background events. As parameters for the discrimination one can take the energy weighted widths of three SLC's and ratios of energy deposited in the hottest strip to the total energy of SLC cluster  $E_{strip}^{max}/E_{SLC}$ . The selection efficiencies for single  $\gamma$ 's and  $\pi^0$ 's (as a most difficult case from the point of view of discrimination) are presented in Fig. 15<sup>53</sup>.

Thus, the total effect of data analysis in the preshower detector can lead to additional increase in the  $S/B$  of order of  $3 - 4$ <sup>54</sup>.

From Tables 9 – 11 we have seen that the cuts listed in Table 7 (having rather moderate values of  $P_{tCUT}^{clust}$  and  $P_{tCUT}^{out}$ ) allow to suppress the major part of the background events. The influence of these two cuts on:

- (a) the number of selected events (for  $L_{int} = 300 pb^{-1}$ );
- (b) the signal-to-background ratio  $S/B$ ;
- (c) the mean value of  $F \equiv (P_t^{\tilde{\gamma}} - P_t^{jet})/P_t^{\tilde{\gamma}}$  and its standard deviation value  $\sigma(F)$

is presented in Tables 1–12 of Appendix 3 for their variation in a wide range.

Let us emphasize that the tables of Appendix 3 include, in contrast to Appendix 2, the re-

<sup>51</sup>Central (CPS) and forward (FPS) preshower detectors are placed at  $|\eta| < 1.1$  and  $1.2 < |\eta| < 2.5$ , respectively, and have a similar 3-layered architecture with set of triangular scintillator strips in every layer.

<sup>52</sup>because they are built from 3 layers rotated in the space by some angles with respect to each other

<sup>53</sup>A consideration of the full QCD background left after our selection cuts (see cuts 1 – 16 of Table 7 plus requirement  $N_{clust}^{PS} \leq 1$  above) is very difficult because of a pure statistics. Obviously should decrease “ $\gamma$ -mes” background selection due to the “ $\eta$ ,  $K_s^0$ ,  $\omega$  events” contribution and probably due to an admixture of hadron accompaniment around  $\gamma$ -candidates in those events.

<sup>54</sup>these factors are caused mainly by the single photon selection efficiency and  $P_t^{\tilde{\gamma}}$  interval.

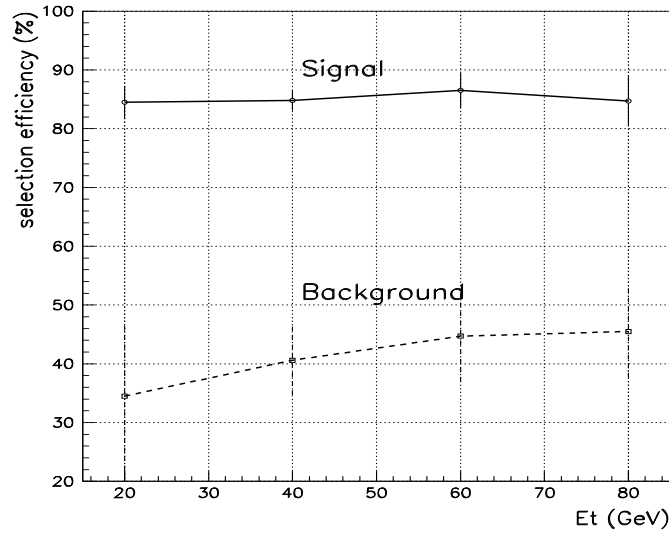


Fig. 14: Selection efficiencies for photons from “ $\gamma + jet$ ” process and photon candidates from QCD background obtained after cut on the number of 2-D clusters in the central preshower:  $N_{clust}^{PS} \leq 1$ .

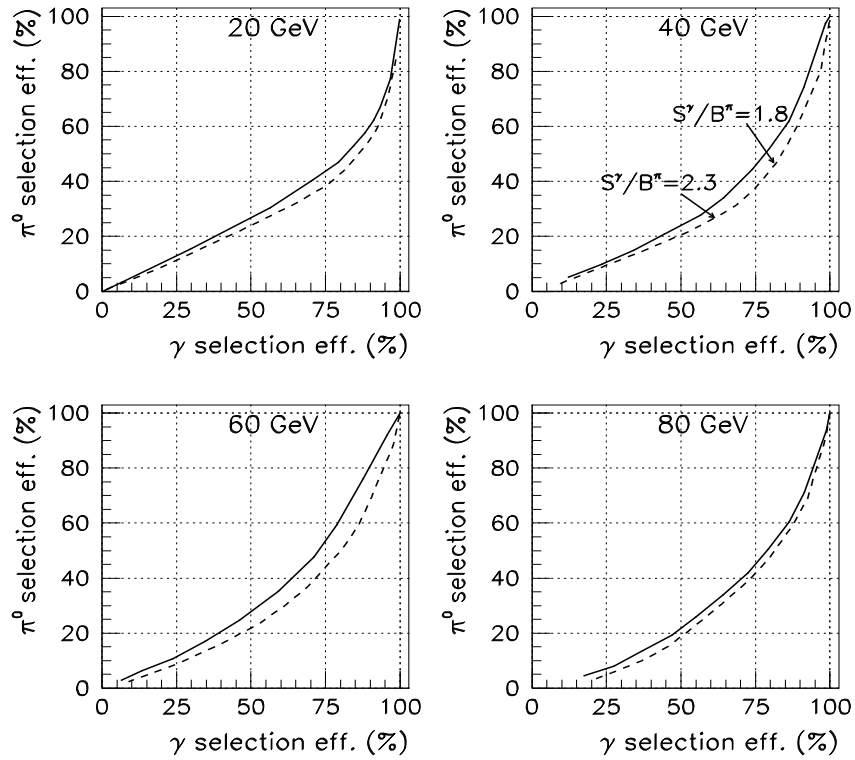


Fig. 15: Selection efficiency of single photon via selection efficiency of  $\pi^0$  obtained by using two set of quantities, measured in the preshower detector: three energy weighted widths of the single layer clusters (full line) and the same plus three ratios of energy deposited in the hottest strip to the total energy of SLC clusters  $E_{strip}^{max}/E_{SLC}$  (dashed line). Four  $P_t$  values, 20, 40, 60, 80, are considered on the plots above.

sults obtained after analyzing three generated samples (described in the beginning of this section) of *signal and background* events. These events were selected with the cuts of Table 7.

Namely, the cuts 1–10 of Table 7 were applied for preselection of “ $\tilde{\gamma} + 1 \text{ jet}$ ” events. The jets in these events as well as clusters were found by use of only one jetfinder LUCCELL (for the whole  $\eta$  region  $|\eta^{jet}| < 4.2$ ).

Tables 1–4 of Appendix 3 correspond to the simulation with  $\hat{p}_{\perp}^{min} = 40 \text{ GeV}/c$ . Analogously, the values of  $\hat{p}_{\perp}^{min} = 70 \text{ GeV}/c$  and  $\hat{p}_{\perp}^{min} = 100 \text{ GeV}/c$  were used for Tables 5–8 and Tables 9–12 respectively. The rows and columns of Tables 1–12 illustrate, respectively, the influence of  $P_{tCUT}^{clust}$  and  $P_{tCUT}^{out}$  on the quantities mentioned above in the points (a), (b), (c).

First of all, we see from Tables 2, 6 and 10 of Appendix 3 that a noticeable reduction of the background take place while moving along the table diagonal from the right-hand bottom corner to the left-hand upper one, i.e. with reinforcing  $P_{tCUT}^{clust}$  and  $P_{tCUT}^{out}$ . So, we see that for  $\hat{p}_{\perp}^{min} = 40 \text{ GeV}/c$  the value of  $S/B$  ratio changes in the table cells along the diagonal from  $S/B = 2.2$  (in the case of no limits on these two variables), to  $S/B = 2.9$  for the cell with  $P_{tCUT}^{clust} = 10 \text{ GeV}/c$  and  $P_{tCUT}^{out} = 10 \text{ GeV}/c$ . Analogously, for  $\hat{p}_{\perp}^{min} = 100 \text{ GeV}/c$  the value of  $S/B$  changes in the same table cells from 10.0 to 29.5 (see Table 10 of Appendix 3)<sup>55</sup>.

The second observation from Appendix 3. The restriction of  $P_{tCUT}^{clust}$  and  $P_{tCUT}^{out}$  improves the calibration accuracy. Table 3 shows that in the interval  $P_t^{\tilde{\gamma}} > 40 \text{ GeV}/c$  the mean value of the fraction  $F(\equiv (P_t^{\tilde{\gamma}} - P_t^{Jet})/P_t^{\tilde{\gamma}})$  decreases from 0.049 (the bottom right-hand corner) to 0.024 for the table cell with  $P_{tCUT}^{clust} = 10 \text{ GeV}/c$  and  $P_{tCUT}^{out} = 10 \text{ GeV}/c$ . At the same time, the both cuts lead to a noticeable decrease of the Gaussian width  $\sigma(F)$  (see Table 4 and also Tables 8, 12). For instance, for  $\hat{p}_{\perp}^{min} = 40 \text{ GeV}/c$   $\sigma(F)$  drops by about a factor of two: from 0.159 to 0.080. It should be also noted that Tables 4, 8 and 12 demonstrate that for any fixed value of  $P_{tCUT}^{clust}$  further improvement in  $\sigma(F)$  can be achieved by limiting  $P_t^{out}$  (e.g. in line with  $P_{tCUT}^{clust} = 10 \text{ GeV}/c$   $\sigma(F)$  drops by a factor of 2 with variation of  $P_t^{out}$  from 1000 to 5  $\text{GeV}/c$ ).

The explanation is simple. The balance equation (25) contains 2 terms on the right-hand side  $(1 - \cos\Delta\phi)$  and  $P_t(O+\eta > 4.2)/P_t^{\tilde{\gamma}}$ . The first one is negligibly small in a case of Selection 1 and tends to decrease with growing  $P_t^{\tilde{\gamma}}$  (see tables in Appendix 2). So, we see that in this case the main source of the disbalance in equation (25) is the term  $P_t(O+\eta > 4.2)/P_t^{\tilde{\gamma}}$ . This term can be diminished by decreasing  $P_t$  activity beyond the jet, i.e. by decreasing  $P_t^{out}$ .

The behavior of the number of selected events (for  $L_{int} = 300 \text{ pb}^{-1}$ ), the mean values of  $F = (P_t^{\tilde{\gamma}} - P_t^{Jet})/P_t^{\tilde{\gamma}}$  and its standard deviation  $\sigma(F)$  as a function of  $P_{tCUT}^{out}$  (with fixed  $P_{tCUT}^{clust} = 10 \text{ GeV}/c$ ) are also displayed in Fig. 16 for events with non-isolated (left-hand column) and isolated jets (right-hand column, see also Tables 13–24 of Appendix 3).

*Thus, we can conclude that application of two criteria introduced in Section 3.2, i.e.  $P_{tCUT}^{clust}$  and  $P_{tCUT}^{out}$ , results in two important consequences: significant background reduction and essential improvement of the calibration accuracy.*

The numbers of events (for  $L_{int} = 300 \text{ pb}^{-1}$ ) for different  $P_{tCUT}^{clust}$  and  $P_{tCUT}^{out}$  are given in the cells of Tables 1, 5 and 9 of Appendix 3. One can see that even with such strict  $P_{tCUT}^{clust}$  and  $P_{tCUT}^{out}$  values as, for example, 10  $\text{GeV}/c$  for both we would have a sufficient number of events (about 100 000, 7 000 and 1 300 for  $P_t^{\tilde{\gamma}} \geq 40 \text{ GeV}/c$ ,  $P_t^{\tilde{\gamma}} \geq 70 \text{ GeV}/c$  and  $P_t^{\tilde{\gamma}} \geq 100 \text{ GeV}/c$ , respectively) with low background contamination ( $S/B = 2.9, 8.8$  and  $21.1$ ) and a good accuracy of the  $P_t^{\tilde{\gamma}} - P_t^{Jet}$  balance:  $F = 2.4\%, 1.5\%$  and  $1.2\%$ , respectively, for the case of Selection 1.

In addition, we also present Tables 13–24 of Appendix 3. They contain the information

---

<sup>55</sup>even better results produces a combined application of stronger cuts  $P_{tCUT}^{clust} = 5 \text{ GeV}/c$  and  $P_{tCUT}^{out} = 5 \text{ GeV}/c$  (see Appendix 3)

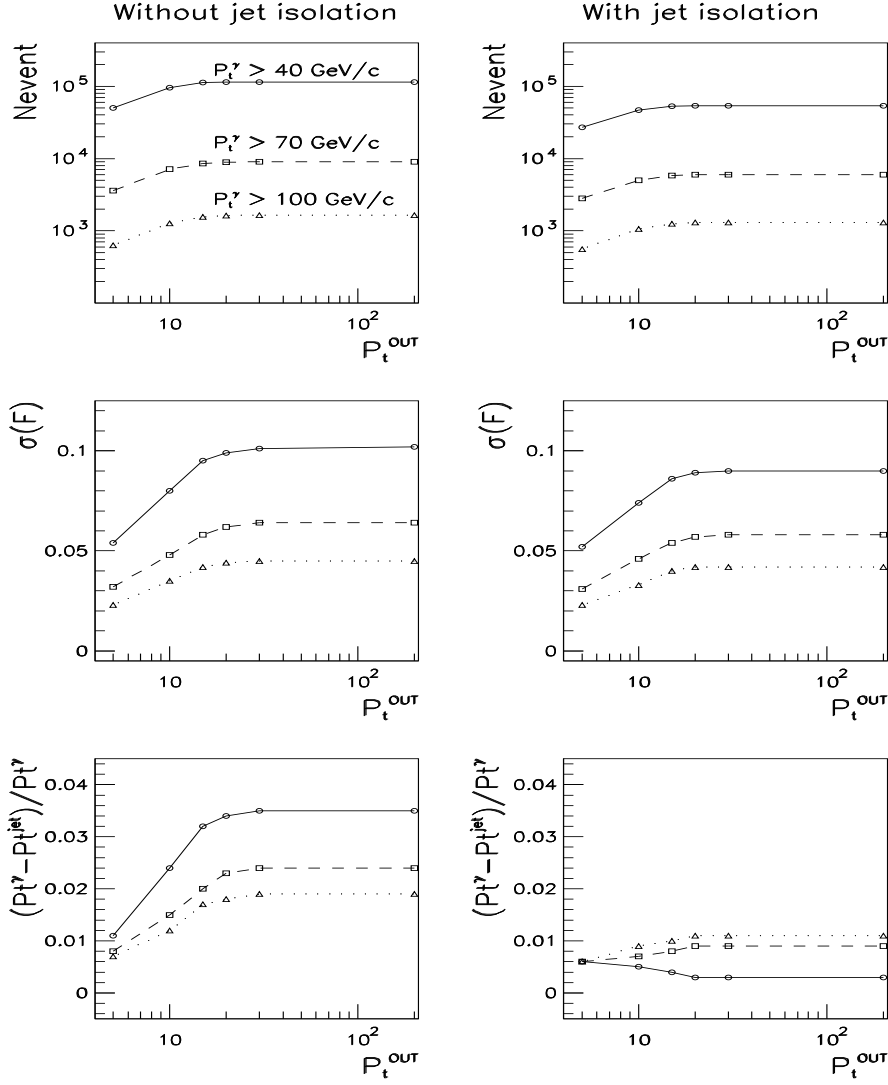


Fig. 16: Number of events (for  $L_{int} = 300 \text{ pb}^{-1}$ ), mean value of  $(P_t^{\tilde{\gamma}} - P_t^{Jet})/P_t^{\tilde{\gamma}} (\equiv F)$  and its standard deviation  $\sigma(F)$  distributions over  $P_t^{out}$  for the cases of non-isolated (left-hand column) and isolated (right-hand column) jet and for three intervals:  $P_t^{\tilde{\gamma}} > 40, 70$  and  $100 \text{ GeV}/c$ .  $P_{tCUT}^{clust} = 10 \text{ GeV}/c$ .

analogous to that in Tables 1 – 12 but for the case of isolated jets with  $\epsilon^{jet} < 3\%$ . From these tables we see that with the same cuts  $P_{tCUT}^{clust} = P_{tCUT}^{out} = 10 \text{ GeV}/c$  one can expect about 47 000, 5 000 and 1000 events for  $P_t^{\tilde{\gamma}} \geq 40 \text{ GeV}/c$ ,  $P_t^{\tilde{\gamma}} \geq 70 \text{ GeV}/c$  and  $P_t^{\tilde{\gamma}} \geq 100 \text{ GeV}/c$ , respectively, with a much more better fractional  $P_t^{\tilde{\gamma}} - P_t^{Jet}$  balance:  $F = 0.5\%, 0.7\%$  and  $0.1\%$ .

Let us mention that all these PYTHIA results give us an indication of a tendency and may serve as a guideline for further full GEANT simulation that would allow to come to a final conclusion.

To conclude this section we would like to stress, firstly, that, as is seen from Tables 9, the “ $\gamma - brem$ ” background defines a dominant part of the total background. One can see from Table 9 that  $\pi^0$  contribution being about the same as “ $\gamma - brem$ ” at  $\hat{p}_{\perp}^{min} > 40 \text{ GeV}/c$  becomes three times less than “ $\gamma - brem$ ” contribution at  $\hat{p}_{\perp}^{min} > 100 \text{ GeV}/c$ . We would like to emphasize here that this is a strong prediction of the PYTHIA generator that has to be compared with predictions of another generator like HERWIG, for example.

Secondly, we would like to mention also that, as it is seen from Tables 8 and 9, the photon isolation and selection cuts 1–6, usually used in the study of inclusive photon production (see, for instance, [33], [34], [35]), increase the  $S/B$  ratio up to 3.20 only (for  $P_t^{\tilde{\gamma}} \geq 70 \text{ GeV}/c$ ). The

other cuts 6–17, that select events with a clear “ $\gamma + jet$ ” topology and limited  $P_t$  activity beyond “ $\gamma + jet$ ” system, lead to quite a significant improvement of  $S/B$  ratio by a factor of three (to  $S/B = 10.07$ ).

The numbers in the tables of Appendix 3 were obtained with inclusion of the contribution from the background events. The tables show that their account does not spoil the  $P_t^\gamma - P_t^{jet}$  balance in the event samples preselected with the cuts 1–10 of Table 7. The estimation of the number of these background events would be important for the gluon distribution determination (see Section 9).

## 9. “ $\gamma + jet$ ” EVENT RATE ESTIMATION FOR GLUON DISTRIBUTION DETERMINATION AT THE TEVATRON RUN II.

*The number of “ $\gamma + jet$ ” events suitable for measurement of gluon distribution in different  $x$  and  $Q^2$  intervals at Run II is estimated. It is shown that with  $L_{int} = 3 fb^{-1}$  it would be possible to collect about one million of these events. This number would allow to cover a new kinematical area not studied in any previous experiment ( $10^{-3} < x < 1.0$  with  $1.6 \cdot 10^3 \leq Q^2 \leq 2 \cdot 10^4 (GeV/c)^2$ ). This area in the region of small  $x \geq 10^{-3}$  has  $Q^2$  by about one order of magnitude higher than reached at HERA now.*

As many of theoretical predictions for production of new particles (Higgs, SUSY) at the Tevatron are based on model estimations of the gluon density behavior at low  $x$  and high  $Q^2$ , the measurement of the proton gluon density for this kinematic region directly in Tevatron experiments would be obviously useful. One of the promising channels for this measurement, as was shown in [30], is a high  $P_t$  direct photon production  $p\bar{p}(p) \rightarrow \gamma^{dir} + X$ . The region of high  $P_t$ , reached by UA1 [31], UA2 [32], CDF [33] and D0 [34] extends up to  $P_t \approx 80 GeV/c$  and recently up to  $P_t = 105 GeV/c$  [35]. These data together with the later ones (see references in [37]–[45] and recent E706 [46] and UA6 [47] results) give an opportunity for tuning the form of gluon distribution (see [38], [42], [48]). The rates and estimated cross sections of inclusive direct photon production at the LHC were given in [30] (see also [49]).

Here for the same aim we shall consider the process  $p\bar{p} \rightarrow \gamma^{dir} + 1 Jet + X$  defined in the leading order by two QCD subprocesses (1a) and (1b) (for experimental results see [50], [51]).

Apart from the advantages, discussed in Section 8 in connection with the background suppression (see also [52]–[58]), the “ $\gamma^{dir} + 1 Jet$ ” final state may be easier for physical analysis than inclusive photon production process “ $\gamma^{dir} + X$ ” if we shall look at this problem from the viewpoint of extraction of information on the gluon distribution in a proton. Indeed, in the case of inclusive direct photon production the cross section is given as an integral over the products of a fundamental  $2 \rightarrow 2$  parton subprocess cross sections and the corresponding parton distribution functions  $f_a(x_a, Q^2)$  ( $a = \text{quark or gluon}$ ), while in the case of  $p\bar{p} \rightarrow \gamma^{dir} + 1 Jet + X$  for  $P_t^{Jet} \geq 30 GeV/c$  (i.e. in the region where “ $k_t$  smearing effects”<sup>56</sup> are not important, see [43]) the cross section is expressed directly in terms of these distributions (see, for example, [41]):

$$\frac{d\sigma}{d\eta_1 d\eta_2 dP_t^2} = \sum_{a,b} x_a f_a(x_a, Q^2) x_b f_b(x_b, Q^2) \frac{d\sigma}{dt}(ab \rightarrow cd), \quad (30)$$

where

$$x_{a,b} = P_t/\sqrt{s} \cdot (\exp(\pm\eta_1) + \exp(\pm\eta_2)). \quad (31)$$

The designation used above are as the following:  $\eta_1 = \eta^\gamma$ ,  $\eta_2 = \eta^{Jet}$ ;  $P_t = P_t^\gamma$ ;  $a, b = q, \bar{q}, g$ ;  $c, d = q, \bar{q}, g, \gamma$ . Formula (30) and the knowledge of  $q, \bar{q}$  distributions allow the gluon dis-

<sup>56</sup>This terminology is different from ours, used in Sections 2 and 9, as we denote by “ $k_t$ ” only the value of parton intrinsic transverse momentum.

tribution  $f_g(x, Q^2)$  to be determined after account of selection efficiencies for jets and  $\gamma^{dir}$  – candidates as well as after subtraction of the background contribution, left after the used selection cuts 1–13 of Table 7 (as it was discussed in Section 8 keeping in hand this physical application).

In the previous sections a lot of details connected with the structure and topology of these events and the features of objects appearing in them were discussed. Now with this information in mind we are in position to discuss an application of the “ $\gamma + jet$ ” event samples, selected with the previously proposed cuts, for estimating the rates of the gluon-based subprocess (1a) in different  $x$  and  $Q^2$  intervals.

Table 14 shows percentage of “Compton-like” subprocess (1a) (amounting to 100% together with (1b)) in the samples of events selected with cuts (16)–(22) of Section 3.2 for  $P_{tCUT}^{clust} = 10 \text{ GeV}/c$  for different  $P_t^\gamma$  and  $\eta^{jet}$  intervals: Central (CC) ( $|\eta^{jet}| < 0.7$ )<sup>57</sup>, Intercryostat (IC)  $0.7 < |\eta^{jet}| < 1.8$  and End (EC)  $1.8 < |\eta^{jet}| < 2.5$  parts of calorimeter. We see that the contribution of Compton-like subprocess grows by about 5 – 6% with  $|\eta^{jet}|$  enlarging and drops with growing  $P_t^{jet} (\approx P_t^\gamma$  in the sample of the events collected with the cuts 1 – 13 of Table 7).

Table 14: The percentage of Compton-like process  $qg \rightarrow \gamma + q$ .

Calorimeter part	$P_t^{jet}$ interval (GeV/c)			
	40–50	50–70	70–90	90–140
CC	84	80	74	68
IC	85	82	76	70
EC	89	85	82	73

In Table 15 we present distribution of the number of events that are caused by the  $qg \rightarrow \gamma + q$  subprocess, in various intervals of the  $Q^2 (\equiv (P_t^\gamma)^2)$ <sup>58</sup> and  $x$  (defined according to (31)). These events have passed the following cuts ( $P_t^{out}$  was not limited):

$$P_t^\gamma > 40 \text{ GeV}/c, \quad |\eta^\gamma| < 2.5, \quad P_t^{jet} > 30 \text{ GeV}/c, \quad |\eta^{jet}| < 4.2, \quad P_t^{hadr} > 7 \text{ GeV}/c, \\ P_{tCUT}^{isol} = 4 \text{ GeV}/c, \quad \epsilon_{CUT}^\gamma = 7\%, \quad \Delta\phi < 17^\circ, \quad P_{tCUT}^{clust} = 10 \text{ GeV}/c. \quad (32)$$

Table 15: Number of  $qg \rightarrow \gamma^{dir} + q$  events at different  $Q^2$  and  $x$  intervals for  $L_{int} = 3 \text{ fb}^{-1}$ .

$Q^2$ (GeV/c) <sup>2</sup>	$x$ values of a parton						All $x$
	.001 – .005	.005 – .01	.01 – .05	.05 – .1	.1 – .5	.5 – 1.	
1600-2500	8582	56288	245157	115870	203018	3647	632563
2500-4900	371	13514	119305	64412	119889	3196	320688
4900-8100	0	204	17865	13514	26364	1059	59007
8100-19600	0	0	3838	5623	11539	548	21549
							<b>1 033 807</b>

The analogous information for events with the charmed quarks in the initial state  $gc \rightarrow \gamma^{dir} + c$  is presented in Table 16. The simulation of the process  $gb \rightarrow \gamma^{dir} + b$  has shown that the rates for the  $b$ -quark are 8 – 10 times smaller than for the  $c$ -quark. These event rates are also given in Appendix 1 for different  $P_t^\gamma$  intervals in the lines denoted by “ $N_{events}(c/b)$ ”<sup>59</sup>.

<sup>57</sup>see also tables of Appendix 1 containing lines “29sub/all”

<sup>58</sup>see [9]

<sup>59</sup>Analogous estimation for LHC energy was done in [18] and [59].

Table 16: Number of  $gc \rightarrow \gamma^{dir} + c$  events at different  $Q^2$  and  $x$  intervals for  $L_{int} = 3 fb^{-1}$ .

$Q^2$ (GeV/c) <sup>2</sup>	$x$ values of a parton						All $x$ .001 – 1.
	.001 – .005	.005 – .01	.01 – .05	.05 – .1	.1 – .5	.5 – 1.	
1600-2500	264	2318	21236	11758	14172	58	49805
2500-4900	13	332	9522	6193	7785	40	23885
4900-8100	0	4	914	1055	1648	16	3637
8100-19600	0	0	142	329	612	8	1092
							<b>78 419</b>

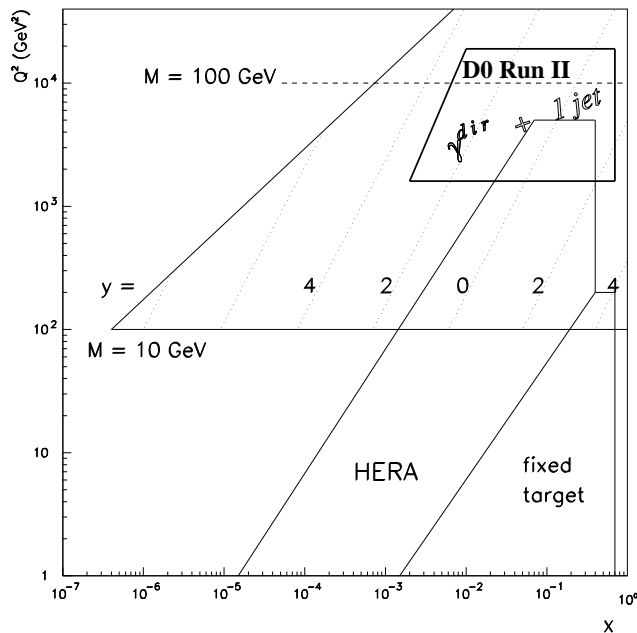


Fig. 17: The  $(x, Q^2)$  kinematic region for studying  $p\bar{p} \rightarrow \gamma + Jet$  process at Tevatron Run II.

Fig. 17 shows in the widely used  $(x, Q^2)$  kinematic plot (see [60] and also in [43]) what area can be covered by studying the process  $qg \rightarrow \gamma + q$  at Tevatron. The distribution of number of events in this area is given by Table 15. From this figure and Table 15 it becomes clear that with integrated luminosity  $L_{int} = 3 fb^{-1}$  it would be possible to study the gluon distribution with a good statistics of “ $\gamma + jet$ ” events in the region of  $10^{-3} < x < 1.0$  with  $Q^2$  by about one order of magnitude higher than reached at HERA now. It is worth emphasizing that extension of the experimentally reachable region at the Tevatron to the region of lower  $Q^2$  overlapping with the area covered by HERA would also be of great interest.

## 10. SUMMARY.

We have done an attempt here to consider, following [10]–[18], the physics of high  $P_t$  direct photon and jet associative production in proton-antiproton collisions basing on the predictions of PYTHIA generator and the models implemented there. This work may be useful for two practical goals: for absolute jet energy scale determination and for gluon distribution measurement at Tevatron energy.

The detailed information provided in the PYTHIA event listings allows to track the origin of different particles (like photons) and of objects (like clusters and jets) that appear in the final state. So, the aims of this work was to explore at the particle level as much as possible this information for finding out what effect may be produced by new variables, proposed in [10]–[17] for selection of “ $\gamma + jet$ ” events, and the cuts on them for solution of the mentioned above practical tasks.



For the first problem of the jet energy determination an important task is to select the events that may be caused (with a high probability) by the  $q\bar{q} \rightarrow g + \gamma$  and  $qg \rightarrow q + \gamma$  fundamental parton subprocesses of direct photon production. To take into account a possible effect of initial state radiation (its spectra are presented in different  $P_t^\gamma$  intervals in Section 5) we used here the  $P_t$ -balance equation (see (15)) written for an event as a whole. It allows to express  $P_t^\gamma - P_t^{jet}$  fractional disbalance (see (25)) through new variables [10]–[17] that describe the  $P_t$  activity *out* of “ $\gamma + jet$ ” system. They are  $P_t^{out}$  and  $P_t^{clust}$ , i.e.  $P_t$  of mini-jets or clusters that are additional to the main jet in event. The latter is the most “visible” part of  $P_t^{out}$ .

The sources of the  $P_t^\gamma - P_t^{jet}$  disbalance are investigated. It is shown that the limitation of  $P_t$  of clusters, i.e.  $P_t^{clust}$ , can help to decrease this disbalance. Analogously, the limitation of  $P_t$  activity of all detectable particles ( $|\eta_i| < 4.2$ ) beyond the “ $\gamma + jet$ ” system, i.e.  $P_t^{out}$ , also leads to a noticeable  $P_t^\gamma - P_t^{jet}$  disbalance reduction (see Sections 7,8).

It is demonstrated that in the events selected by means of simultaneous restriction from above of the  $P_t^{clust}$  and  $P_t^{out}$  activity the values of  $P_t^\gamma$  and  $P_t^{jet}$  are well balanced with each other. The samples of these “ $\gamma + jet$ ” events gained in this way are of a large enough volume for the jet energy scale determination in the interval  $40 < P_t^\gamma < 140 \text{ GeV}/c$  (see Tables 1–12 of Appendix 3).

It is worth mentioning that the most effect for improvement of  $P_t^\gamma$  and  $P_t^{jet}$  balance can be reached by applying additionally the jet isolation criterion defined in [10]–[17]. As it can be seen from Tables 13–18 of Appendix 2 and Tables 13–24 of Appendix 3, the application of this criterion allows to select the events having the  $P_t^\gamma - P_t^{jet}$  disbalance at the particle level less than 1%. Definitely, the detector effects may worsen the balance determination due to a limited accuracy of the experimental measurement<sup>60</sup>.

We present also PYTHIA predictions for the dependence of the distributions of the number of selected “ $\gamma + jet$ ” events on  $P_t^\gamma$  and  $\eta^{jet}$  (see Section 5 and also tables of Appendix 2 with account of  $P_t^{clust}$  variation).

The corrections to a jet  $P_t$  the measurable values of  $P_t^{jet}$  that have take into account the contribution from neutrinos belonging to a jet are presented for different  $P_t^{jet} (\approx P_t^\gamma$  for the selected events) intervals in the tables of Appendix 1. It is shown in Section 4 that a cut on  $P_t^{miss} < 10 \text{ GeV}/c$  allows to reduce the neutrino contribution to the value of  $\langle P_{t(\nu)}^{jet} \rangle_{all\ events} = 0.1 \text{ GeV}/c$ .

At the same time, as it is shown in [26], and discussed in Section 8 (see also [17]), this cut noticeably decreases the number of the background  $e^\pm$ -events in which  $e^\pm$  (produced in the  $W^\pm \rightarrow e^\pm \nu$  weak decay) may be registered as direct photon.

The possibility of the background events (caused by QCD subprocesses of  $qg, gg, qq$  scattering) suppression was studied in Section 8. Basing on the introduced selection criteria that include 17 cuts (see Table 7 of Section 8), the background suppression relative factors and the values of signal event selection efficiencies are estimated (see Tables 8-11).

It is shown that after applying the first 6 “photonic” cuts (that may be used, for example, for selecting events with inclusive photon production and lead to  $S/B$  ratio equal to 3.2 for  $P_t^\gamma > 70 \text{ GeV}/c$ , see Table 8) the use of the next 11 “hadronic” cuts of Table 7 may lead to further essential improvement of  $S/B$  ratio (by factor of 3.2 for the same  $P_t^\gamma > 70 \text{ GeV}/c$  where  $S/B$  becomes 10.1).

---

<sup>60</sup>We are planning to present the results of full GEANT simulation with the following digitization and reconstruction of signals by using the corresponding D0 packages in the forthcoming papers.

It is important to underline that this improvement is achieved by applying “hadronic” cuts that select the events having clear “ $\gamma + jet$ ” topology at the particle level and also having rather “clean” area (in a sense of limited  $P_t$  activity) beyond a “ $\gamma + jet$ ” system. In this sense and taking into account the fact that these “hadronic” cuts lead to an essential improvement of  $P_t^\gamma - P_t^{jet}$  balance, one may say that the cuts on  $P_t^{clust}$  and  $P_t^{out}$ , considered here, do act quite effectively to select the events caused by leading order diagrams (see Fig. 1) and do suppress the contribution of NLO diagrams, presented in Figs. 2, 4.

The consideration of the cuts, connected with detector effects (e.g., based the preshower usage) may lead to further noticeable improvement of  $S/B$  ratio.

Another interesting predictions of PYTHIA is about the dominant contribution of “ $\gamma$ -brem” events into the total background at Tevatron energy, as in was already mentioned in Section 8 (see also [17] and [26]). As the “ $\gamma$ -brem” background has irreducible nature its careful estimation is an important task and requires the analogous estimation with another generator.

To finish the discussion of the jet calibration study let us mention that the main results on this subject are summed up in Tables 1–12 (Selection 1) and 13–24 (Selection 2 with jet isolation criterion) of Appendix 3 and Fig. 16.

It should be emphasized that numbers presented in all mentioned tables and figures were found within the PYTHIA particle level of simulation. They may depend on the used generator and on the particular choice of a long set of its parameters<sup>61</sup> as well as they may change after account of the results of the full GEANT-based simulation.

It is also shown that the samples of the “ $\gamma + jet$ ” events, gained with the cuts used for the jet energy calibration, can provide an information suitable also for determining the gluon distribution inside a proton in the kinematic region (see Fig. 17) that includes  $x$  values as small as accessible at HERA [61], [62], but at much higher  $Q^2$  values (by about one order of magnitude):  $10^{-3} \leq x \leq 1.0$  with  $1.6 \cdot 10^3 \leq Q^2 \leq 2 \cdot 10^4 (GeV/c)^2$ . The number of events, based on the gluonic process (1a), that may be collected with  $L_{int} = 3 fb^{-1}$  in different  $x$ - and  $Q^2$ - intervals of this new kinematic region for this goal are presented in Table 15 (all quarks included) and in Table 16 (only for charm quarks).

## 11. ACKNOWLEDGMENTS.

We are greatly thankful to D. Denegri who initiated our interest to study the physics of “ $\gamma + jet$ ” processes, for his permanent support and fruitful suggestions. It is a pleasure for us to express our deep recognition for helpful discussions to P. Aurenche, M. Dittmar, M. Fontannaz, J.Ph. Guillet, M.L. Mangano, E. Pilon, H. Rohringer, S. Tapprogge, H. Weerts and J. Womersley. Our special gratitude is to J. Womersley also for supplying us with the preliminary version of paper [1], interest in the work and encouragements.

---

<sup>61</sup>We have already mentioned that we are planning to perform analogous analysis by help of another generator like HERWIG, for example. The comparison of predictions of different generators (PYTHIA, HERWIG, etc.) with the experimental results is a part of a work in any experiment.

## References

- [1] D0 Collaboration, F. Abachi *et al.*, NIM **A424** (1999)352 (Its earlier prototype: B. Abbot *et al.*, “Jet Energy Scale at D0”; D0 Note #3287 (1997) contains some more detailed discussions of different physical aspects of the calibration).
- [2] CDF Collaboration. F. Abe *et al.*, Phys.Rev. **D50** (1994)2966; F. Abe *et al.*, Phys.Rev.Lett. **73** (1994)225.
- [3] D. Denegri, R. Kinnunen, A. Nikitenko, CMS Note 1997/039 “Study of calorimeter calibration with  $\tau$ 's in CMS”.
- [4] R. Kinnunen, A. Nikitenko, CMS Note 1997/097 “Study of calorimeter calibration with pions from jets in CMS”.
- [5] J. Womersley. A talk at CMS Week meeting, Aachen, 1997.
- [6] J. Freeman, W. Wu, **draft** “In situ calibration of CMS HCAL calorimeter”.
- [7] R. Mehdiyev, I. Vichou, ATLAS Note ATL-COM-PHYS-99-054 (1999) “Hadronic jet energy scale calibration using Z+jet events”.
- [8] ATLAS Detector and Physics Performance, Technical Design Report, Volumes **1, 2**, 1999. CERN/LHCC 99-14.
- [9] T. Sjostrand, Comp.Phys.Comm. **82** (1994)74.
- [10] N.B. Skachkov, V.F. Konoplyanikov, D.V. Bandourin, “Photon – jet events for calibration of HCAL”. Second Annual RDMS CMS Collaboration Meeting. CMS-Document, 1996–213. CERN, December 16-17, 1996, p.7-23.
- [11] N.B. Skachkov, V.F. Konoplyanikov, D.V. Bandourin, “ $\gamma$ -direct + 1 jet events for HCAL calibration”. Third Annual RDMS CMS Collaboration Meeting. CMS-Document, 1997–168. CERN, December 16-17, 1997, p.139-153.
- [12] D.V. Bandourin, V.F. Konoplyanikov, N.B. Skachkov, ”Jet energy scale setting with ” $\gamma$ +jet” events for a hadronic calorimeter of CMS.” Fifth Annual RDMS CMS Collaboration Meeting. CMS Document 2000-058. Conference. ”Physics Program with the CMS Detector”, ITEP, Moscow, Russia. November 22-24, 2000. p. 422-427.
- [13] D.V. Bandourin, V.F. Konoplyanikov, N.B. Skachkov. “Jet energy scale setting with “ $\gamma + jet$ ” events at LHC energies. Generalities, selection rules.” JINR Preprint E2-2000-251, JINR, Dubna, hep-ex/0011012.
- [14] D.V. Bandourin, V.F. Konoplyanikov, N.B. Skachkov. “Jet energy scale setting with “ $\gamma + jet$ ” events at LHC energies. Event rates,  $P_t$  structure of jet.” JINR Preprint E2-2000-252, JINR, Dubna, hep-ex/0011013.
- [15] D.V. Bandourin, V.F. Konoplyanikov, N.B. Skachkov. “Jet energy scale setting with “ $\gamma + jet$ ” events at LHC energies. Minijets and cluster suppression and  $P_t^\gamma - P_t^{Jet}$  disbalance.” JINR Preprint E2-2000-253, JINR, Dubna, hep-ex/0011084.

- [16] D.V. Bandourin, V.F. Konoplyanikov, N.B. Skachkov. “Jet energy scale setting with “ $\gamma + jet$ ” events at LHC energies. Selection of events with a clean “ $\gamma + jet$ ” topology and  $P_t^\gamma - P_t^{Jet}$  disbalance.” JINR Preprint E2-2000-254, JINR, Dubna, hep-ex/0011014.
- [17] D.V. Bandourin, V.F. Konoplyanikov, N.B. Skachkov. “Jet energy scale setting with “ $\gamma + jet$ ” events at LHC energies. Detailed study of the background suppression.” JINR Preprint E2-2000-255, JINR, Dubna, hep-ex/0011017.
- [18] D.V. Bandourin, V.F. Konoplyanikov, N.B. Skachkov, ““ $\gamma + jet$ ” events rate estimation for gluon distribution determination at LHC”, Part.Nucl.Lett.103:34-43,2000, hep-ex/0011015.
- [19] D.V. Bandourin, N.B. Skachkov. “ $\gamma + jet$ ” process application for setting the absolute scale of jet energy and determining the gluon distribution at the Tevatron Run II.” D0 Note 3948, 2002, hep-ex/0203003.
- [20] M. Dittmar, K.Mazumdar, N. Skachkov, Proc. of “CERN Workshop on Standard Model Physics (and more) at the LHC”, QCD, Section 2.7 “Measuring parton luminosities and parton distribution functions at the LHC”, Yellow Report CERN-2000-004, May 2000, CERN, Geneva.
- [21] D.V. Bandourin, V.F. Konoplyanikov, N.B. Skachkov. “On the possibility of  $\pi^0, \eta, \omega, K_s^0$  mesons and a photon discrimination basing on the calorimeter information in the CMS detector”, JINR Communication E1-2001-261, JINR, Dubna, hep-ex/0108050.
- [22] D.V. Bandourin, N.B. Skachkov. “Separation of a single photon and products of the  $\pi^0, \eta, K_s^0$  mesons neutral decay channels in the CMS electromagnetic calorimeter using neural network”, JINR Communication E2-2001-259, JINR, Dubna, hep-ex/0108051.
- [23] GEANT3 - Detector Description and Simulation Tool, R. Brun *et al.*, GEANT3 CERN DD/EE/84-1, revised 1987.
- [24] S. Abdullin, A. Khanov, N. Stepanov, CMS Note CMS TN/94–180 “CMSJET”.
- [25] D.V. Bandourin, V.F. Konoplyanikov, N.B. Skachkov. “On the application of “ $\gamma + jet$ ” events for setting the absolute scale of the jet energy at the LHC and determining the gluon distribution”. CMS Note in preparation.
- [26] Talk at D0 QCD group meeting, see <http://www-d0.fnal.gov/Run2Physics/qcd/>, link to “Meeting June 21, 2001”.
- [27] Talk at D0 QCD group meeting, see <http://www-d0.fnal.gov/Run2Physics/qcd/>, link to “Meeting December 12, 2002”.
- [28] L. Lonnblad, C. Peterson, T. Rognvaldsson, “Mass reconstruction with a neural network” Phys.Lett.B278:181-186,1992.
- [29] I.A. Bertram *et al.*, “Single jet energy resolutions at D0 for Run I”, D0 Note 3414, 1998.
- [30] P. Aurenche *et al.* Proc. of “ECFA LHC Workshop”, Aachen, Germany, 4-9 Oktob. 1990, edited by G. Jarlskog and D. Rein (CERN-Report No 90-10; Geneva, Switzerland 1990), Vol. II.
- [31] UA1 Collaboration, C. Albajar *et al.*, Phys.Lett, **209B** (1998)385.

- [32] UA2 Collaboration, R. Ansari *et al.*, Phys.Lett. **176B** (1986)239.
- [33] CDF Collaboration. F. Abe *et al.*, Phys.Rev.Lett. **68** (1992)2734; F. Abe *et al.*,Phys.Rev. **D48** (1993)2998; F. Abe *et al.*,Phys.Rev.Lett., **73** (1994)2662.
- [34] D0 Collaboration, F. Abachi *et al.*, Phys.Rev.Lett, **77** (1996)5011.
- [35] D0 Collaboration, B. Abbott *et al.* , Phys.Rev.Lett. **84** 2786-2791,2000.
- [36] L3 Collaboration, D. Kirkby, CALT-69-1992, hep-ex/9505012.
- [37] T. Ferbel and W.R. Molzon, Rev.Mod.Phys. **56** (1984)181.
- [38] P. Aurenche, *et al.* Phys.Lett. **169B** (1986)441.
- [39] E.N. Argyres, A.P. Contogouris, N. Mebarki and S.D.P. Vlassopoulos, Phys.Rev, **D35** (1987)1534–1589.
- [40] P. Aurenche, *et al.* Phys.Rev. **D39** (1989)3275.
- [41] J.F. Owens, Rev.Mod.Phys. **59** (1987)465.
- [42] W. Vogelsang and A. Vogt, Nucl.Phys. **B453** (1995)334.
- [43] J. Huston ATLAS Note ATL-Phys-99-008, CERN,1999.
- [44] W. Vogelsang and M. Whally, J.Phys. **G23** (1997)A1.
- [45] S. Frixione and W. Vogelsang, CERN-TH/99-247, hep-ph/9908387.
- [46] E706 Collaboration, L. Apanasevich *et al.*, Phys.Rev.Lett., **81** (1997)2642.
- [47] UA6 Collaboration, G. Balocchi *et al.*, Phys.Lett.,**B436** (1998)222.
- [48] A.D. Martin *et al.*, Eur.Phys.J. **C4** (1998)463.
- [49] P. Aurenche, M. Fontannaz, S. Frixione Proc. of “CERN Workshop on Standard Model Physics (and more) at the LHC”, QCD, Section 6.1 “General features of photon production”, Yellow Report CERN-2000-004, 9 May 2000, CERN, Geneva.
- [50] ISR–AFS Collaboration, T.Akesson *et al.*, Zeit.Phys. **C34** (1987)293.
- [51] CDF Collaboration, F. Abe *et al.*, Phys.Rev. **D57** (1998)67.
- [52] E.L. Berger and J. Qiu, Phys.Rev. **D44** (1991)2002.
- [53] M. Fontannaz, S. Frixione, S. Tapprogge Proc. of “CERN Workshop on Standard Model Physics (and more) at the LHC”, QCD, Section 6 “Prompt photon production”, Yellow Report CERN-2000-004, 9 May 2000, CERN, Geneva.
- [54] G.P. Skoro, M.V. Tokarev, “Asymmetry of jet production in polarized  $pp$  collisions and sign of  $\Delta G$ ”, Proc. of the XIV International Seminar on High Energy Physics Problems “Relativistic Nuclear Physics and QCD”, Vol.II, p.120., hep-ph/0009028.

- [55] G.P. Skoro, M.V. Tokarev, "Asymmetry of jet production in polarized  $pp$  collisions at RHIC and sign of  $\Delta G$ ", Nuov. Cim. **A111** (1998) 353.
- [56] G.P. Skoro, M. Zupan, M.V. Tokarev, "Asymmetry of Prompt Photon Production in  $p - p$  Collisions at RHIC" Nuov. Cim. **A112** (1999) 809.
- [57] P. Chiapetta, G.J. Gounaris, J. Layssac and F.M. Renard "Glue constraining asymmetries in  $W, \gamma$  or  $Z$  production at CERN LHC", hep-ph/9807563.
- [58] J. Huston *et al.* "Study of the uncertainty of the gluon distribution", hep-ph/9801444.
- [59] M. Dittmar, F. Pauss, D. Zurcher, Phys.Rev.D56:7284-7290,1997; hep-ex/9705004.
- [60] R. Ball, M. Dittmar, W.J. Stirling, Proc. of "CERN Workshop on Standard Model Physics (and more) at the LHC", QCD, Section 2 "Parton distribution functions", Yellow Report CERN-2000-004, 9 May 2000, CERN, Geneva.
- [61] H1 Collaboration, S. Aid *et al.*, Nucl.Phys. **B470** (1996)3; C. Adloff *et al.* Nucl.Phys. **B497** (1997)3.
- [62] ZEUS Collaboration, M. Derrick *et al.*, Zeit.Phys. **C69** (1996)607; M. Derrick *et al.*, Zeit.Phys. **C72** (1996)399.
- [63] Particle Data Group, D.E. Groom *et al.*, The European Physical Journal C15 (2000) 1.

## Appendix 1

Selection 1.  $\phi_{(\gamma,jet)} = 180^\circ \pm 17^\circ$ . UA1 algorithm.  $L_{int} = 300 \text{ pb}^{-1}$ .

Table 1:  $40 < P_t^\gamma < 50 \text{ GeV}/c$ .

$P_{tCUT}^{clust}$	30	20	15	10	5
$P_t^{jet}$	42.646	42.460	42.410	42.564	42.912
$P_t^{Jet} - P_t^{jet}$	0.127	0.127	0.131	0.133	0.105
$P_{t(\nu)}^{Jet}$	0.129	0.128	0.133	0.135	0.106
$R_{event}^{\nu \in Jet}$	0.171	0.170	0.169	0.166	0.152
$P_{t(\mu)}^{Jet}$	0.153	0.153	0.158	0.157	0.113
$R_{event}^{\mu \in Jet}$	0.148	0.146	0.146	0.144	0.126
$P_t^{miss}$	2.088	2.083	2.096	2.105	2.101
$P_{t\nu \in Jet}^{miss}$	2.366	2.370	2.383	2.403	2.310
$Nevent_{(c)}$	964	926	865	723	348
$Nevent_{(b)}$	100	94	90	70	34
29sub/all	0.85	0.85	0.84	0.84	0.83
Entries	10493	10144	9472	7992	4421

Table 2:  $70 < P_t^\gamma < 90 \text{ GeV}/c$ .

$P_{tCUT}^{clust}$	30	20	15	10	5
$P_t^{jet}$	72.873	74.375	75.239	75.968	76.353
$P_t^{Jet} - P_t^{jet}$	0.257	0.259	0.272	0.250	0.245
$P_{t(\nu)}^{Jet}$	0.259	0.262	0.275	0.253	0.248
$R_{event}^{\nu \in Jet}$	0.182	0.176	0.177	0.175	0.173
$P_{t(\mu)}^{Jet}$	0.184	0.181	0.186	0.168	0.174
$R_{event}^{\mu \in Jet}$	0.172	0.169	0.171	0.172	0.165
$P_t^{miss}$	2.178	2.182	2.196	2.168	2.190
$P_{t\nu \in Jet}^{miss}$	3.092	3.123	3.179	3.118	3.089
$Nevent_{(c)}$	129	108	91	64	30
$Nevent_{(b)}$	22	18	13	9	2
29sub/all	0.77	0.76	0.76	0.75	0.72
Entries	13641	11613	9892	7495	3845

Table 3:  $90 < P_t^\gamma < 140 \text{ GeV}/c$ .

$P_{tCUT}^{clust}$	30	20	15	10	5
$P_t^{jet}$	101.878	103.159	103.988	104.565	104.615
$P_t^{Jet} - P_t^{jet}$	0.331	0.330	0.319	0.312	0.317
$P_{t(\nu)}^{Jet}$	0.334	0.333	0.321	0.315	0.320
$R_{event}^{\nu \in Jet}$	0.190	0.188	0.187	0.185	0.179
$P_{t(\mu)}^{Jet}$	0.272	0.283	0.272	0.280	0.309
$R_{event}^{\mu \in Jet}$	0.181	0.180	0.175	0.170	0.163
$P_t^{miss}$	2.186	2.197	2.193	2.195	2.201
$P_{t\nu \in Jet}^{miss}$	3.339	3.339	3.276	3.238	3.345
$Nevent_{(c)}$	51	40	32	22	9
$Nevent_{(b)}$	6	5	4	2	1
29sub/all	0.70	0.70	0.69	0.68	0.66
Entries	14058	11806	9997	7439	3673

## Appendix 2

$$P_t^{isol} < 4 \text{ GeV}/c, \quad \epsilon^\gamma < 7\%,$$

$$\phi_{(\gamma, jet)} = 180^\circ \pm 17^\circ. \quad \text{UA1 algorithm.} \quad L_{int} = 300 \text{ pb}^{-1}.$$

Table 4: Selection 1.  $40 < P_t^\gamma < 50 \text{ GeV}/c$ .

$P_{tCUT}^{clust}$	30	20	15	10	5
Nevent	12915	12486	11659	9837	5442
$P_t^{56}$	10.1	9.6	8.9	7.9	6.2
$\Delta\phi$	5.9	5.8	5.6	5.1	3.9
$P_t^{out}$	7.6	7.3	6.8	6.1	4.6
$P_t^{ \eta >4.2}$	2.0	2.0	2.0	2.0	2.0
$(P_t^\gamma - P_t^{part})/P_t^\gamma$	0.0120	0.0155	0.0147	0.0116	0.0071
$(P_t^J - P_t^{part})/P_t^J$	-0.0291	-0.0291	-0.0296	-0.0275	-0.0213
$(P_t^\gamma - P_t^J)/P_t^\gamma$	0.0363	0.0400	0.0400	0.0357	0.0266
$P_t(O+\eta>5)/P_t^\gamma$	0.0279	0.0319	0.0325	0.0293	0.0226
$1 - \cos(\Delta\phi)$	0.0084	0.0081	0.0076	0.0064	0.0040
$\sigma(Db[\gamma, J])$	0.1531	0.1414	0.1298	0.1142	0.0904
$\sigma(Db[\gamma, part])$	0.1957	0.1831	0.1667	0.1424	0.1105
Entries	10493	10144	9472	7992	4421

Table 5: Selection 1.  $70 < P_t^\gamma < 90 \text{ GeV}/c$ .

$P_{tCUT}^{clust}$	30	20	15	10	5
Nevent	2414	2055	1751	1327	681
$P_t^{56}$	14.7	12.5	11.0	9.1	6.8
$\Delta\phi$	5.4	4.7	4.2	3.4	2.3
$P_t^{out}$	12.5	10.4	8.9	7.0	4.9
$P_t^{ \eta >4.2}$	1.9	1.9	2.0	2.0	2.0
$(P_t^\gamma - P_t^{part})/P_t^\gamma$	0.0328	0.0184	0.0118	0.0067	0.0038
$(P_t^J - P_t^{part})/P_t^J$	-0.0411	-0.0310	-0.0244	-0.0192	-0.0151
$(P_t^\gamma - P_t^J)/P_t^\gamma$	0.0642	0.0440	0.0325	0.0233	0.0171
$P_t(O+\eta>5)/P_t^\gamma$	0.0570	0.0382	0.0279	0.0203	0.0156
$1 - \cos(\Delta\phi)$	0.0073	0.0058	0.0046	0.0030	0.0014
$\sigma(Db[\gamma, J])$	0.1518	0.1207	0.1015	0.0812	0.0624
$\sigma(Db[\gamma, part])$	0.1789	0.1467	0.1268	0.1048	0.0843
Entries	13641	11613	9892	7495	3845

Table 6: Selection 1.  $90 < P_t^\gamma < 140 \text{ GeV}/c$ .

$P_{tCUT}^{clust}$	30	20	15	10	5
Nevent	1242	1043	885	669	333
$P_t^{56}$	15.0	12.7	11.2	9.4	7.0
$\Delta\phi$	4.5	3.7	3.2	2.5	1.8
$P_t^{out}$	13.2	10.6	9.0	7.1	5.0
$P_t^{ \eta >4.2}$	1.9	1.9	1.9	1.9	1.9
$(P_t^\gamma - P_t^{part})/P_t^\gamma$	0.0102	0.0045	0.0014	0.0007	0.0003
$(P_t^J - P_t^{part})/P_t^J$	-0.0382	-0.0276	-0.0221	-0.0160	-0.0121
$(P_t^\gamma - P_t^J)/P_t^\gamma$	0.0417	0.0286	0.0213	0.0153	0.0112
$P_t(O+\eta>5)/P_t^\gamma$	0.0363	0.0248	0.0185	0.0136	0.0103
$1 - \cos(\Delta\phi)$	0.0054	0.0038	0.0028	0.0018	0.0009
$\sigma(Db[\gamma, J])$	0.1154	0.0896	0.0753	0.0605	0.0479
$\sigma(Db[\gamma, part])$	0.1359	0.1111	0.0981	0.0861	0.0677
Entries	26759	22471	19068	14411	7163

\*Number of events (Nevent) is given in this and in the following tables for integrated luminosity  $L_{int} = 300 \text{ pb}^{-1}$ .



Table 7: Selection 2.  $40 < P_t^\gamma < 50 \text{ GeV}/c$  ( $\epsilon^{jet} \leq 3\%$ ).

$P_t^{clust}$	30	20	15	10	5
Nevent	5189	5043	4804	4222	2689
$P_t^{56}$	9.4	8.9	8.4	7.4	5.9
$\Delta\phi$	5.5	5.4	5.3	4.8	3.8
$P_t^{out}$	7.0	6.7	6.3	5.6	4.3
$P_t^{ \eta >4.2}$	2.0	2.0	2.0	2.0	2.0
$(P_t^\gamma - P_t^{part})/P_t^\gamma$	-0.0237	-0.0179	-0.0143	-0.0126	-0.0085
$(P_t^J - P_t^{part})/P_t^J$	-0.0078	-0.0094	-0.0105	-0.0135	-0.0125
$(P_t^\gamma - P_t^J)/P_t^\gamma$	-0.0163	-0.0088	-0.0043	0.0001	0.0032
$P_t(O+\eta>5)/P_t^\gamma$	-0.0238	-0.0161	-0.0111	-0.0058	-0.0005
$1 - \cos(\Delta\phi)$	0.0076	0.0074	0.0069	0.0059	0.0038
$\sigma(Db[\gamma, J])$	0.1531	0.1373	0.1253	0.1082	0.0878
$\sigma(Db[\gamma, part])$	0.1814	0.1661	0.1515	0.1251	0.1028
Entries	4216	4097	3903	3430	2185

Table 8: Selection 2.  $70 < P_t^\gamma < 90 \text{ GeV}/c$  ( $\epsilon^{jet} \leq 3\%$ ).

$P_t^{clust}$	30	20	15	10	5
Nevent	1262	1152	1038	849	505
$P_t^{56}$	12.7	11.3	10.1	8.7	6.7
$\Delta\phi$	4.7	4.3	3.9	3.2	2.3
$P_t^{out}$	10.0	8.8	7.8	6.4	4.7
$P_t^{ \eta >4.2}$	2.0	2.0	2.0	2.0	2.0
$(P_t^\gamma - P_t^{part})/P_t^\gamma$	-0.0056	-0.0074	-0.0080	-0.0055	-0.0007
$(P_t^J - P_t^{part})/P_t^J$	-0.0126	-0.0135	-0.0137	-0.0120	-0.0124
$(P_t^\gamma - P_t^J)/P_t^\gamma$	0.0054	0.0042	0.0039	0.0049	0.0098
$P_t(O+\eta>5)/P_t^\gamma$	-0.0006	-0.0007	-0.0001	0.0022	0.0083
$1 - \cos(\Delta\phi)$	0.0060	0.0050	0.0040	0.0027	0.0014
$\sigma(Db[\gamma, J])$	0.1207	0.1012	0.0897	0.0743	0.0620
$\sigma(Db[\gamma, part])$	0.1442	0.1212	0.1083	0.0937	0.0806
Entries	7128	6507	5866	4794	2852

Table 9: Selection 2.  $90 < P_t^\gamma < 140 \text{ GeV}/c$  ( $\epsilon^{jet} \leq 3\%$ ).

$P_t^{clust}$	30	20	15	10	5
Nevent	797	711	632	511	288
$P_t^{56}$	13.4	11.6	10.4	8.9	6.9
$\Delta\phi$	4.0	3.4	2.9	2.4	1.8
$P_t^{out}$	10.9	9.2	8.0	6.6	4.8
$P_t^{ \eta >4.2}$	1.9	1.9	1.9	1.9	1.9
$(P_t^\gamma - P_t^{part})/P_t^\gamma$	-0.0100	-0.0101	-0.0092	-0.0062	-0.0018
$(P_t^J - P_t^{part})/P_t^J$	-0.0160	-0.0149	-0.0137	-0.0118	-0.0105
$(P_t^\gamma - P_t^J)/P_t^\gamma$	0.0045	0.0036	0.0034	0.0047	0.0077
$P_t(O+\eta>5)/P_t^\gamma$	0.0000	0.0004	0.0010	0.0031	0.0069
$1 - \cos(\Delta\phi)$	0.0045	0.0033	0.0024	0.0016	0.0008
$\sigma(Db[\gamma, J])$	0.0934	0.0764	0.0668	0.0552	0.0456
$\sigma(Db[\gamma, part])$	0.1145	0.0956	0.0872	0.0763	0.0624
Entries	17161	15309	13613	11009	6200

### Appendix 3

$$\hat{p}_\perp^{min} = 40 \text{ GeV}/c$$

$$P_t^{isol} < 2 \text{ GeV}/c, \quad \epsilon^{\tilde{\gamma}} < 5\%, \quad \Delta\phi = 17^\circ \quad (\text{Selection 1})$$

Table 1: Number of signal and background events (per  $L_{int} = 300 \text{ pb}^{-1}$ ).

$P_{t \text{ cut}}^{clust}$ (GeV/c)	$P_{t \text{ cut}}^{out}$ (GeV/c)					
	5	10	15	20	30	1000
5	40000	59000	62000	62000	62000	62000
10	50000	96000	112000	115000	115000	115000
15	52000	105000	132000	141000	143000	143000
20	53000	107000	139000	153000	158000	159000
30	53000	109000	143000	159000	170000	173000

Table 2:  $S/B$ .

$P_{t \text{ cut}}^{clust}$ (GeV/c)	$P_{t \text{ cut}}^{out}$ (GeV/c)					
	5	10	15	20	30	1000
5	$3.6 \pm 0.3$	$3.4 \pm 0.2$	$3.4 \pm 0.2$	$3.4 \pm 0.2$	$3.4 \pm 0.2$	$3.4 \pm 0.2$
10	$3.3 \pm 0.2$	$2.9 \pm 0.1$	$2.8 \pm 0.1$	$2.8 \pm 0.1$	$2.8 \pm 0.1$	$2.8 \pm 0.1$
15	$3.2 \pm 0.2$	$2.7 \pm 0.1$	$2.5 \pm 0.1$	$2.5 \pm 0.1$	$2.5 \pm 0.1$	$2.5 \pm 0.1$
20	$3.1 \pm 0.2$	$0.0 \pm 0.0$	$2.4 \pm 0.1$	$2.4 \pm 0.1$	$2.4 \pm 0.1$	$2.4 \pm 0.1$
30	$3.1 \pm 0.2$	$2.6 \pm 0.1$	$2.3 \pm 0.1$	$2.3 \pm 0.1$	$2.2 \pm 0.1$	$2.2 \pm 0.1$

Table 3:  $\langle F \rangle$ ,  $F = (P_t^{\tilde{\gamma}} - P_t^{Jet})/P_t^{\tilde{\gamma}}$ .

$P_{t \text{ cut}}^{clust}$ (GeV/c)	$P_{t \text{ cut}}^{out}$ (GeV/c)					
	5	10	15	20	30	1000
5	0.012	0.020	0.023	0.023	0.023	0.023
10	0.011	0.024	0.032	0.034	0.035	0.035
15	0.011	0.025	0.035	0.040	0.042	0.043
20	0.011	0.025	0.036	0.041	0.046	0.046
30	0.011	0.025	0.035	0.042	0.047	0.049

Table 4:  $\sigma(F)$ ,  $F = (P_t^{\tilde{\gamma}} - P_t^{Jet})/P_t^{\tilde{\gamma}}$ .

$P_{t \text{ cut}}^{clust}$ (GeV/c)	$P_{t \text{ cut}}^{out}$ (GeV/c)					
	5	10	15	20	30	1000
5	0.053	0.070	0.074	0.074	0.075	0.076
10	0.054	0.080	0.095	0.099	0.101	0.102
15	0.055	0.082	0.104	0.115	0.121	0.121
20	0.055	0.083	0.108	0.123	0.135	0.137
30	0.055	0.083	0.109	0.127	0.150	0.159

$$\hat{p}_{\perp}^{min} = 70 \text{ GeV}/c$$

$$P_t^{isol} < 2 \text{ GeV}/c, \quad \epsilon^{\tilde{\gamma}} < 5\%, \quad \Delta\phi = 17^{\circ} \quad (\text{Selection 1})$$

Table 5: Number of signal and background events (per  $L_{int} = 300 \text{ pb}^{-1}$ ).

$P_{t \text{ cut}}^{clust}$ (GeV/c)	$P_{t \text{ cut}}^{out}$ (GeV/c)					
	5	10	15	20	30	1000
5	2900	4500	4700	4700	4700	4700
10	3600	7100	8500	8900	9000	9000
15	3800	7700	10100	11200	11800	11800
20	3800	7900	10600	12300	13600	13700
30	3800	8000	10900	12900	15400	16000

Table 6:  $S/B$ .

$P_{t \text{ cut}}^{clust}$ (GeV/c)	$P_{t \text{ cut}}^{out}$ (GeV/c)					
	5	10	15	20	30	1000
5	11.1 ± 1.1	10.3 ± 0.8	10.3 ± 0.8	10.2 ± 0.8	10.1 ± 0.8	10.0 ± 0.8
10	10.1 ± 0.9	8.8 ± 0.5	8.3 ± 0.4	8.2 ± 0.4	8.1 ± 0.4	8.1 ± 0.4
15	9.8 ± 0.8	8.2 ± 0.5	7.4 ± 0.4	7.1 ± 0.3	6.8 ± 0.3	6.8 ± 0.3
20	9.4 ± 0.8	7.9 ± 0.4	7.0 ± 0.3	6.5 ± 0.3	6.1 ± 0.2	6.1 ± 0.2
30	9.3 ± 0.8	7.6 ± 0.4	6.6 ± 0.3	6.0 ± 0.2	5.4 ± 0.2	5.2 ± 0.2

Table 7:  $\langle F \rangle$ ,  $F = (P_t^{\tilde{\gamma}} - P_t^{Jet})/P_t^{\tilde{\gamma}}$ .

$P_{t \text{ cut}}^{clust}$ (GeV/c)	$P_{t \text{ cut}}^{out}$ (GeV/c)					
	5	10	15	20	30	1000
5	0.008	0.014	0.016	0.016	0.016	0.016
10	0.008	0.015	0.020	0.023	0.024	0.024
15	0.008	0.015	0.022	0.027	0.031	0.031
20	0.007	0.014	0.022	0.028	0.037	0.039
30	0.007	0.014	0.022	0.029	0.043	0.052

Table 8:  $\sigma(F)$ ,  $F = (P_t^{\tilde{\gamma}} - P_t^{Jet})/P_t^{\tilde{\gamma}}$ .

$P_{t \text{ cut}}^{clust}$ (GeV/c)	$P_{t \text{ cut}}^{out}$ (GeV/c)					
	5	10	15	20	30	1000
5	0.031	0.042	0.045	0.046	0.046	0.046
10	0.032	0.048	0.058	0.062	0.064	0.064
15	0.032	0.049	0.063	0.072	0.078	0.078
20	0.032	0.050	0.065	0.078	0.089	0.090
30	0.032	0.050	0.066	0.080	0.099	0.102

$$\hat{p}_\perp^{min} = 100 \text{ GeV}/c$$

$$P_t^{isol} < 2 \text{ GeV}/c, \quad \epsilon^{\tilde{\gamma}} < 5\%, \quad \Delta\phi = 17^\circ \quad (\text{Selection 1})$$

Table 9: Number of signal and background events (per  $L_{int} = 300 \text{ pb}^{-1}$ ).

$P_{t \text{ cut}}^{clust}$ (GeV/c)	$P_{t \text{ cut}}^{out}$ (GeV/c)					
	5	10	15	20	30	1000
5	510	820	870	870	870	870
10	630	1270	1560	1630	1650	1650
15	650	1380	1830	2050	2150	2150
20	660	1410	1930	2260	2520	2560
30	670	1430	1970	2370	2870	3060

Table 10:  $S/B$ .

$P_{t \text{ cut}}^{clust}$ (GeV/c)	$P_{t \text{ cut}}^{out}$ (GeV/c)					
	5	10	15	20	30	1000
5	29.5± 4.0	26.5± 2.7	25.3± 2.5	24.9± 2.4	24.9± 2.4	24.5± 2.3
10	26.9± 3.1	22.3± 1.7	20.1± 1.3	19.0± 1.2	18.7± 1.2	18.7± 1.2
15	24.5± 2.7	20.2± 1.4	17.1± 1.0	15.7± 0.8	14.9± 0.8	14.9± 0.8
20	23.6± 2.5	18.6± 1.2	15.5± 0.8	13.7± 0.7	12.3± 0.5	12.1± 0.5
30	23.1± 2.5	18.3± 1.2	14.7± 0.8	12.7± 0.6	10.8± 0.4	10.0± 0.4

Table 11:  $\langle F \rangle$ ,  $F = (P_t^{\tilde{\gamma}} - P_t^{Jet})/P_t^{\tilde{\gamma}}$ .

(GeV/c)						
	5	10	15	20	30	1000
5	0.007	0.012	0.013	0.013	0.013	0.013
10	0.007	0.012	0.017	0.018	0.019	0.019
15	0.007	0.012	0.017	0.021	0.024	0.024
20	0.007	0.012	0.017	0.022	0.027	0.029
30	0.007	0.012	0.017	0.022	0.030	0.038

Table 12:  $\sigma(F)$ ,  $F = (P_t^{\tilde{\gamma}} - P_t^{Jet})/P_t^{\tilde{\gamma}}$ .

$P_{t \text{ cut}}^{clust}$ (GeV/c)	$P_{t \text{ cut}}^{out}$ (GeV/c)					
	5	10	15	20	30	1000
5	0.022	0.031	0.034	0.034	0.034	0.034
10	0.023	0.035	0.042	0.044	0.045	0.045
15	0.023	0.035	0.045	0.052	0.055	0.055
20	0.023	0.036	0.046	0.055	0.061	0.061
30	0.023	0.036	0.047	0.057	0.066	0.067

$$\hat{p}_\perp^{min} = 40 \text{ GeV}/c$$

$$P_t^{isol} < 2 \text{ GeV}/c, \quad \epsilon^{\tilde{\gamma}} < 5\%, \quad \Delta\phi = 17^\circ, \quad \epsilon^{jet} < 3\% \quad (\text{Selection 2})$$

Table 13: Number of signal and background events (per  $L_{int} = 300 \text{ pb}^{-1}$ ).

$P_{t \text{ cut}}^{clust}$ (GeV/c)	$P_{t \text{ cut}}^{out}$ (GeV/c)					
	5	10	15	20	30	1000
5	23000	33000	34000	34000	34000	34000
10	27000	47000	53000	54000	54000	54000
15	28000	50000	60000	63000	63000	63000
20	28000	51000	62000	66000	68000	68000
30	28000	51000	63000	68000	72000	73000

Table 14:  $S/B$ .

$P_{t \text{ cut}}^{clust}$ (GeV/c)	$P_{t \text{ cut}}^{out}$ (GeV/c)					
	5	10	15	20	30	1000
5	$4.0 \pm 0.4$	$4.1 \pm 0.4$	$4.1 \pm 0.4$	$4.1 \pm 0.4$	$4.0 \pm 0.4$	$4.0 \pm 0.4$
10	$3.9 \pm 0.4$	$3.7 \pm 0.3$	$3.6 \pm 0.3$	$3.6 \pm 0.2$	$3.6 \pm 0.2$	$3.6 \pm 0.2$
15	$3.8 \pm 0.4$	$3.4 \pm 0.2$	$3.2 \pm 0.2$	$3.2 \pm 0.2$	$3.2 \pm 0.2$	$3.2 \pm 0.2$
20	$3.8 \pm 0.4$	$0.0 \pm 0.0$	$3.2 \pm 0.2$	$3.1 \pm 0.2$	$3.0 \pm 0.2$	$3.1 \pm 0.2$
30	$3.8 \pm 0.4$	$3.4 \pm 0.2$	$3.1 \pm 0.2$	$3.0 \pm 0.2$	$2.9 \pm 0.2$	$2.8 \pm 0.2$

Table 15:  $\langle F \rangle$ ,  $F = (P_t^{\tilde{\gamma}} - P_t^{Jet})/P_t^{\tilde{\gamma}}$ .

$P_{t \text{ cut}}^{clust}$ (GeV/c)	$P_{t \text{ cut}}^{out}$ (GeV/c)					
	5	10	15	20	30	1000
5	0.006	0.008	0.008	0.008	0.008	0.008
10	0.006	0.005	0.004	0.003	0.003	0.003
15	0.006	0.006	0.003	0.003	0.001	0.001
20	0.006	0.006	0.003	0.000	-0.002	-0.003
30	0.006	0.006	0.003	0.001	-0.005	-0.006

Table 16:  $\sigma(F)$ ,  $F = (P_t^{\tilde{\gamma}} - P_t^{Jet})/P_t^{\tilde{\gamma}}$ .

$P_{t \text{ cut}}^{clust}$ (GeV/c)	$P_{t \text{ cut}}^{out}$ (GeV/c)					
	5	10	15	20	30	1000
5	0.050	0.066	0.069	0.069	0.069	0.069
10	0.052	0.074	0.086	0.089	0.090	0.090
15	0.051	0.075	0.095	0.102	0.107	0.107
20	0.052	0.075	0.097	0.109	0.120	0.123
30	0.052	0.075	0.098	0.113	0.136	0.147

$$\hat{p}_{\perp}^{min} = 70 \text{ GeV}/c$$

$$P_t^{isol} < 2 \text{ GeV}/c, \quad \epsilon^{\tilde{\gamma}} < 5\%, \quad \Delta\phi = 17^{\circ}, \quad \epsilon^{jet} < 3\% \quad (\text{Selection 2})$$

Table 17: Number of signal and background events (per  $L_{int} = 300 \text{ pb}^{-1}$ ).

$P_{t\ cut}^{clust}$ (GeV/c)	$P_{t\ cut}^{out}$ (GeV/c)					
	5	10	15	20	30	1000
5	2300	3400	3600	3600	3600	3600
10	2800	5000	5800	6000	6000	6000
15	2900	5300	6700	7200	7400	7400
20	2900	5400	6900	7700	8200	8300
30	2900	5500	7000	8000	9000	9200

Table 18:  $S/B$ .

$P_{t\ cut}^{clust}$ (GeV/c)	$P_{t\ cut}^{out}$ (GeV/c)					
	5	10	15	20	30	1000
5	$11.8 \pm 1.3$	$11.6 \pm 1.1$	$11.4 \pm 1.0$	$11.3 \pm 1.0$	$11.3 \pm 1.0$	$11.1 \pm 1.0$
10	$11.0 \pm 1.1$	$10.1 \pm 0.8$	$9.5 \pm 0.6$	$9.3 \pm 0.6$	$9.3 \pm 0.6$	$9.3 \pm 0.6$
15	$10.9 \pm 1.1$	$9.6 \pm 0.7$	$9.0 \pm 0.6$	$8.6 \pm 0.5$	$8.4 \pm 0.5$	$8.4 \pm 0.5$
20	$10.6 \pm 1.1$	$9.3 \pm 0.6$	$8.5 \pm 0.5$	$8.1 \pm 0.5$	$7.5 \pm 0.4$	$7.4 \pm 0.4$
30	$10.5 \pm 1.0$	$9.1 \pm 0.6$	$8.2 \pm 0.5$	$7.6 \pm 0.4$	$6.8 \pm 0.3$	$6.6 \pm 0.3$

Table 19:  $\langle F \rangle$ ,  $F = (P_t^{\tilde{\gamma}} - P_t^{Jet})/P_t^{\tilde{\gamma}}$ .

$P_{t\ cut}^{clust}$ (GeV/c)	$P_{t\ cut}^{out}$ (GeV/c)					
	5	10	15	20	30	1000
5	0.006	0.009	0.009	0.009	0.009	0.009
10	0.006	0.007	0.008	0.009	0.009	0.009
15	0.005	0.007	0.009	0.009	0.009	0.009
20	0.005	0.006	0.008	0.009	0.010	0.010
30	0.005	0.006	0.008	0.009	0.010	0.010

Table 20:  $\sigma(F)$ ,  $F = (P_t^{\tilde{\gamma}} - P_t^{Jet})/P_t^{\tilde{\gamma}}$ .

$P_{t\ cut}^{clust}$ (GeV/c)	$P_{t\ cut}^{out}$ (GeV/c)					
	5	10	15	20	30	1000
5	0.031	0.040	0.043	0.043	0.043	0.043
10	0.031	0.046	0.054	0.057	0.058	0.058
15	0.031	0.047	0.059	0.066	0.069	0.069
20	0.031	0.047	0.060	0.071	0.078	0.078
30	0.032	0.047	0.061	0.073	0.086	0.088

$$\hat{p}_\perp^{min} = 100 \text{ GeV}/c$$

$$P_t^{isol} < 2 \text{ GeV}/c, \quad \epsilon^{\tilde{\gamma}} < 5\%, \quad \Delta\phi = 17^\circ, \quad \epsilon^{jet} < 3\% \quad (\text{Selection 2})$$

Table 21: Number of signal and background events (per  $L_{int} = 300 \text{ pb}^{-1}$ ).

$P_{t \text{ cut}}^{clust}$ (GeV/c)	$P_{t \text{ cut}}^{out}$ (GeV/c)					
	5	10	15	20	30	1000
5	460	720	760	760	760	760
10	560	1060	1250	1300	1300	1300
15	580	1130	1440	1570	1620	1620
20	580	1150	1490	1700	1830	1840
30	580	1160	1520	1750	2020	2090

Table 22:  $S/B$ .

$P_{t \text{ cut}}^{clust}$ (GeV/c)	$P_{t \text{ cut}}^{out}$ (GeV/c)					
	5	10	15	20	30	1000
5	$31.9 \pm 4.7$	$27.6 \pm 3.0$	$26.6 \pm 2.8$	$26.0 \pm 2.7$	$26.0 \pm 2.7$	$25.5 \pm 2.7$
10	$31.1 \pm 4.1$	$23.9 \pm 2.2$	$22.4 \pm 1.7$	$21.7 \pm 1.6$	$21.5 \pm 1.6$	$21.4 \pm 1.6$
15	$29.5 \pm 3.7$	$22.6 \pm 1.8$	$19.1 \pm 1.3$	$18.2 \pm 1.2$	$17.5 \pm 1.1$	$17.5 \pm 1.1$
20	$28.7 \pm 3.6$	$21.5 \pm 1.5$	$17.5 \pm 1.1$	$15.9 \pm 0.9$	$14.7 \pm 0.8$	$14.6 \pm 0.8$
30	$28.1 \pm 3.5$	$20.9 \pm 1.6$	$16.6 \pm 1.0$	$14.7 \pm 0.8$	$12.9 \pm 0.6$	$12.3 \pm 0.6$

Table 23:  $\langle F \rangle$ ,  $F = (P_t^{\tilde{\gamma}} - P_t^{Jet})/P_t^{\tilde{\gamma}}$ .

(GeV/c)						
	5	10	15	20	30	1000
5	0.006	0.009	0.010	0.010	0.010	0.010
10	0.006	0.009	0.010	0.011	0.011	0.011
15	0.006	0.008	0.010	0.011	0.011	0.011
20	0.006	0.008	0.010	0.010	0.011	0.011
30	0.006	0.008	0.009	0.010	0.011	0.011

Table 24:  $\sigma(F)$ ,  $F = (P_t^{\tilde{\gamma}} - P_t^{Jet})/P_t^{\tilde{\gamma}}$ .

$P_{t \text{ cut}}^{clust}$ (GeV/c)	$P_{t \text{ cut}}^{out}$ (GeV/c)					
	5	10	15	20	30	1000
5	0.022	0.030	0.032	0.032	0.033	0.033
10	0.023	0.033	0.040	0.042	0.042	0.042
15	0.023	0.034	0.043	0.048	0.050	0.050
20	0.023	0.035	0.044	0.051	0.056	0.056
30	0.023	0.035	0.044	0.053	0.060	0.060